APPLICATIONS OF DIFFERENTIAL ALGEBRAIC INCLUSIONS TO THE MODELING OF FRICTION AND CONTACT

熊, 小剛

https://doi.org/10.15017/1441188

出版情報：九州大学, 2013, 博士（工学）, 課程博士
バージョン：
権利関係：全文ファイル公表済

APPLICATIONS OF DIFFERENTIAL ALGEBRAIC INCLUSIONS TO THE MODELING OF FRICTION AND CONTACT

by

XIAOGANG XIONG

Acknowledgments

The writing of this dissertation would have never been possible without the financial support provided by the scholarships from the government of the P. R. of China and Kyushu University in Japan, and emotional support from many people during my Ph.D. research at Kyushu University.

I first would like to sincerely thank my chief supervisor, Professor Motoji Yamamoto, for providing me lots of help during my study in Kyushu University. He gave me the opportunity and courage to study in Japan. His kindness, encouragement, and patience have been great support throughout my research.

I would like to particularly thank my co-supervisor, Associate Professor Ryo Kikuuwe, for his enthusiastic and patient academic guidance. Any progression I made on my academic research cannot happen without his direction, education, and inspiration. I have benefited a lot from his excitation to science and engineering research.

I wish to express my thanks to Professor Takahiro Kondou, Professor Joichi Sugimura, Professor Svinin Mikhail, Associate Professor Kenji Tahara, Assistant Professor Takeshi Ikeda for their suggestions and comments throughout my Ph.D. research. I am also grateful to Mr. Kouki Shinya and Ms. Midori Tateyama for their help in various forms. Furthermore, I want to thank all previous and current Ph.D. and master students of Control Engineering Laboratory, Dr. Katsuki , Dr. Jin, Mr. Aung, Mr. Iwatani, and so on, for various interesting talks and discussions.

Finally, I am deeply thankful to my parents for their moral support and encouragement throughout my Ph.D. research.

Contents

List of figures

List of abbreviations

DI	Differential inclusion
DAI	Differential algebraic inclusion
HC	Hunt-Crossley
GMS	Generalized Maxwell-slip
COR	Coefficient of restitution
ODE	Ordinary differential equation
PID	Proportional integral derivative

Chapter 1

Introduction

1.1 Mechanical systems involving friction and contact

Friction and contact are common phenomena that occur in almost all mechanical systems. The two phenomena seems simple, but in fact they are much complicated, involving many factors, such as temperature and materials. Although it is impossible to give exact mathematical descriptions for friction and contact, they can be modeled by different simplified ways in different cases. According to the simplifications of friction and contact models, this dissertation classifies the description methods of mechanical systems into two groups, hard-constraint approaches and regularization approaches.

In some cases, the deformations caused by the friction and contact phenomena are negligible, comparing to the volume sizes of contact bodies. In those cases, the contact bodies can be idealized as rigid ones and can be assumed to be impenetrable to each other. From a mathematical point of view, friction and contact phenomena are described as tangential and normal constraints, respectively. This kind of descriptions for mechanical systems involving friction and contact are termed as hard-constraint approaches. They are preferred by academic researchers in the filed of multibody dynamical systems, because those hard-constraint approaches allow for great simplifications and lead to more robust numerical schemes for simulations of mechanical systems with friction and contact. Typical examples of mechanical systems described by hard-constraint approaches include woodpecker

toy [5, 6], slider-crank mechanism with a translational clearance joint [7, 8], and granular material with large quantity [9–11].

In some other cases, friction and contact are modeled by considering the microscopic deformations from the physical point of view, as opposed to the mathematical point of view. These models, usually consisting of spring and damper elements, are regularizations of the hard-constraint approaches. Those kind of description methods for mechanical systems are therefore termed as regularization approaches. They can be viewed as more realistic and closer to real systems than the hard-constraint approaches, because the variables and parameters in regularization approaches represent specific physical meanings, such as displacements, stiffness, and viscosity. Regularization approaches are appreciated by engineers in the field of virtual reality, especially, in cases where the contact bodies are not so rigid or even soft [12]. Regularized models of friction and contact are also applicable in mechanical engineering, such as friction compensations with regularized friction models [13, 14] and property estimations of soft object with regularized contact models [2–4, 15].

The friction and contact models in regularization approaches can be continuously extended to more sophistical models based on observations of experimental data. For example, the Hertz contact model is one of contact models in regularization approaches. It has been extended into Kelvin-Voigt model, Hunt-Crossly model [16], and other more complicated contact models [17].

1.2 Differential inclusion

Hard-constraint approaches describe mechanical systems involving friction and contact as differential inclusions (DIs), which are generalizations of ordinary differential equations (ODEs) as the following form:

$$\frac{\mathrm{d}}{\mathrm{d}t}x(t) \in F(x(t), u(t)) \tag{1.1}$$

where $x(t)$ is a vector that represents the states of systems, $u(t)$ is another vector representing the inputs, and $F(\cdot, \cdot)$ is a set-valued map rather than a single-valued one. The

map $F(x(t), u(t))$ is only set-valued at countable points of x and is single-valued at other values of x. The DI description (1.1) has the difficulty in numerical integration due to its set-valued characteristic. For example, DIs in [7, 18] have to be discretized by some Euler-like methods and then integrated numerically by special mathematical solvers, such as linear complementary problem (LCP) solvers and mixed linear complementary (MLCP) solvers.

In some cases, DIs cannot be explicitly written in the form (1.1). They can only be written in the form of differential algebraic inclusions (DAIs) as follows:

$$0 \in F(x(t), \dot{x}(t), u(t)). \tag{1.2}$$

In the main content of this dissertation, i.e., Chapter 3, 4, and 5, DIs in the form of (1.1) is regularized into DAIs (1.2) by considering the microscopic deformations caused by friction and contact. This way provides a new perspective for DI regularizations, which is different from the conventional regularization approaches.

1.3 Friction modeling

Hard-constraint approaches typically describe the friction force $f_T \in \mathbb{R}$ as a set-valued function of the velocity $v_T \in \mathbb{R}$ as follows [18, 19]:

$$f_T \in \begin{cases} -F & \text{if } v_T > 0 \\ [-F, F] & \text{if } v_T = 0 \\ F & \text{if } v_T < 0 \end{cases} \tag{1.3}$$

where F is the magnitude of kinetic friction force. The friction force at the static friction state is set-valued within the range $[-F, F]$, as shown by the vertical line segment in Fig 1.1(a). Such kind of discontinuous characteristic is important to describe the static friction [14]. It is easy to imagine that the set-valued friction model (1.3) leads to DI descriptions for mechanical systems involving friction.

In regularization approaches, the friction force f_T is typically described as a continuous

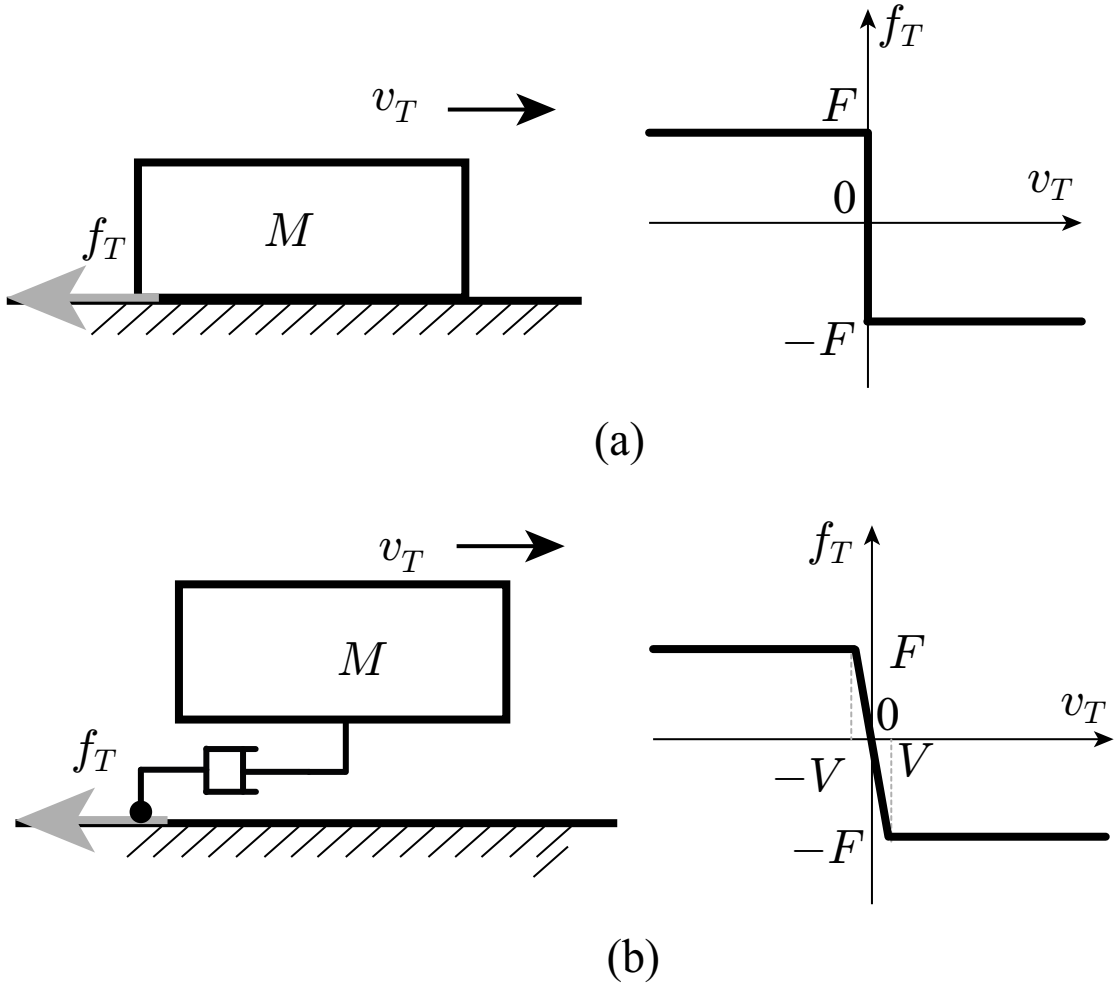

Figure 1.1: (a) One of typical ways to model friction in hard-constraints approaches, and (b) one of typical ways in regularization approaches

function of the velocity v_T as follows:

$$f_T = \begin{cases} -F & \text{if } v_T > V \\ -Fv_T/V & \text{if } |v_T| \leq V \\ F & \text{if } v_T < -V \end{cases} \tag{1.4}$$

where $V > 0$ is a threshold that is used to replace zero value for easinesses of numerical integration and $F/V > 0$ can be interpreted as the viscosity coefficient. This friction force law is illustrated in Fig 1.1(b). One can notice that the vertical portion in Fig 1.1(a) is replaced by a line segment with slope $-F/V$. This implies that the friction force is a continuous function of the velocity. It is easy to imagine that such kind of friction model lead to ODE descriptions for mechanical systems involving friction, without any integration problems. However, due to the lack of the discontinuous nature, such kind of friction models cause various strange behaviors. For example, the behavior of the friction model (1.4) heavily depends on the chosen value of the threshold V. Some more elaborately regularized models than (1.4), e.g., Dahl [20] and LuGre [21] friction models, produce positional drift in the static friction state.

Experimental data of friction in the literature, e.g., [22, 23], show that friction phenomena are more complicated than what is described by Fig 1.1(a) and Fig 1.1(b). From static friction to kinetic friction, friction is believed to experience two different regimes: the presliding regime and the sliding regime [24]. The presliding regime is the time period within which the major asperities in the contact surfaces are deformed elastically. The friction force is a function of presliding displacement, which is a consequence of the elastic deformations of asperities. In contrast, the sliding regime is the time period within which the major asperities are deformed inelastically and the interconnections of asperities between the contact surfaces are broken. The friction force is a function of the velocity, as roughly described by Coulomb friction model. It has been pointed out [24, 25] that, in reality, the transitions between the presliding and sliding regimes are not always sudden but gradual, and some features are observed in each regime, such as the presliding hysteresis with nonlocal mem-

ory[1] in the presliding regime and frictional lag[2] in the sliding regime. Smooth transitions between the two regimes and the features in each regime should be appropriately described by friction models for applications such as precise control of machines [27, 28] and precise simulations of mechanical systems [29, 30].

The Dahl model [20], the LuGre model [21, 31], and the single state elastoplastic model [32] are relatively simple models that are preferred for control applications. Each of them has one internal state variable representing the average deflection of asperities in the contact surfaces, and thus they can be referred to as single-state friction models. As a price for their simplicity, these three models do not capture some important properties of friction phenomena in the presliding regime. For instance, the Dahl and LuGre models produce unbounded positional drift even when the applied force is smaller than the maximum static friction force [32, 33]. The single state elastoplastic model is free from this problem, but none of those three models produce presliding hysteresis with nonlocal memory.

The modified Leuven model [23, 34], the generalized Maxwell-slip (GMS) model [35], and the smoothed GMS model [36, 37] can be referred to as multistate friction models because each of them includes more than one internal state variables. Those three multistate models are free from the aforementioned problems of the single-state friction models due to their sophisticated structures, but they still suffer from other problems. The modified Leuven model and the GMS models are described by equations involving discontinuities resulting from the switching between the presliding and sliding regimes. Such switching structures cause the difficulty in on-line parameters identification [36, 37]. The smoothed GMS model does not involve such discontinuities, but comparing to the original GMS model, this smoothed version additionally includes two functions and three parameters, which increases the difficulty in parameter identification. The formulations of the smoothed GMS model are any order smoothly differentiable. This characteristic is originally motivated from the easiness of parameter identifications, without any physical meanings.

[1]Hysteresis with nonlocal memory is defined as an input-output map, of which the output at any time instant depends on the output at some time instant in the past, the input since then, and the past extrema of the input or the output [22, 24]. This is in contrast to hysteresis with only local memory, of which the output only depends on the output at some time instant in the past [24].

[2]Frictional lag is time delay in the friction force as a function of velocity. It results in the friction force being larger during acceleration than that during deceleration [14, 21, 26].

There are some physically-motivated models that consider microscopic dynamics of contact surfaces. For example, generic models [38, 39] consider the effects of masses and geometries of asperities in the contact surfaces. As pointed out in [23, 40], the generic models give good agreements with experimental data, but they can be too complex for control applications due to the necessity of massive computation. The Burridge-Knopoff [41] and its modified versions, such as [42], also consider the masses of asperities and the stiffness of the couplings among the asperities. Those models can also be computationally expensive compared to the LuGre, Leuven, and GMS models, which are suited for control applications.

In Chapter 3, a single-state friction model derived from a DAI is used to approximate the hard-constraint model (1.3). Unlike the regularized model (1.4), the Dahl model, and the LuGre model, this single-state model is independent from any velocity thresholds and does not produce unbounded positional drift, but it produces only linearly elastic behavior in the presliding regime. Chapter 4 extends the DAI proposed in Chapter 3 to a multistate version with including Stribeck and frictional lag effects. This multistate version is composed of parallel connection of a number of elastoplastic elements, having a similar structure to those of the conventional multistate models and others [43–46]. The force produced by the extended model is analytically continuous with respect to the velocity and the state variables because it is transformable to a set of ODEs with continuous right-hand sides. Moreover, it captures the Stribeck effect, nondrifting property, stick-slip oscillation, presliding hysteresis with nonlocal memory, and frictional lag, which are major features of friction phenomena reported in the literature.

1.4 Contact modeling

Hard-constraint approaches typically describe the contact force $f_N \in \mathbb{R}$ as a set-valued function of the positional distance $p_N \in \mathbb{R}$ as follows:

$$f_N \in \begin{cases} 0 & \text{if } p_N > 0 \\ [0, \infty] & \text{if } p_N = 0 \\ \emptyset & \text{if } p_N < 0. \end{cases} \tag{1.5}$$

The contact force is set-valued within the scope $[0, +\infty]$ when the contact is closed, i.e., $p_N = 0$, as shown by the vertical portion in Fig. 1.2(a). When the contact is open, i.e., $p_N > 0$, the contact force is $f_N = 0$. The empty set at $p_N < 0$ implies that the contact bodies are idealized as rigid and impenetrable. The nonnegative force $f_N \geq 0$ in (1.5) implies that the contact bodies are not sticky to each other. One can notice the orthogonal corner at the origin in Fig 1.2(a), which shows the discontinuities of contact model (1.5). It is easy to imagine that such a set-valued model leads to DI descriptions for mechanical systems involving contact.

In regularization approaches, the relation between f_N and p_N is typically described as a continuous function $f_N = \max(0, -kp_N)$ where k can be interpreted as the stiffness. One can notice that the vertical portion in Fig 1.1(a) has been replaced by an inclined one with slope $-k$ in Fig 1.2(b). The contact force is zero when the contact is open, i.e., $p_N > 0$. The contact force is proportional to the penetration $-p_N$ when the contact is closed, $p_N \leq 0$. The Hertz contact model can be viewed as a nonlinear extension of this regularized model.

The contact between two bodies is in fact more complicated than that described by the hard-constraint and regularization approaches in Fig 1.2(a) and (b). The force exerted by a contact varies according to nonlinear relations with time and the relative displacement, both during the contact and at the beginning and end of the contact. In order to precisely simulate the behaviors of various mechanical systems, such relations must be appropriately modeled. Much effort has been paid for the modeling of contact, especially those among biological tissues [2, 3], components of machinery [47, 48], rubber materials [4, 15, 49, 50] and granular materials [51, 52].

The Kelvin-Voigt (KV) model is one of simply regularized models. It is based on a linear spring-dashpot model and it captures energy dissipation during contact [53]. The drawback of this model is that it produces a discontinuous jump in the force at the beginning of contact and a sticky force (negative contact force) in the end of contact [16, 53, 54]. Hunt-Crossley (HC) model [16] is another compliant contact model that is free from such weaknesses. HC model is a combination of Hertz-like nonlinear compliance and an indentation-dependent damping term. This model is extended in [12, 54–57] and empirically validated in [2, 3, 50, 58–60]. As pointed out in [55], however, HC model can produce unnatural sticky force

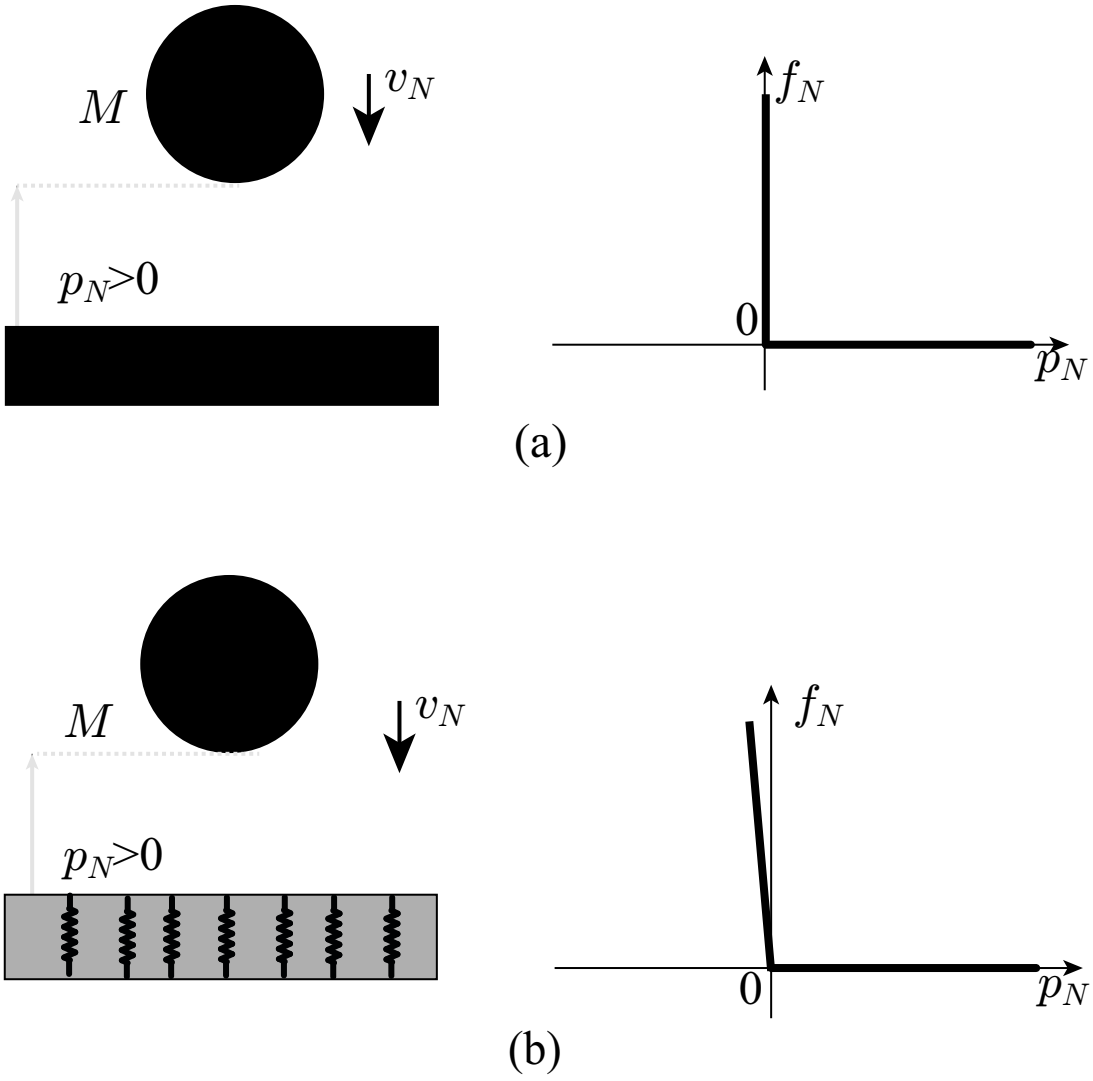

Figure 1.2: (a) One of typical ways to model contact in hard-constraints approaches, and (b) one of typical ways in regularization approaches

especially when the contact objects are separated rapidly by an external force. Moreover, the experiments in [60] show that the HC model is only consistent with empirical results when the coefficient of restitution (COR) is large [61].

The literature includes some report regarding the force-indentation curves obtained from real objects [2–4, 15, 49, 60]. Those force-indentation curves agree with the curves of HC model in most aspects, but differ in that, when the force arrives back in zero, the indentation is still not zero. That is, one can say that a contact force model should satisfy the following three conditions:

(i) the contact force should be continuous with respect to time at the time of contact;

(ii) the force-indentation curve can be designed to be nonlinear as is in Hertz's contact model;

(iii) the indentation can be nonzero at the time of loss of contact force.

As discussed earlier, KV and HC models fail to satisfy two and one, respectively, of the three conditions. There have been some models [49, 61–64] that satisfy those conditions. These models, however, describes the restitution phase and the compression phase separately, in different equations from each other. As far as the author are aware, there have been no contact model that realizes the aforementioned features in a unified framework. In this dissertation, lacking of discontinuity nature is thought to be the reason for their problems of those models.

In Chapter 3, a linear contact model derived from a DAI is used to approximate the hard-constraint model (1.5). This model does satisfy the conditions (i) and (iii) but does not satisfy the condition (ii), producing a linear force-indentation curve. Chapter 5 extends the DAI proposed in Chapter 3 to a new nonlinear DAI by adding a Hertz-like power-law nonlinearity and displacement-dependent viscosity such that the equivalent ODE formulation, i.e., the new contact model, satisfies the aforementioned three conditions.

1.5 Major achievements

This dissertation focuses on modeling friction and contact for simulation and engineering applications. First, this dissertation regularizes DIs by using DAIs for simulations of mechanical systems involving friction and contact. In contrast to previous regularization approaches, the new approach preserve the discontinuity of original DIs. It is free from various problems of unnatural behaviors produced by the conventional regularization approaches. Then, this dissertation extends the DAIs of friction and contact to more sophisticated formulations for engineering applications. Extensive simulation studies show that the properties of the new models derived from the extended DAIs are consistent with the experimental data reported in the literature. The major achievement are as follows:

- **New simulation method for mechanical systems (Chapter 3)**

  This method provides a new perspective to regularize DIs for simulations of mechanical systems. Different from straightforward approximations of DIs by ODEs in conventional regularization approaches, this new model first relaxes the rigid-bodies based DIs into DAIs with considering the deformations of bodies. Then, those DAIs are equivalently transformed into ODEs. Therefore, it has the features of both hard-constraint and regularization approaches and possesses both of their advantages. The new approximation method makes it feasible to simulate complicated mechanical systems with an easy integration procedure as regularization approaches. On the other hand, it preserves the discontinuous nature of the original systems.

- **New friction model (Chapter 4)**

  This new friction model is an extended version of the friction model proposed in Chapter 3. This extended model is free of the positional drift problem of Dahl and LuGre model, unnatural nondrifting behavior of Leuven model, and discontinuous force of the GMS model. The problems of first three models are caused by lacking of the discontinuous nature of friction between presliding and sliding regimes. The GMS model does not suffer from the problems of the previous three models due to its preservation of discontinuous nature, but it encounters the mathematical difficulty in dealing with transitions between the presliding and sliding regimes. A pair of switch-

ing conditions have to be used in the GMS model for the transitions. On the contrary, the extended friction model not only preserves the discontinuous nature of friction, but also allows smooth transitions between the presliding and sliding regimes without any switching structures. In addition, the extended friction model captures all the properties of friction that the GMS model does.

- **New contact model (Chapter 5)**

  This new model is a nonlinear extension of the contact model proposed in Chapter 3. It can simultaneously satisfy those three features of contact phenomena observed from experimental data without suffering from the problems of the KV and HC models. Different from the KV and HC models, this new model has two viscosity terms for energy dissipation, which leads to adjustable coefficient of restitutions (CORs) even at low impact velocities. Those two terms have similar physical meanings with respect to those in the KV and HC models. Furthermore, it can produce similar behaviors to the KV and HC models by adjusting the two viscosity terms. Therefore, both the KV model and HC model can be viewed as special cases of this extended contact model in a unified form.

1.6 Organization

The rest of this dissertation is organized as follows. Chapter 2 provides mathematical preliminaries that will be used throughout this dissertation. Chapter 3 proposes to regularize DIs into DAIs for simulations of mechanical systems involving friction and contact. It illustrates the simplicity and efficiency of this new approach through three examples. Chapter 4 extends the single-state friction model in Chapter 3 to a multistate version and illustrates the consistences between the extended model and experimental data reported in the literature. Chapter 5 extends the linear contact model in Chapter 3 to a new nonlinear version and illustrates its properties through numerical simulations. Chapter 6 provides concluding remarks.

Chapter 2

Mathematical preliminaries

For the discussion throughout this dissertation, this section introduces three functions: sgn, sat and dio. Some theorems regarding those functions are also presented. In the rest of this dissertation, $\mathbb{R}$ denotes the set of all real numbers and $\mathbb{R}_+$ denotes the set of all nonnegative real numbers. The symbol 0 denotes the zero vector of an appropriate dimension.

2.1 Signum function

First, let us define the signum function $\mathrm{sgn} : \mathbb{R}^n \to \mathbb{R}^n$ and the unit saturation function $\mathrm{sat} : \mathbb{R}_+ \times \mathbb{R}^n \to \mathbb{R}^n$ as follows:

$$\mathrm{sgn}(x) \triangleq \begin{cases} x/\|x\| & \text{if } \|x\| \neq 0 \\ \{z \in \mathbb{R}^n \mid \|z\| \leq 1\} & \text{if } \|x\| = 0 \end{cases} \tag{2.1}$$

$$\mathrm{sat}(Z, x) \triangleq \begin{cases} Zx/\|x\| & \text{if } \|x\| > Z \\ x & \text{if } \|x\| \leq Z \end{cases} \tag{2.2}$$

where $x \in \mathbb{R}^n$, $Z \in \mathbb{R}_+$ and $\|\cdot\|$ denotes the vector two-norm. If $n = 1$, the $\mathrm{sgn}(x)$ and $\mathrm{sat}(Z, x)$ can be depicted as Fig. 2.1(a) and Fig. 2.1(b), respectively. The following theorem is useful to rewrite the DIs involving sgn as ODEs involving sat:

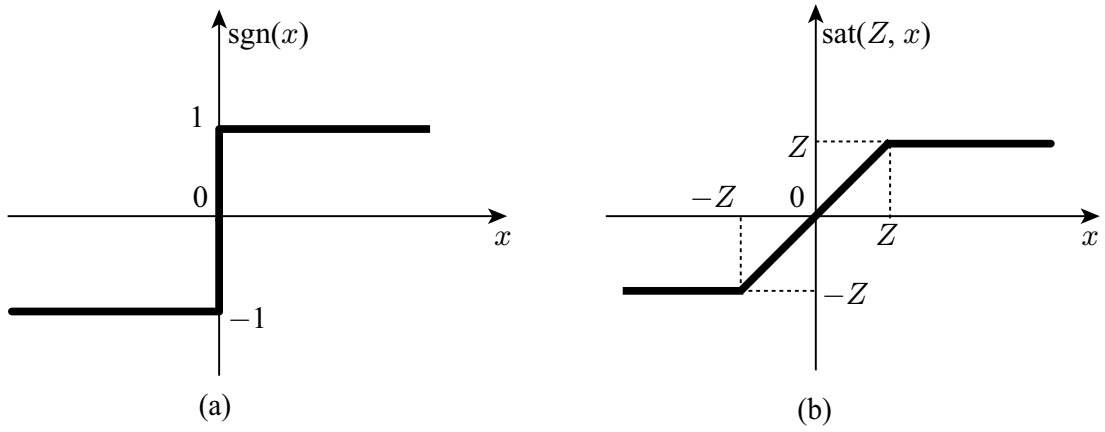

Figure 2.1: The signum function $\mathrm{sgn}(x)$ and saturation function $\mathrm{sat}(Z, x)$

Theorem 1. *For $x, y \in \mathbb{R}^n$ and $Z \in \mathbb{R}_+$, the following relation holds true [65, 66]:*

$$y \in Z\mathrm{sgn}(x - y) \Leftrightarrow y = \mathrm{sat}(Z, x). \tag{2.3}$$

Proof. : A proof can be given as follows:

$$\begin{aligned}
&y \in Z\mathrm{sgn}(x - y) \Leftrightarrow (y = Z(x - y)/\|x - y\| \wedge x \neq y) \vee (y = x \wedge \|y\| \leq Z) \\
&\Leftrightarrow (y = Zx/(Z + \|x - y\|) \wedge x \neq y \wedge \|y\| = Z) \vee (y = x \wedge \|x\| \leq Z) \\
&\Leftrightarrow (y = Zx/(Z + \|x - y\|) \wedge \|x\| = Z + \|x - y\| > Z) \vee (y = x \wedge \|x\| \leq Z) \\
&\Leftrightarrow (y = Zx/\|x\| \wedge \|x\| > Z) \vee (y = x \wedge \|x\| \leq Z) \Leftrightarrow y = \mathrm{sat}(Z, x).
\end{aligned}$$

□

2.2 Diode function

Next, let us define the "diode" function $\mathrm{dio} : \mathbb{R}_+ \to \mathbb{R}_+$ as follows:

$$\mathrm{dio}(x) \triangleq \begin{cases} 0 & \text{if } x > 0 \\ \mathbb{R}_+ & \text{if } x = 0 \end{cases} \tag{2.4}$$

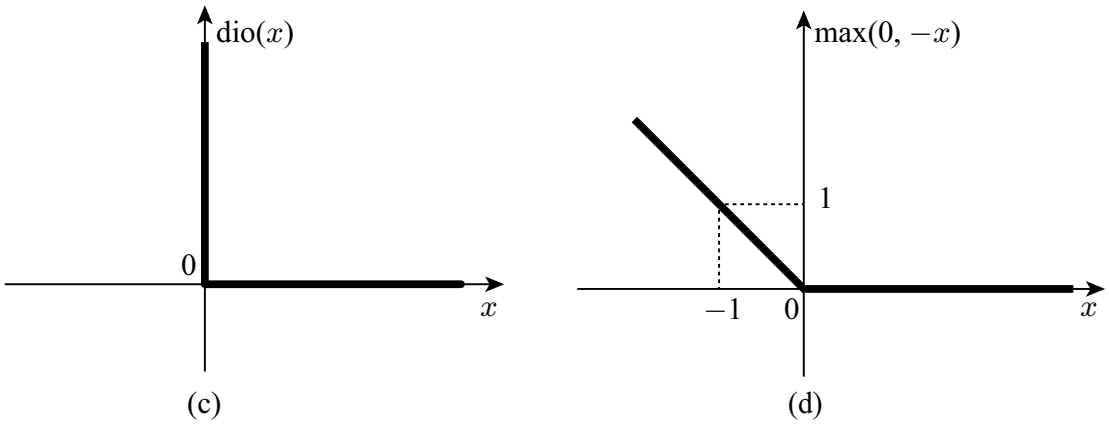

Figure 2.2: The diode function $\mathrm{dio}(x)$ and maximum function$\max(0, -x)$

where $x \in \mathbb{R}_+$. The following theorem is useful to rewrite DIs involving dio by ODEs:

Theorem 2. *For $x \in \mathbb{R}$ and $y \in \mathbb{R}_+$, the following relation holds true:*

$$y \in \mathrm{dio}(x + y) \Leftrightarrow y = \max(0, -x). \tag{2.5}$$

Proof. : A proof can be given as follows:

$$\begin{aligned} y \in \mathrm{dio}(x + y) &\Leftrightarrow (y = 0 \wedge x + y > 0) \vee (y \geq 0 \wedge x + y = 0) \\ &\Leftrightarrow (y = 0 \wedge x > 0) \vee (y \geq 0 \wedge y = -x) \Leftrightarrow y = \max(0, -x). \end{aligned}$$

□

The graphs of $\mathrm{dio}(x)$ and $\max(0, -x)$ are illustrated as Fig. 2.2(a) and Fig. 2.2(b), respectively.

2.3 General notations

It must be noted that Theorem 1 and Theorem 2 are special cases of the following relation, which has been used in, e.g., [18, Appendix A.3], [19, eq.(2)] and [67, eq.(4)]:

$$x - y \in N_S(y) \Leftrightarrow y = \mathrm{prox}(S, x). \tag{2.6}$$

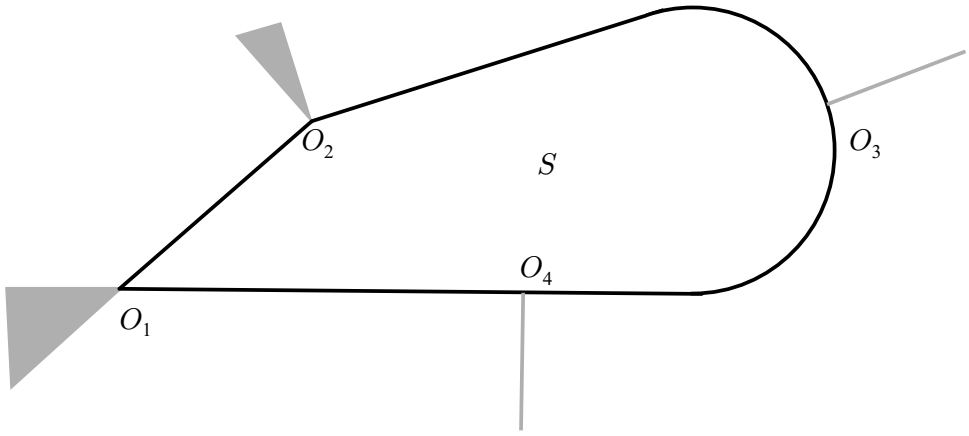

Figure 2.3: The normal cone of the set S at O_1, O_2, O_3, and O_4.

Here, $x \in \mathbb{R}^n$, $y \in S \subset \mathbb{R}^n$, S is a closed convex set, and $N_S(y)$ is the normal cone to the set S at y. The normal cone $N_S(y)$ is defined as follows:

$$N_S(y) = \begin{cases} \{z \in \mathbb{R}^n | z^T(y - \xi) \geq 0, \forall \xi \in S\}, & \text{if } y \in S \\ \emptyset & \text{otherwise.} \end{cases} \tag{2.7}$$

Examples of two dimensional normal cone $N_S(y)$ to the set S at the points O_1, O_2, O_3, and O_4 are illustrated in Fig. 2.3. The normal cones $N_S(y)$ at those points are colored with gray.

The function $\mathrm{prox}(S, x)$ represents the "proximal point" defined as follows:

$$\mathrm{prox}(S, x) \triangleq \underset{z \in S}{\operatorname{argmin}} \, \|z - x\|^2. \tag{2.8}$$

Theorem 1 and Theorem 2 can be obtained by using the relation (2.6) with $S = \{z \in \mathbb{R}^n \,|\, \|z\| \leq Z\}$ and $S = \mathbb{R}_+$, respectively.

Chapter 3

Mechanical systems involving Coulomb friction and rigid unilateral contact

Nonsmooth mechanical systems, which are mechanical systems involving Coulomb friction and rigid unilateral contact, are usually described as DIs. Those DIs may be approximated by ordinary differential equations (ODEs) by simply smoothing the discontinuities. Such approximations, however, can produce unrealistic behaviors because the discontinuous natures of the original DIs are lost. This chapter presents a new algebraic procedure to approximate DIs describing nonsmooth mechanical systems by ODEs with preserving the discontinuities. The procedure is based on the fact that the DIs can be approximated by differential algebraic inclusions (DAIs) and thus they can be equivalently rewritten as ODEs. The procedure is illustrated by some examples of nonsmooth mechanical systems with simulation results obtained by the fourth-order Runge-Kutta method.

The rest of this chapter is organized as follows. Section 3.1 overviews previous approximation methods for Coulomb friction and rigid unilateral contact. Section 3.2 gives the main contribution of the work. Section 3.3 provides two example applications of the new method. Finally, concluding remarks are given in Section 3.4.

★ The content of this chapter is partially published in [33].

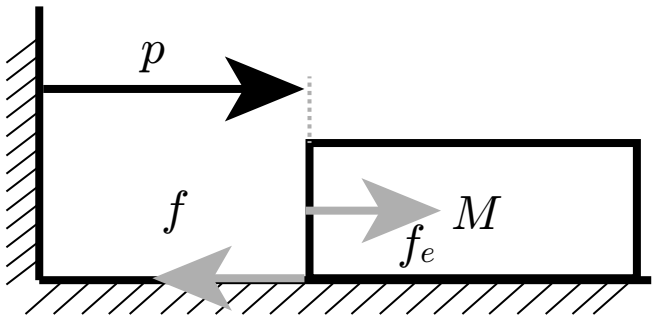

Figure 3.1: One physical interpretation of (3.1)

3.1 Previous simulation approaches

3.1.1 Coulomb friction

Let us consider the situation where a rigid mass $M > 0$, of which the position is $p \in \mathbb{R}^r (r \in \{1, 2\})$, is sliding on a fixed surface, as shown in Fig. 3.1. Let us assume that it is subject to the Coulomb friction force $f \in \mathbb{R}$ and an external force $f_e \in \mathbb{R}$. Then, the equation of motion of the mass is described as the following DI:

$$M\ddot{p} = f_e - f \tag{3.1}$$

where

$$f \in F\mathrm{sgn}(\dot{p}) \tag{3.2}$$

and $F > 0$ is the magnitude of kinetic friction force[1]. The direct integration of (3.1)(3.2) is difficult since the value of $\mathrm{sgn}(\dot{p})$ is not determined at $\dot{p} = 0$, according to the definition (2.1) of sgn.

Some previous friction models can be viewed as approximations of (3.2). One simple way is to employ a threshold velocity [13, 68] below which the velocity is considered zero. This method may be useful to avoid the discontinuity in (3.2) but the non-physical threshold

[1]Common definitions of Coulomb friction assume that the static friction force can be larger than the kinetic friction force. This chapter leaves this out of consideration and assumes that the maximum static friction force is equal to the kinetic friction force.

can produce unrealistic artifacts. Another way is to employ a new state variable which usually can be interpreted as the displacement of a viscoelastic element. For example, LuGre friction model [21, 31] without Stribeck effect can be described as follows:

$$\dot{a} = \dot{p} - \frac{K\|\dot{p}\|a}{F} \tag{3.3a}$$

$$f = Ka + B(\dot{p} - K\|\dot{p}\|a/F) + D\dot{p} \tag{3.3b}$$

where $a \in \mathbb{R}^r$ is the new state variable, $K > 0$ is a sufficiently large constant and $B, D > 0$ are constants appropriately chosen to suppress the oscillation in p. Dahl friction model [20] is a special case of LuGre friction model with $D = B = 0$. A disadvantage of those two models is that they produce unbounded positional drift in the static friction state under oscillatory external force even smaller than the maximum static friction force [69, 70].

Another type of regularized friction models are proposed by Kikuuwe et al. [69, Sec.III.C] and Bastien and Lamarque [71] based on Backward-Euler method, and by Kikuuwe and Fujimoto [72] based on a modified Runge-Kutta method. A downside of their models is that they restrict the choice of methods for time integration.

In hard-constraint approaches, the equations of motion are discretized along time by Euler-like methods. Those discretized equations are usually formulated into complementarity problems, which are then numerically solved. The literature includes some complementarity formulations of Coulomb friction in one-dimensional space [8, 73] and in multi-dimensional space [74–77]. One exception is Kikuuwe et al.'s approach [69, Sec III.A], in which the discretized equation in a very simple case is analytically solved by the application of Theorem 2 in the present chapter.

3.1.2 Rigid unilateral contact

Let us consider the one-dimensional system composed of a rigid mass M, of which the position is $p \in \mathbb{R}$, and a fixed rigid wall whose position coincides with the origin, as shown in Fig. 3.2. The rigid mass is subject to an external force $f_e \in \mathbb{R}$. Then, the equation of

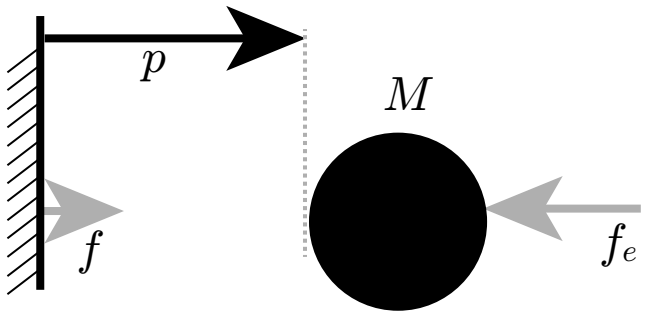

Figure 3.2: One physical interpretation of (3.4)

motion of the rigid mass is described as the following DI:

$$M\ddot{p} = f - f_e \tag{3.4}$$

where

$$f \in \mathrm{dio}(p). \tag{3.5}$$

The integration of (3.4)(3.5) is also difficult due to $\mathrm{dio}(p)$, whose value is not determined at $p = 0$.

One of trivial methods to approximately realize the contact force f in (3.5) is as follows [18, 72, 78]:

$$f = \begin{cases} -Kp - B\dot{p} & \text{if } p \leq 0 \\ 0 & \text{if } p > 0 \end{cases} \tag{3.6}$$

where K is a sufficiently large positive constant and B is a positive constant large enough to suppress the oscillation in p. This force law can be viewed as a linear viscoelastic contact model with the stiffness K and the viscosity B. As pointed out in [79, 80], one drawback of (3.6) is that it produces an unnatural sucking force toward the wall. This drawback may be

overcome by using the following slightly different one:

$$f = \begin{cases} \max(0, -Kp - B\dot{p}) & \text{if } p \leq 0 \\ 0 & \text{if } p > 0. \end{cases} \tag{3.7}$$

However, both (3.6) and (3.7) are discontinuous with respect to p and $\dot{p}$. Thus, they are not suitable for the use with common ODE solvers.

As another example, the nonlinear viscoelastic contact model proposed by Hunt and Crossley [79] can also be viewed as an approximation of rigid unilateral contact. This model was extended in [12, 55, 81] and empirically validated in [59, 60, 82]. This model is continuous with respect to p and $\dot{p}$, but it can also produce unnatural sucking force when $\dot{p}$ is large.

In hard-constraint approaches for rigid unilateral contact, the equations of motion are usually discretized by Euler-like methods and then solved numerically [8, 9, 73, 75, 83]. A different approach is in [18, Sec.1.4.3.2][80] where the discretized equations in very simple cases are solved analytically. Those methods can be used only with Euler-like methods.

3.2 New simulation approach

In this section, new ODE approximations are introduced for (3.1)(3.2) and (3.4)(3.5). Based on those simple approximations, a general procedure is presented for approximating nonsmooth mechanical systems involving many rigid-unilateral and Coulomb-frictional contacts.

3.2.1 Coulomb friction

The new approach for approximating (3.2) is motivated by Kikuuwe et al.'s work [69]. Their work (specifically, model-C in [69]) provides an idea to approximate (3.2) by the following DAI:

$$0 \in K(a + \beta\dot{a}) - F\mathrm{sgn}(\dot{p} - \dot{a}) \tag{3.8a}$$

$$f = K(a + \beta\dot{a}). \tag{3.8b}$$

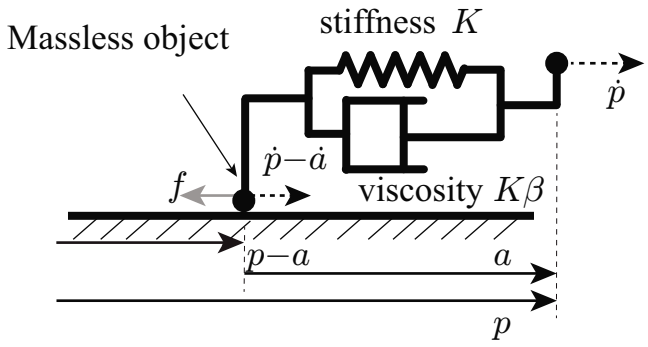

Figure 3.3: A physical interpretation of (3.8).

Here, $a \in \mathbb{R}^r$ is a state variable newly introduced, $K > 0$ is a sufficiently large constant and $\beta > 0$ is a constant appropriately chosen to suppress the oscillation in p. A physical interpretation of the approximation (3.8) can be illustrated as Fig. 3.3. A friction force described by $F\mathrm{sgn}(\dot{p}-\dot{a})$ acts on a massless object whose velocity is $\dot{p}-\dot{a}$, and a viscoelastic element with the stiffness K and the viscosity $K\beta$ produces the force f in (3.8b), which exactly balances the friction force.

In Kikuuwe et al.'s method, (3.8a) is discretized by Backward-Euler method, e.g., $\dot{a}$ is replaced by $(a_k - a_{k-1})/T$ where T denotes the timestep size and the subscripts denote time indices, and then it is analytically solved with respect to a_k by using Theorem 1. In Bastien and Lamarque's model [71], a set of inclusions and equations with similar form to (3.8), are also discretized by Back-Euler method and then analytically solved.

The observation that motivated the new approach is that, (3.8) can be solved without using the Backward-Euler method. By the direct application of Theorem 1, (3.8) can be equivalently rewritten as the following ODE:

$$\dot{a} = (\mathrm{sat}(F/K, a + \beta\dot{p}) - a)/\beta \tag{3.9a}$$

$$f = K\mathrm{sat}(F/K, a + \beta\dot{p}). \tag{3.9b}$$

As far as the author are aware, the literature includes no computational methods making use of the equivalence between DAIs of the form of (3.8) and ODEs of the form of (3.9).

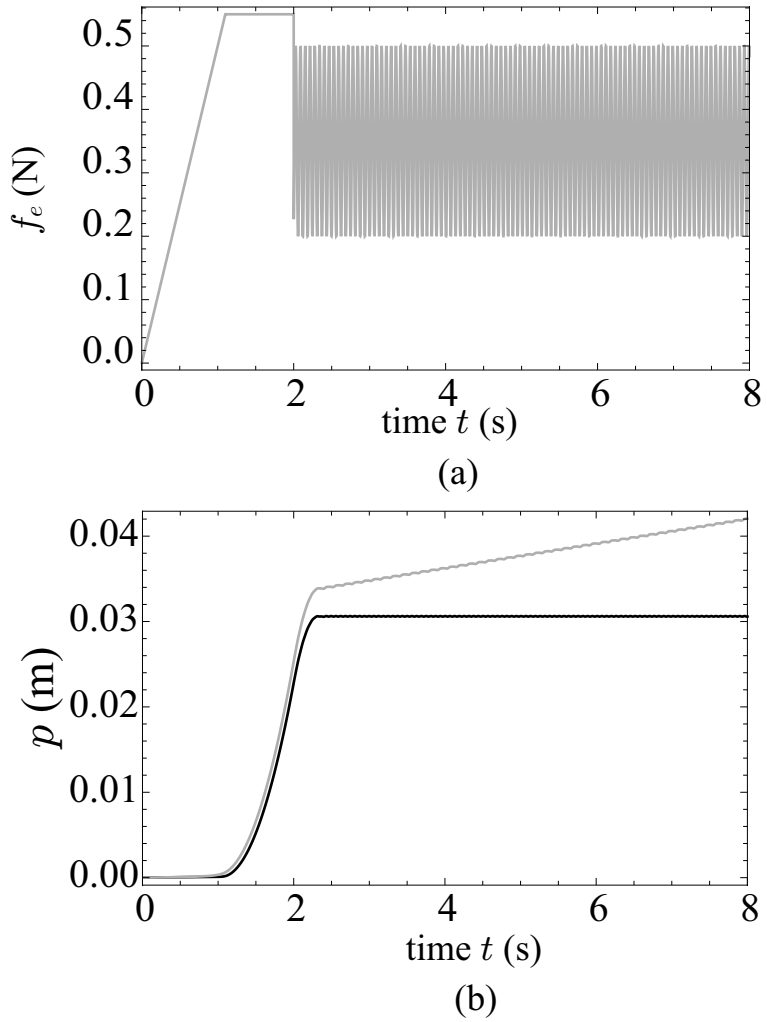

Figure 3.4: Simulation of the system (3.1); (a) provided external force f_e described as (3.11); (b) simulation results by RK4 with the timestep size 0.001s. The parameters are chosen as; $M = 1$ kg, $F = 0.5$ N, $K = 5 \times 10^3$ N/m, $\beta = 2 \times 10^{-3}$ s. The initial conditions are; $p = 0$ m, $\dot{p} = 0$ m/s.

After replacing (3.2) by (3.9b) and appending (3.9a) to the state-space model, the system

(3.1)(3.2) is approximated by the following ODE:

$$\frac{\mathrm{d}}{\mathrm{d}t}\begin{bmatrix} \dot{p} \\ p \\ a \end{bmatrix} = \begin{bmatrix} (f_e - K\mathrm{sat}(F/K, a + \beta\dot{p}))/M \\ \dot{p} \\ (\mathrm{sat}(F/K, a + \beta\dot{p}) - a)/\beta \end{bmatrix}. \tag{3.10}$$

Fig. 3.4 shows the simulation result by using the ODE (3.10) with RK4. To illustrate the advantage of this method, it also presents the result of LuGre model (3.3) combined with (3.1). In the simulation, an external force f_e was chosen as

$$f_e = \begin{cases} \min(0.55, 0.5t)\ \mathrm{N} & \text{if } t < 2\ \mathrm{s} \\ 0.35 + 0.15\cos(100t)\ \mathrm{N} & \text{otherwise,} \end{cases} \tag{3.11}$$

which is, after $t = 2$s, oscillatory below the static friction level $F = 0.5$ N. As shown in Fig. 3.4(b), LuGre model produces unrealistic positional drift, which has been known in the literature (e.g.,[69, 70]), while the presented method (3.10) does not. This implies that (3.9) is a better approximation of (3.2) than (3.3).

It should be mentioned that, (3.9) is derived by relaxing the rigid constraint between f and $\dot{p}$ in (3.2) by introducing an auxiliary variable a that has its own dynamics. In this sense, the proposed method may be viewed to be similar to Baumgarte's method [84], in which constraints are relaxed to improve the numerical stability of the solutions of ODEs. One of concerns regarding models based on DIs is the existence and uniqueness of solution, as discussed by Bastien and Lamarque [71]. As for the case of (3.8), on the other hand, it is clear because (3.8) is equivalent to the ODE (3.9).

3.2.2 Rigid unilateral contact

The new approach for approximating (3.5) is a modification of the work by Kikuuwe and Fujimoto [80]. In their approach, (3.5) is approximated by the following DAI:

$$0 \in K(e + \beta\dot{e}) - \mathrm{dio}(p + e) \tag{3.12a}$$

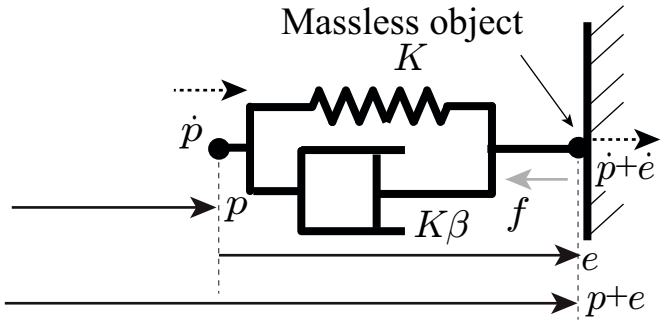

Figure 3.5: A physical interpretation of (3.12)

$$f = K(e + \beta\dot{e}) \tag{3.12b}$$

where K and β are appropriate positive constants, $e \in \mathbb{R}$ is a state variable newly introduced. A physical interpretation of (3.12) is illustrated as Fig. 3.5. Here, a massless object whose position is $p+e$ is connected to the mass through a viscoelastic element with the stiffness K and the viscosity $K\beta$. Due to the contact, the contact force $\mathrm{dio}(p + e)$ acts on the massless object and it balances the force f from the viscoelastic element. In Kikuuwe and Fujimoto's work, (3.12) was discretized by Backward-Euler method and then analytically solved by the application of Theorem 2. Unfortunately, (3.12) cannot be rewritten into an ODE because $\dot{e}$ cannot be obtained explicitly.

The new approach presented here is to add another term $\alpha\dot{e}$ to the argument of $\mathrm{dio}(\cdot)$, which yields the following DAI:

$$0 \in K(e + \beta\dot{e}) - \mathrm{dio}(p + e + \alpha\dot{e}) \tag{3.13a}$$

$$f = K(e + \beta\dot{e}) \tag{3.13b}$$

where $\alpha > 0$ is another appropriate constant. By using Theorem 2, (3.13) can be equivalently rewritten as the following ODE:

$$\dot{e} = \max(-e/\beta, -(p + e)/\alpha) \tag{3.14a}$$

$$f = K\max(0, e - \beta(p + e)/\alpha). \tag{3.14b}$$

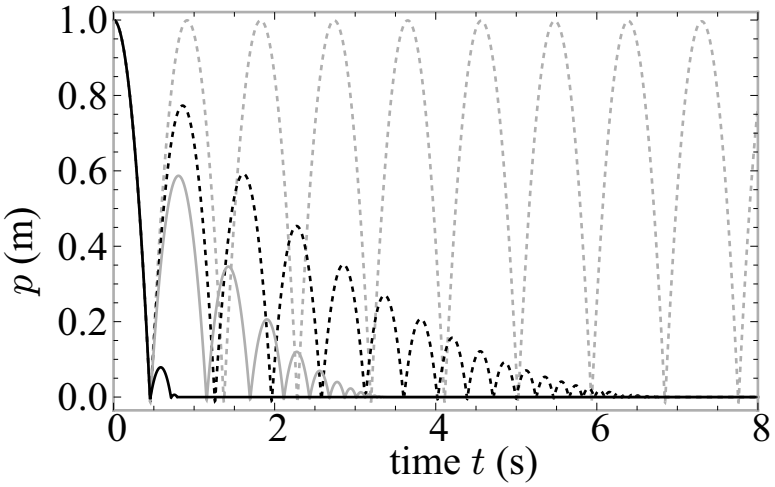

Figure 3.6: Simulation of the system (3.16) by RK4 with the timestep size 0.001s. The parameters are chosen as; $M = 1$ kg, $f_e = -9.8$ N, $K = 10^5$ N/m, $\beta = 0.01$ s, $\alpha = 0.01$ s(gray dashed), 0.007 s(black dashed), 0.005 s(gray solid), 0.001 s(black solid). The initial conditions are; $p = 1$ m, $\dot{p} = 0$ m/s.

The equivalence between DAIs of the form of (3.13) and ODEs of the form of (3.14) has not been pointed out in the literature either. One can see that (3.14) is continuous with respect to p, $\dot{p}$ and e and it does not produce sucking force because the right-hand side of (3.14b) is always positive. This features in contrast to the conventional methods (3.6) and (3.7), which are discontinuous, and to Hunt and Crosley's model [12, 55, 79], which produces a sucking force. It is also easy to see that (3.13), or equivalently, of (3.14) has a unique solution.

One possible interpretation of (3.13) and its equivalent expression (3.14) can be explained by defining $\tilde{e} \triangleq e + \alpha\dot{e}$. By using $\tilde{e}$, (3.13) can be rewritten as follows:

$$0 \in \mathcal{L}^{-1}\left[\ \frac{\mathcal{L}[K(\tilde{e} + \beta\dot{\tilde{e}})]}{1 + \alpha s}\ \right] - \mathrm{dio}(p + \tilde{e}) \tag{3.15a}$$

$$f = \mathcal{L}^{-1}\left[\ \frac{\mathcal{L}[K(\tilde{e} + \beta\dot{\tilde{e}})]}{1 + \alpha s}\ \right]. \tag{3.15b}$$

where $\mathcal{L}$ denotes the Laplace transform. By noting the similarity between (3.15) and (3.12),

one can see that force f in (3.15b) can be interpreted as a low-pass filtered viscoelastic force although it does not exist in the real world. When $\alpha = \beta$, (3.15) is equivalent to (3.12) with $\beta = 0$, which produces a perfectly elastic force. To preserve the effect of the viscous force and stability, it is presumable that α should be set smaller than β, although any tuning guidelines are not obtained yet.

By replacing (3.5) by (3.14b) and appending (3.14a) to the state-space model, the system (3.4)(3.5) is approximated by the following ODE:

$$\frac{\mathrm{d}}{\mathrm{d}t}\begin{bmatrix} \dot{p} \\ p \\ e \end{bmatrix} = \begin{bmatrix} (f_e + K\max(0, e - \beta(p+e)/\alpha))/M \\ \dot{p} \\ \max(-e/\beta, -(p+e)/\alpha) \end{bmatrix}. \tag{3.16}$$

A set of numerical simulation of the ODE (3.16) was performed with different α values and a fixed β value. Fig. 3.6 shows that the bouncing motion becomes smaller as α decreases. This is consistent with the interpretation based on (3.15), which implies that a smaller α strengthens the viscous effect in a high-frequency region. Detailed analysis on the relation between the parameter values and the achieved coefficient of restitution is left outside the scope of this chapter. What can be said is that the coefficient of restitution can be adjusted by appropriate choices of α and β on a trial-and-error basis.

3.2.3 Coulomb-frictional, rigid unilateral contact

The methods in Sec. 3.2.1 and Sec. 3.2.2 can be easily combined to describe a rigid unilateral contact involving Coulomb friction. Let us consider a rigid mass M of which the position is $p \in \mathbb{R}^3$ and a rigid frictional surface perpendicular to the z axis and including the origin. Then, the state-space model of the system can be described as the following DI:

$$\frac{\mathrm{d}}{\mathrm{d}t}\begin{bmatrix} p \\ \dot{p} \end{bmatrix} \in \left[\begin{array}{c} \dot{p} \\ \hline \dfrac{1}{M}\begin{bmatrix} \mu\mathrm{dio}(p_z)\mathrm{sgn}(\dot{p}_{xy}) \\ \mathrm{dio}(p_z) \end{bmatrix} \end{array}\right] \tag{3.17}$$

where $p = \left[\begin{array}{c} p_{xy}^T, \ p_z \end{array} \right]^T$, $p_{xy} \in \mathbb{R}^2$ and μ is the friction coefficient between the mass and the surface.

It must be noticed that (3.17) includes a multiplication of $\mathrm{dio}(\cdot)$ and $\mathrm{sgn}(\cdot)$. To integrate it, one must replace $\mathrm{dio}(\cdot)$ first and then replace $\mathrm{sgn}(\cdot)$ because the replacement of $\mathrm{sgn}(\cdot)$ involves its multiplicative factor (F in (3.2)) while that of $\mathrm{dio}(\cdot)$ can be done independently. In conclusion, the DI (3.17) can be approximated by the following ODE:

$$\frac{\mathrm{d}}{\mathrm{d}t} \left[\begin{array}{c} p \\ \hdashline \dot{p} \\ \hdashline e \\ a \end{array} \right] = \left[\begin{array}{c} \dot{p} \\ \hdashline \dfrac{1}{M} \left[\begin{array}{c} f_{xy}(p_z, \dot{p}_{xy}, e, a) \\ f_z(p_z, e) \end{array} \right] \\ \hdashline \max(-e/\beta_1, -(p_z + e)/\alpha) \\ (f_{xy}(p_z, \dot{p}_{xy}, e, a)/K_2 - a)/\beta_2 \end{array} \right] \tag{3.18}$$

where

$$f_z(p_z, e) \triangleq K_1 \max(0, e - \beta_1(p_z + e)/\alpha) \tag{3.19}$$

$$f_{xy}(p_z, \dot{p}_{xy}, e, a) \triangleq K_2 \mathrm{sat}(\mu f_z(p_z, e)/K_2\beta_2\dot{p}_{xy} + a) \tag{3.20}$$

and the parameters $\alpha, \beta_1, \beta_2, K_1$ and K_2 are appropriate positive constants. This ODE is obtained by replacing $\mathrm{dio}(p_z)$ in (3.17) by $f_z(p_z, e)$ and then replacing $f_z(p_z, e)\mathrm{sgn}(p_{xy})$ by $f_{xy}(p_z, \dot{p}_{xy}, e, a)$.

3.2.4 General procedure

Now we are in position to present the main contribution of the work. A mechanical system can be generally described by a DI in the following form:

$$\dot{x} \in \Phi(x) \tag{3.21}$$

where $x \in \mathbb{R}^n$ is the state vector of the system. Here, Φ is a function that contains $\mathrm{dio}(\cdot)$ and $\mathrm{sgn}(\cdot)$ in several places and may also contain single valued functions. Let us assume that, in Φ, m different arguments, denoted as $\psi_i(x)$, $i \in \{1, \cdots, m\}$, are used for $\mathrm{dio}(\cdot)$ and that l different arguments, denoted as $\theta_i(x)$, $i \in \{1, \cdots, l\}$, are used for $\mathrm{sgn}(\cdot)$. Here, $\psi_i : \mathbb{R}^n \to \mathbb{R}_+$ and $\theta_i : \mathbb{R}^n \to \mathbb{R}^r$, $r \in \{1, 2\}$, are continuous functions.

By applying the methods introduced in Sec. 3.2.1 and 3.2.2, $\Phi(x)$ can be approximated by the following procedure:

1. First, replace $\mathrm{dio}(\psi_i(x))$ by $K_{\mathrm{d}i} \max(0, e_i - \beta_{\mathrm{d}i}(\psi_i(x) + e_i)/\alpha_i)$, where $K_{\mathrm{d}i}$, $\beta_{\mathrm{d}i}$ and α_i are appropriate positive constants.

2. Next, let $\chi_i(x)$ denote the multiplicative factors of $\mathrm{sgn}(\theta_i(x))$, which are nonnegative continuous functions. Then, replace $\chi_i(x)\mathrm{sgn}(\theta_i)$ by $K_{\mathrm{s}i}\mathrm{sat}(\chi_i(x)/K_{\mathrm{s}i}, \beta_{\mathrm{s}i}\theta_i(x)+a_i)$, where $K_{\mathrm{s}i}$ and $\beta_{\mathrm{s}i}$ are appropriate positive constants.

3. Finally, append $\dot{e}_i = \max(-e_i/\beta_{\mathrm{d}i}, -(\psi_i(x) + e_i)/\alpha_i)$, $i \in \{1, \cdots, m\}$, and $\dot{a}_i = (\mathrm{sat}(\chi_i(x)/K_{\mathrm{s}i}, a_i + \beta_{\mathrm{s}i}\theta_i(x)) - a_i)/\beta_{\mathrm{s}i}$, $i \in \{1, \cdots, l\}$, to the state-space model.

With this procedure, the nonsmooth system (3.21) is approximated by the following ODE:

$$\frac{\mathrm{d}}{\mathrm{d}t}\begin{bmatrix} x \\ e_1 \\ \vdots \\ e_m \\ a_1 \\ \vdots \\ a_l \end{bmatrix} = \begin{bmatrix} \hat{\Phi}(x, e_1, \cdots, e_m, a_1, \cdots, a_l) \\ \max(-e_1/\beta_{\mathrm{d}1}, -(\psi_1(x) + e_1)/\alpha_1) \\ \vdots \\ \max(-e_m/\beta_{\mathrm{d}m}, -(\psi_m(x) + e_m)/\alpha_m) \\ (\mathrm{sat}(\chi_1(x)/K_{\mathrm{s}1}, a_1 + \beta_{\mathrm{s}1}\theta_1(x)) - a_1)/\beta_{\mathrm{s}1} \\ \vdots \\ (\mathrm{sat}(\chi_l(x)/K_{\mathrm{s}l}, a_l + \beta_{\mathrm{s}l}\theta_l(x)) - a_l)/\beta_{\mathrm{s}l} \end{bmatrix} \tag{3.22}$$

where $\hat{\Phi}(x, e_1, \cdots, e_m, a_1, \cdots, a_l)$ is the function $\Phi(x)$ in which the aforementioned replacements are made.

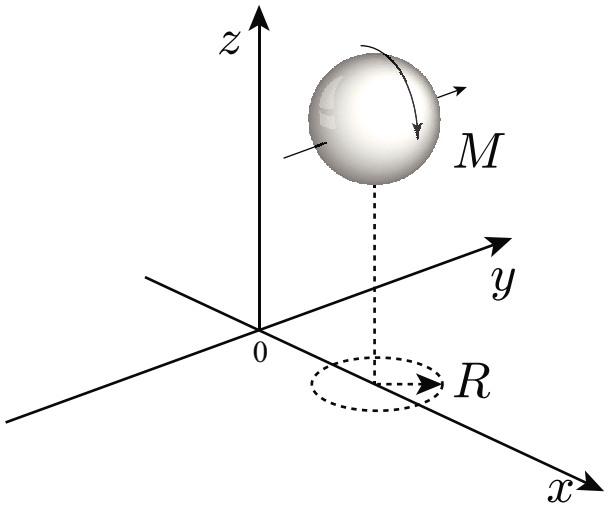

Figure 3.7: Example I: A rolling sphere with collision and slip. In the simulation, the parameters are chosen as; $M = 1$ kg, $R = 0.5$ m, $\mu = 0.1$ and the initial conditions are; $\dot{p} = [5.5, 0, 0]^T$ m/s, $p = [0, 0, 2R]^T$ m, $\omega = [0, 0, 0]^T$ rad/s.

The presented procedure cannot apply if the function $\Phi(x)$ includes a $\mathrm{sgn}(\cdot)$ whose multiplicative factor involves discontinuous functions other than $\mathrm{dio}(\cdot)$ and if $\chi_i(x)$ are not guaranteed to be nonnegative. The author, however, are not aware of nonsmooth mechanical systems that must be described by such $\Phi(x)$ functions. As illustrated in Sec. 3.3.2, the presented procedure can deal with such a complicated system as the one in Fig. 3.9.

3.3 Examples and simulation results

3.3.1 Example I: A rolling sphere with collision and slip

The presented approach is now illustrated by examples. Let us consider a system in which a spherical object with a uniform mass density falls onto a fixed rigid surface. The surface

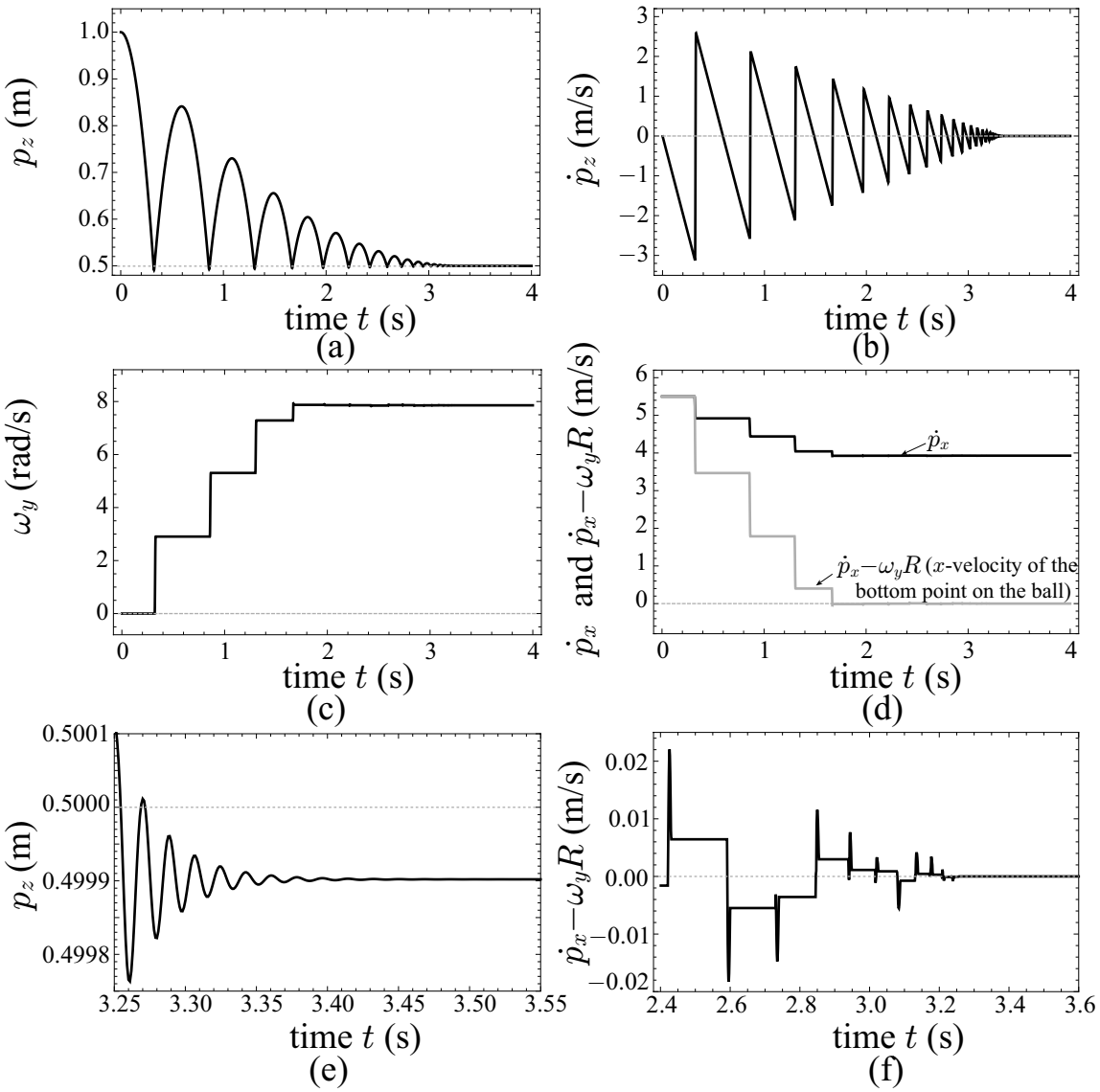

Figure 3.8: Simulation results of Example I by using (3.27) integrated by RK4 with the timestep size 0.001 s. The parameters are chosen as; $K_1 = K_2 = 1 \times 10^5$ N/m, $\beta_1 = \beta_2 = 4 \times 10^{-3}$ s, $\alpha = 2.8 \times 10^{-3}$ s.

includes the origin and is perpendicular to the z axis. This example is also introduced in [72] and a similar example is employed in [12]. Let $p \in \mathbb{R}^3$ be the position of the gravity center of the object, q be the unit quaternion representing the attitude of the object, and $\omega \in \mathbb{R}^3$ be

the angular velocity of the object. Let R and M be the radius and the mass of the object, respectively, and μ be the friction coefficient between the object and the surface. Then, the equations of motion of the object can be described as the following DI:

$$\frac{\mathrm{d}}{\mathrm{d}t}\begin{bmatrix} \dot{p} \\ \hdashline p \\ \hdashline \omega \\ \hdashline q \end{bmatrix} \in \begin{bmatrix} \dfrac{1}{M}\begin{bmatrix} -\mu \mathrm{dio}(p_z - R)\mathrm{sgn}(v(\dot{p},\omega)) \\ \mathrm{dio}(p_z - R) \end{bmatrix} - g \\ \hdashline \dot{p} \\ \hdashline \dfrac{5}{2MR^2}\left(d \times \begin{bmatrix} -\mu \mathrm{dio}(p_z - R)\mathrm{sgn}(v(\dot{p},\omega)) \\ \mathrm{dio}(p_z - R) \end{bmatrix}\right) \\ \hdashline Q(\omega, q) \end{bmatrix} \tag{3.23}$$

where

$$v(\dot{p},\omega) \triangleq [\dot{p}_x - \omega_y R,\ \dot{p}_y + \omega_x R]^T, \tag{3.24}$$

$Q : \mathbb{R}^3 \times \mathbb{R}^4 \to \mathbb{R}^4$ denotes an appropriate function that transforms ω into the quaternion rate $\dot{q}$, $d \triangleq [0, 0, -R]^T$ and $g \triangleq [0, 0, 9.8\mathrm{m/s}^2]^T$.

According to the procedure presented in Sec. 3.2.4, the DI (3.23) can be approximated by an ODE in the following procedure. First, one should replace $\mathrm{dio}(p_z - R)$ by

$$\psi(p_z, e) \triangleq K_1 \max(0, e - \beta_1(e + p_z - R)/\alpha) \tag{3.25}$$

where $e \in \mathbb{R}$ and K_1, β_1 and α are appropriate positive constants. Then $\mu\mathrm{dio}(p_z - R)\mathrm{sgn}(v(\dot{p},\omega))$ becomes $\mu\psi(p_z, e)\mathrm{sgn}(v(\dot{p},\omega))$. Next, $\mu\psi(p_z, e)\mathrm{sgn}(v(\dot{p}, \omega))$ should be replaced by

$$\theta(p_z, v(\dot{p},\omega), e, a) \triangleq K_2 \mathrm{sat}(\mu\psi(p_z, e)/K_2, a + \beta_2 v(\dot{p},\omega)) \tag{3.26}$$

where $a \in \mathbb{R}^2$ and K_2 and β_2 are positive constants appropriately chosen. Finally, ODEs defining the behaviors of e and a should be appended to (3.23). Then, (3.23) is approximated by the following ODE:

$$\frac{\mathrm{d}}{\mathrm{d}t}\begin{bmatrix} \dot{p} \\ \hdashline p \\ \hdashline \omega \\ \hdashline q \\ e \\ a \end{bmatrix} = \begin{bmatrix} \dfrac{1}{M}\begin{bmatrix} -\theta(p_z, v(\dot{p},\omega), e, a) \\ \psi(p_z, e) \end{bmatrix} - g \\ \hdashline \dot{p} \\ \hdashline \dfrac{5}{2MR^2}\left(d \times \begin{bmatrix} -\theta(p_z, v(\dot{p},\omega), e, a) \\ \psi(p_z, e) \end{bmatrix}\right) \\ \hdashline Q(\omega, q) \\ \max(-e/\beta_1, -(e + p_z - R)/\alpha) \\ (\theta(p_z, v(\dot{p},\omega), e, a)/K_2 - a)/\beta_2 \end{bmatrix}. \tag{3.27}$$

Fig. 3.8 shows the result of the simulation by using (3.27) with RK4. Here, K_1 and K_2 are set as high as possible to achieve small penetrations during collisions, and β_1, β_2 and α are chosen based on some trials and errors. Fig. 3.8(a) and Fig. 3.8(b) show the bouncing motion in the z direction and Fig. 3.8(c) and Fig. 3.8(d) show the transition from pure translation (slipping in contact) to pure rolling. One can see that those behaviors are properly simulated, which supports the validity of the approximation (3.18) of the original DI (3.17).

3.3.2 Example II: Multiple friction with multiple rigid unilateral contacts

Next example is the application of the presented method to a system involving many frictional contacts interacting to one another. Let us consider a planar system illustrated in Fig. 3.9, which consists of a conveyor moving at a constant velocity u, a spring with the stiffness K_s, two rigid objects M_1 and M_2 and a rigid vertical wall. The object M_1 can move freely in the horizontal direction and is subject to the elastic force from a spring K_s in the vertical direction. It is assumed that the objects do not rotate. The coefficients of friction between the wall and M_1, between M_1 and M_2 and between M_2 and the conveyor are μ_1, μ_2 and μ_3, respectively. The state vector is defined as $x \triangleq [p^T, \dot{p}^T]^T$ where

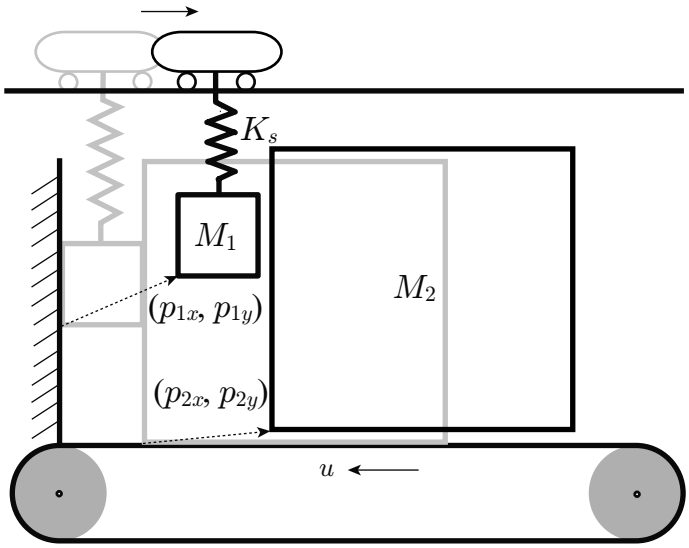

Figure 3.9: Example II: Multiple friction contacts with multiple rigid unilateral contacts. In the simulation, the parameters were chosen as; $\mu_1 = \mu_2 = \mu_3 = 0.5$, $M_1 = 0.5$ kg, $M_2 = 1$ kg, $K_s = 100$ N/m, $u = 1$ m/s and the initial conditions are; $p = [0, 0.25, 0.05, 0]^T$ m, $\dot{p} = [0, 0, 0, 0]^T$ m/s.

$p = [p_{1x}, p_{1y}, p_{2x}, p_{2y}]^T$ where $[p_{1x}, p_{1y}]^T$ and $[p_{2x}, p_{2y}]^T$ denote the positions of M_1 and M_2, respectively. The object M_1 is regarded to be at $[0, 0]^T$ when it is in contact with the wall and the spring balances the gravity. The object M_2 is regarded to be at $[0, 0]^T$ when it is in contact with the conveyor and the object M_2 being at its $[0, 0]^T$. Then, the state-space model of the system can be described as the following DI:

$$\frac{\mathrm{d}}{\mathrm{d}t}\begin{bmatrix} p \\ \hdashline \dot{p} \end{bmatrix} \in \begin{bmatrix} \dot{p} \\ \hdashline (\mathrm{dio}(p_{1x}) - \mathrm{dio}(p_{2x} - p_{1x}))/M_1 \\ (-\Omega_1(x) - \Omega_2(x) - K_{s_1} p_{1y})/M_1 \\ (-\Omega_3(x, u) + \mathrm{dio}(p_{2x} - p_{1x}))/M_2 \\ (\Omega_2(x) + \mathrm{dio}(p_{2y}))/M_2 - g \end{bmatrix} \tag{3.28}$$

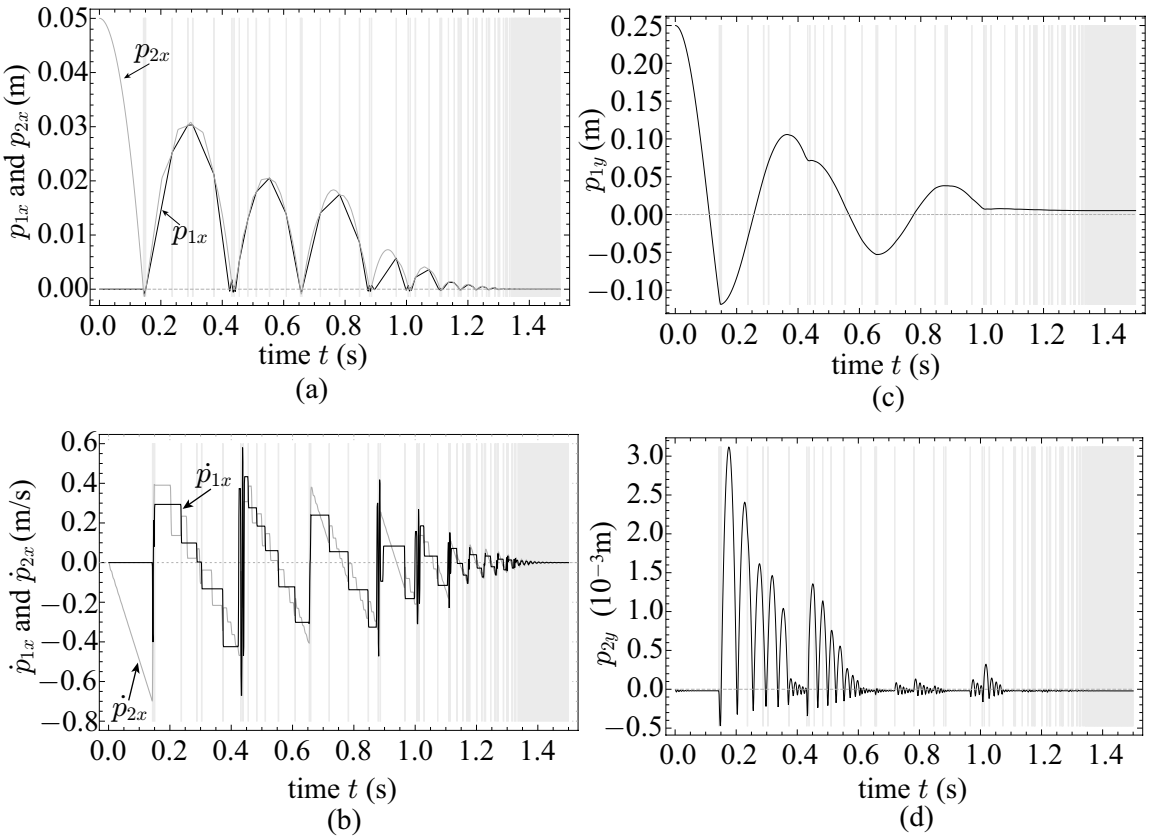

Figure 3.10: Simulation results of Example II by using (3.35) integrated by RK4 with timestep size 0.001s. The gray regions indicate the time periods in which the objects M_1 and M_2 are in contact with each other. The parameters are chosen as; $K_i = 5 \times 10^5$ N/m, $\beta_i = 2 \times 10^{-3}$ s ($\forall i \in \{1, \cdots, 6\}$), $\alpha_i = 1.6 \times 10^{-3}$ s ($\forall i \in \{1, 2, 3\}$).

where $\Omega_1(x) \triangleq \mu_1 \mathrm{dio}(p_{1x})\mathrm{sgn}(\dot{p}_{1y})$, $\Omega_2(x) \triangleq \mu_2 \mathrm{dio}(p_{2x} - p_{1x})\mathrm{sgn}(\dot{p}_{1y} - \dot{p}_{2y})$ and $\Omega_3(x, u) \triangleq \mu_3 \mathrm{dio}(p_{2y})\mathrm{sgn}(\dot{p}_{2x} + u)$.

According to the procedure presented in Sec. 3.2.4, the DI (3.28) is approximated by an ODE in the following procedure. First, one should replace $\mathrm{dio}(p_{1x})$, $\mathrm{dio}(p_{2x} - p_{1x})$ and $\mathrm{dio}(p_{2y})$ by

$$\psi_1(x, e_1) \triangleq K_1 \max(0, e_1 - \beta_1(p_{1x} + e_1)/\alpha_1), \tag{3.29}$$

$$\psi_2(x, e_2) \triangleq K_2 \max(0, e_2 - \beta_2(p_{2x} - p_{1x} + e_2)/\alpha_2), \tag{3.30}$$

$$\psi_3(x, e_3) \triangleq K_3 \mathrm{max}(0, e_3 - \beta_3(p_{2y} + e_3)/\alpha_3), \tag{3.31}$$

respectively, where K_i, β_i and α_i ($i \in \{1, 2, 3\}$) are appropriate positive constants. Then, $\Omega_1(x)$, $\Omega_2(x)$ and $\Omega_3(x, u)$ are found to be replaced by $\mu_1\psi_1(x, e_1)\mathrm{sgn}(\dot{p}_{1y})$, $\mu_2\psi_2(x, e_2)\mathrm{sgn}(\dot{p}_{1y} - \dot{p}_{2y})$ and $\mu_3\psi_3(x, e_3)\mathrm{sgn}(\dot{p}_{2x}+u)$, respectively. Next, they should be replaced by $\theta_1(x, e_1, a_1)$, $\theta_2(x, e_2, a_2)$ and $\theta_3(x, u, e_3, a_3)$, respectively, where

$$\theta_1(x, e_1, a_1) \triangleq K_4 \mathrm{sat}(\mu_1\psi_1(x, e_1)/K_4, a_1 + \beta_4\dot{p}_{1y}), \tag{3.32}$$

$$\theta_2(x, e_2, a_2) \triangleq K_5 \mathrm{sat}(\mu_2\psi_2(x, e_2)/K_5, a_2 + \beta_5(\dot{p}_{1y} - \dot{p}_{2y})), \tag{3.33}$$

$$\theta_3(x, u, e_3, a_3) \triangleq K_6 \mathrm{sat}(\mu_3\psi_3(x, e_3)/K_6, a_3 + \beta_6(\dot{p}_{2x} + u)), \tag{3.34}$$

and K_i and β_i ($i \in \{4, 5, 6\}$) are appropriate constants. Finally, the differential equations defining the behaviors of e_i and a_i ($i \in \{1, 2, 3\}$) should be appended to (3.28). Then, (3.28) is approximated by the following ODE:

$$\frac{\mathrm{d}}{\mathrm{d}t}\begin{bmatrix} p \\ \hdashline \dot{p} \\ \hdashline e_1 \\ e_2 \\ e_3 \\ a_1 \\ a_2 \\ a_3 \end{bmatrix} = \begin{bmatrix} \dot{p} \\ \hdashline (\psi_1(x, e_1) - \psi_2(x, e_2))/M_1 \\ (-K_s p_{1y} - \theta_1(x, e_1, a_1) - \theta_2(x, e_2, a_2))/M_1 \\ (-\theta_3(x, u, e_3, a_3) + \psi_2(x, e_2))/M_2 \\ (\theta_2(x, e_2, a_2) + \psi_3(x, e_3))/M_2 - g \\ \hdashline \mathrm{max}(-e_1/\beta_1, -(p_{1x} + e_1)/\alpha_1) \\ \mathrm{max}(-e_2/\beta_2, -(p_{2x} - p_{1x} + e_2)/\alpha_2) \\ \mathrm{max}(-e_3/\beta_3, -(p_{2y} + e_3)/\alpha_3) \\ (\theta_1(x, e_1, a_1)/K_4 - a_1)/\beta_4 \\ (\theta_2(x, e_2, a_2)/K_5 - a_2)/\beta_5 \\ (\theta_3(x, e_3, a_3)/K_6 - a_3)/\beta_6 \end{bmatrix}. \tag{3.35}$$

A numerical simulation was performed by using the ODE (3.35) with RK4. The results

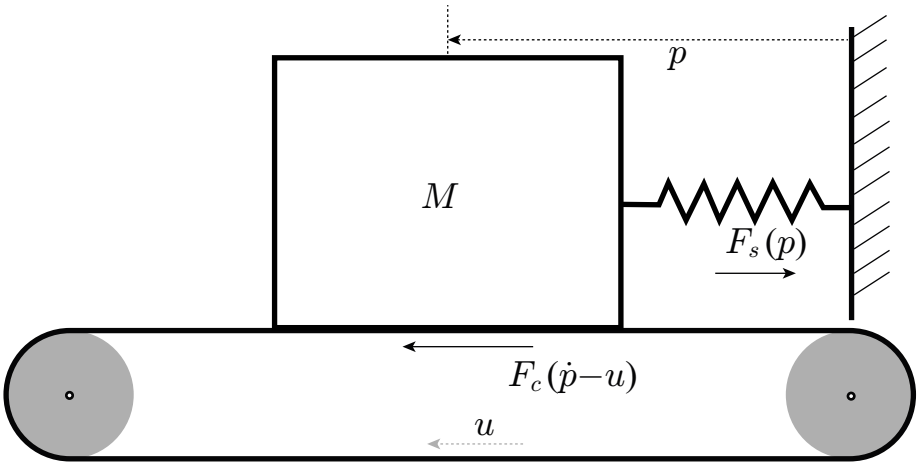

Figure 3.11: Example III: Periodic motion. In the simulation, the parameters were chosen as; $F = 0.2$ N, $M = 1$ kg, $k_1 = 1$ N/m, $k_2 = 1$ N/m^3, $u = 1$ m/s, $V = 1$ m/s, and the initial conditions are adopted from [1] for comparison; $p = 1.19149$ m, $w = 0$ m/s.

are shown in Fig. 3.10. Here, again, K_i are set as high as possible to achieve small penetrations during collisions, and β_i and α_i are chosen based on some trials and errors. The time periods indicated by the gray regions are those in which the objects M_1 and M_2 are in contact to each other. Fig. 3.10(a) shows the horizontal bouncing motion of M_1 and M_2, which eventually converges. Fig. 3.10(b) shows the vertical motion of M_1, which exhibits nonsmooth changes in the velocity during the contact with M_2, being influenced by the friction force. The vertical position of M_1 does not converge to zero because of the static friction forces from the wall and M_2. Fig. 3.10(c) shows the vertical motion of M_2, which determines the normal force from the conveyor to M_2. It properly shows the influence in the normal force from the friction force acting on the side face. Those results are physically plausible and indicate the validity of the approximation (3.35) of the original DI (3.28).

3.3.3 Example III: Periodic motion

This section shows the application of the proposed method to a system exhibiting periodic motion. Let us consider the system illustrated by Fig. 3.11, which has been investigated by Awrejcewicz et al. [1]. Fig. 3.11 shows that a mass M, of which the position is denoted as $p \in \mathbb{R}$, rests on a conveyor rolling with a constant velocity $u \in \mathbb{R}$. The mass is subjected

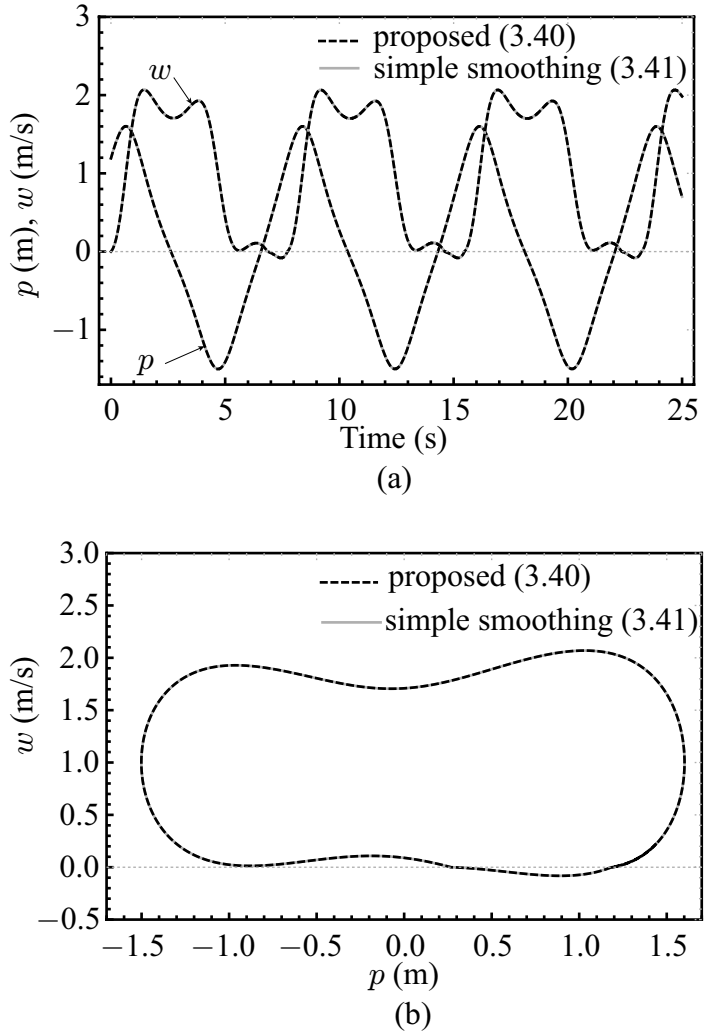

Figure 3.12: Simulation results of Example III by using (3.40) and (3.41) integrated by RK4 with timestep size 0.001 s. The parameters in (3.40) are chosen as; $K = 1 \times 10^5$ N/m, $\beta = 0.5$ s. The parameter in (3.41) is chosen as $\epsilon = 10^{-5}$ m/s.

to a nonlinear spring force $F_s(p)$ and a rate-dependent friction force $F_c(\dot{p} - u)$. Then, the system is described as the following equation:

$$M\ddot{p} + F_s(p) - F_c(\dot{p} - u) = 0. \tag{3.36}$$

Here, let us assume that $F_s(p)$ and $F_c(\dot{p}-u)$ are defined as follows:

$$F_s(p) \triangleq -k_1 p + k_2 p^3 \tag{3.37}$$

$$F_c(\dot{p}-u) \triangleq -\frac{F}{V+|\dot{p}-u|}\mathrm{sgn}(\dot{p}-u) \tag{3.38}$$

where k_1, k_2, F and V are positive constants. By using a new variable $w \triangleq u - \dot{p}$, one can rewrite (3.36) into the following DI:

$$\frac{\mathrm{d}}{\mathrm{d}t}\begin{bmatrix} p \\ \hdashline w \end{bmatrix} \in \begin{bmatrix} u-w \\ \hdashline \dfrac{1}{M}\left(k_2 p^3 - k_1 p - \dfrac{F}{V+|w|}\mathrm{sgn}(w)\right) \end{bmatrix}. \tag{3.39}$$

According to the procedure presented in Section 3.2.4, (3.39) is approximated as follows:

$$\frac{\mathrm{d}}{\mathrm{d}t}\begin{bmatrix} p \\ \hdashline w \\ \hdashline a \end{bmatrix} = \begin{bmatrix} u-w \\ \hdashline \dfrac{1}{M}\left(k_2 p^3 - k_1 p - \mathrm{sat}\left(\dfrac{F}{V+|w|}, Ka + K\beta w\right)\right) \\ \hdashline \left(\mathrm{sat}\left(\dfrac{F}{(V+|w|)K}, a+\beta w\right) - a\right)/\beta \end{bmatrix} \tag{3.40}$$

where a is a new state variable and K and β are positive parameters. In contrast, Awrejcewicz et al. [1] used the following equation to approximate (3.39):

$$\frac{\mathrm{d}}{\mathrm{d}t}\begin{bmatrix} p \\ \hdashline w \end{bmatrix} = \begin{bmatrix} u-w \\ \hdashline \dfrac{1}{M}\left(k_2 p^3 - k_1 p - \dfrac{F\mathrm{sat}(\epsilon, w)}{(V+\max(|w|,\epsilon))\epsilon}\right) \end{bmatrix} \tag{3.41}$$

where $0 < \epsilon \ll V$ is a parameter. This approximation was obtained by simply replacing the discontinuity by a linear function of a constant slope in the region $|w| < \epsilon$. Awrejcewicz et al. [1] has shown that this approximation does reproduce periodic motion appropriately.

Fig. 3.12 shows the simulation results of the proposed approximation (3.40) and the simple smoothing (3.41). It shows that the proposed approximation (3.40) also provides

periodic solution, and it is very close to that of the simple smoothing (3.41). Considering that the result of (3.41) has been analytically validated through Tichonov theorem in [1], one can see that the result of the new approximation (3.40) is also valid.

3.4 Summary

This chapter has introduced a new method to approximate DIs describing nonsmooth mechanical systems involving Coulomb friction and rigid unilateral contact by ODEs. A main difference of the new method from conventional regularization methods is that the resultant ODEs are equivalent to DAIs that are approximations of DIs. As a consequence, the approximated ODEs preserve important features of the original DIs such as static friction and always-repulsive contact force. An algebraic procedure for yielding the ODE approximations has been presented and has been illustrated by using some examples.

Future research should address the theoretical and numerical studies on the influence of the chosen parameters (K, α, β) on the system behavior. Currently there are no guidelines for the choice of the parameter values, thus they have been chosen through trial and error in the presented examples. In particular, the choice of α and β strongly influences the realized coefficient of restitution. Theoretical or empirical relations between the parameter values and the coefficient of restitution must be sought in the future study.

One limitation of the presented approach is that it is only for "lumped" contacts. In some situations, the contact force may be distributed across a contact area. It is unclear whether the presented approach is applicable or not to such situations. Anisotropic friction force and elastic contact, such as those seen in vehicle tires, would demand further extension of the presented approach.

Chapter 4

A friction model with realistic presliding behavior

This chapter proposes a multistate friction model by extending the previous single-state friction model introduced in Chapter 3. This new model is described as a set of continuous differential equations that describe both the presliding and sliding regimes in a unified expression. It reproduces major features of friction phenomena reported in the literature, such as the Stribeck effect, nondrifting property, stick-slip oscillation, presliding hysteresis with nonlocal memory, and frictional lag. Moreover, the new model does not produce unbounded positional drift or non-smooth forces, which are major problems of previous models due to the mathematical difficulty in dealing with transitions between the presliding and sliding regimes. The model is validated through comparison between its simulation results and empirical results in the literature.

The rest of this chapter is organized as follows. Section 4.1 overviews some related models of friction. Section 4.2 proposes the multistate model. Section 4.3 provides theoretical analysis on properties of the proposed model. Section 4.4 validates this model through simulations in comparisons with the GMS model in the literature. Finally, concluding remarks

★ Portions of the materials in this chapter are reprinted from *Tribology Letters*, vol. 51, no. 3, Xiaogang Xiong and Ryo Kikuuwe and Motoji Yamamoto, "A Multistate Friction Model Described by Continuous Differential Equations", pp. 513–523, 2013, as published in [85, 86], with permission from Springer (see Appendix A1) .

are given in Section 4.5.

4.1 Related work

4.1.1 LuGre model, single-state elastoplastic model, Leuven model and modified Leuven model

The LuGre model without the Stribeck effect has been reviewed in Chapter 3.1.1 as an approximation of the set-valued law (3.2). For easinesses of comparisons with other friction models, this model is rewritten here with the Stribeck effect and new parameter notations [21, 31]:

$$\dot{a} = v\left(1 - \operatorname{sgn}(v)\frac{\kappa a}{g(v)}\right) \tag{4.1a}$$

$$f = \kappa a + \sigma \dot{a}. \tag{4.1b}$$

Again, f is the friction force and v is the relative velocity between two surfaces in contact. From the physical point of view, a should be interpreted as the average deflection of asperities and $\kappa, \sigma \in \mathbb{R}_+$ are the stiffness and micro-damping coefficients, respectively. For simplicity and without loss of generality, the viscous component Dv of the friction force f in (4.1b) is not considered throughout this chapter. Function $g(v)$ describes the Stribeck effect, which can be typically described as follows [21, 31]:

$$g(v) \triangleq F_c + (F_s - F_c)e^{-|v/v_s|^\alpha}. \tag{4.2}$$

Here, F_c and F_s are the magnitude of kinetic friction force and static friction force, respectively. The parameter $\alpha \in \mathbb{R}_+$ and the Stribeck velocity v_s are constants. The LuGre model produces unbounded positional drift due to its inappropriate way of modeling the elastic deformation in the presliding regime [32].

The single state elastoplastic model [32] does not suffer from the unbounded positional drift problem. However, as pointed out in [35], this model produces unrealistic presliding hysteresis behaviors that do not show nonlocal memory. The Leuven model [24, 34] pro-

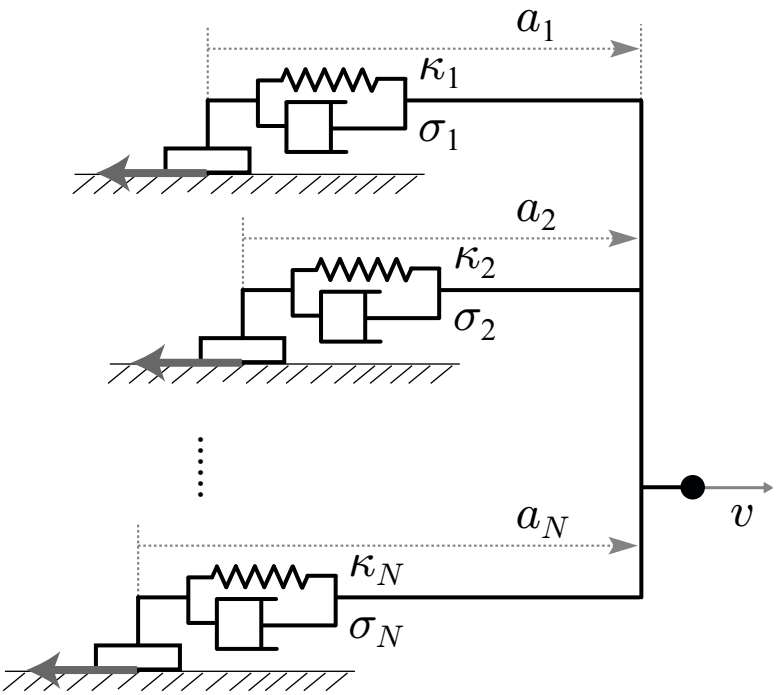

Figure 4.1: A physical interpretation of (4.3b) and (4.3b). In the sliding regime, the asperity deflections a_i evolve so that the elastic forces $|\kappa_i a_i|$ converge to $\lambda_i g(v)$. The total friction force f is the sum of the viscoelastic forces of the elements. Figure and caption are reprinted, with permission from Springer: Tribology letter, "A Multistate Friction Model Described by Continuous Differential Equations", vol. 51, no. 3, pp. 513–523, 2013, Xiaogang Xiong, Ryo Kikuuwe, and Motoji Yamamoto, Fig. 2 (see Appendix A1).

duces presliding hysteresis behaviors with nonlocal memory in the presliding regime, but as pointed out in [35], it has implementation difficulties since it requires additional stacks to store extreme force values. In contrast, the modified Leuven model [34] is free from those implementation difficulties. However, as pointed out and illustrated in [23, 35, 40], the force-position and force-velocity curves produced by this model do not exhibit an appropriate nondrifting property and frictional lag effect that agree with experimental data.

4.1.2 Generalized Maxwell-Slip friction model

The generalized Maxwell-slip (GMS) model [35] is a friction model that can be represented by a parallel connection of N elastoplastic elements, as illustrated in Fig. 4.1. This model is

described as follows [35–37]:

$$f = \sum_{i=1}^{N} (\kappa_i a_i + \sigma_i \dot{a}_i),\ i \in \{1, \cdots, N\} \tag{4.3a}$$

$$\dot{a}_i = \begin{cases} v & \text{if } s_i = \text{STICK} \\ \dfrac{C\lambda_i \text{sgn}(v)}{\kappa_i} \left(1 - \text{sgn}(v) \dfrac{\kappa_i a_i}{\lambda_i g(v)}\right) & \text{if } s_i = \text{SLIP} \end{cases} \tag{4.3b}$$

where s_i are binary state variables, each of which remains STICK until $|a_i| = \lambda_i g(v)/\kappa_i$ and remains SLIP until v goes through zero. Here, $\sum_{i=1}^{N} \lambda_i = 1$ and $\kappa_i, \sigma_i \in \mathbb{R}_+$ are the stiffness and micro-damping coefficients of the ith element, respectively. The state variable a_i of the ith element can be interpreted as the deflection of an asperity as is the case with the LuGre model. The positive constant parameter C, which replaces a quantity proportional to $|v|$ in the LuGre model (4.1a)(4.1b) determines how fast a_i converges to $\lambda_i g(v)/\kappa_i$.

The GMS model is capable of capturing many features of friction phenomena, such as presliding hysteresis with nonlocal memory, frictional lag, stick-slip oscillation, and non-drifting property [23, 35, 40]. One of its drawback is that the switching structure, involving additional binary variables s_i, results in the difficulty in on-line parameter identification, as pointed out in [36, 37]. Another point that should be noted is that, when $\sigma_i > 0$, the force f produced by (9) can be discontinuous with respect to time since (9b) does not guarantee the continuity of $\dot{a}$ with respect to time. Such a discontinuity, however, has not been seen as a problem. In fact, many previous works [87–90] employ a version of the GMS model without the term $\sigma_i \dot{a}_i$. In [36, 37], a smoothed version of the GMS model is proposed, but it involves another two functions and three parameters, which further increase the difficulty in parameter identification.

4.1.3 Differential-algebraic single-state friction model

In Chapter 3, the author proposed a single-state friction model based on a differential-algebraic inclusion (DAI). This model is only valid for the case where the magnitudes of maximum static friction force and kinetic friction force are equal to each other. It is derived

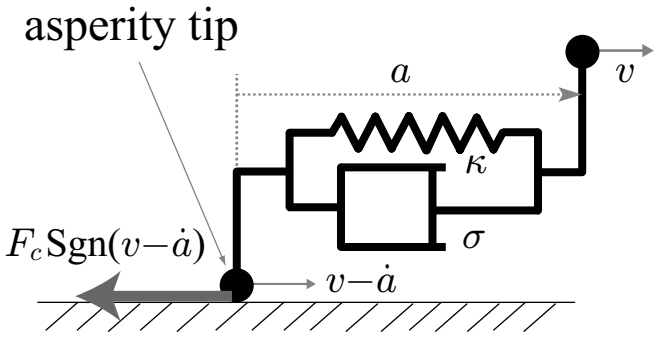

Figure 4.2: A physical interpretation of the model (4.4a) and (4.4b). The viscoelastic force balances the friction force $F_c\mathrm{Sgn}(v-\dot{a})$ both in the sliding and presliding regimes. Figure and caption are reprinted, with permission from Springer: Tribology letter, "A Multistate Friction Model Described by Continuous Differential Equations", vol. 51, no. 3, pp. 513–523, 2013, Xiaogang Xiong, Ryo Kikuuwe, and Motoji Yamamoto, Fig. 3 (see Appendix A1).

from the following DAI:

$$0 \in \kappa a + \sigma\dot{a} - F_c\mathrm{Sgn}(v-\dot{a}) \tag{4.4a}$$

$$f = \kappa a + \sigma\dot{a}. \tag{4.4b}$$

Here, the friction force acting on the averaged asperity is determined by a set-valued Coulomb friction law $F_c\mathrm{Sgn}(v-\dot{a})$ according to the velocity $v-\dot{a}$ of the asperity tip, of which the deflection is a, as shown in Fig. 4.2. Equation (4.4a) means that the force balances (i.e., is equal to) the force $\kappa a + \sigma\dot{a}$ produced by the viscoelasticity of the asperity.

It is clear that the DAI (4.4a)(4.4b) cannot be used for numerical computation of the friction force f because it involves set-valued function $\mathrm{Sgn}(\cdot)$. Our observation presented in [33] is that, by the use of Theorem 1, the DAI (4.4a)(4.4b) is equivalently rewritten as the following ordinary differential equation (ODE):

$$\dot{a} = \frac{\mathrm{sat}(F_c, \kappa a + \sigma v) - \kappa a}{\sigma} \tag{4.5a}$$

$$f = \mathrm{sat}(F_c, \kappa a + \sigma v). \tag{4.5b}$$

There are some friction models that have similar structures to (4.4a)(4.4b), which de-

scribe the Coulomb-like discontinuous relation between the force f and the asperity-tip velocity $v - \dot{a}$ [69, 91, 92]. They however need to be numerically integrated through through Euler methods. In contrast, because the model (4.4a)(4.4b) is equivalent to the ODE (4.5a)(4.5b), it can be numerically integrated through any integration methods such as Runge-Kutta methods.

In contrast to the Dahl and LuGre models, which are also described by ODEs, the model (4.5a)(4.5b) (or equivalently, (4.4a)(4.4b)) does not produce positional drift, as demonstrated in [33]. Obvious limitations of (4.5a)(4.5b) are that this model does not include the Stribeck effect and that it cannot produce presliding hysteresis with nonlocal memory. Those limitations will be treated in the next section.

4.2 New multistate friction model

4.2.1 Extension to include Stribeck effect

The previous friction model (4.4a)(4.4b), or equivalently, (4.5a)(4.5b), does not include the Stribeck effect represented by the function $g(v)$ in (4.2). One way to overcome this limitation is to replace F_c by $g(v)$, which represents rate-dependent friction force. Then, one can extend (4.4a)(4.4b) into the following DAI:

$$0 \in \kappa a + \sigma \dot{a} - g(v)\mathrm{Sgn}(v - \dot{a}) \tag{4.6a}$$

$$f = \kappa a + \sigma \dot{a}. \tag{4.6b}$$

As was the case with (4.4a)(4.4b), by the direct application of Theorem 1, (4.6) can also be equivalently rewritten into the following ODE:

$$\dot{a} = \frac{\mathrm{sat}(g(v), \kappa a + \sigma v) - \kappa a}{\sigma} \tag{4.7a}$$

$$f = \mathrm{sat}(g(v), \kappa a + \sigma v). \tag{4.7b}$$

Some differences and similarities among the model (4.7a)(4.7b), the LuGre model (4.1a)(4.1b), and the GMS model (4.3b)(4.3b) are now discussed. Because the model (4.7a)(4.7b) does

not consider the frictional lag, it is in the presliding regime when the friction force $\kappa a + \sigma v$ satisfies $|\kappa a + \sigma v| \leq g(v)$. In this case, $\mathrm{sat}(g(v), \kappa a + \sigma v)$ in (4.7a)(4.7b) reduces to $\kappa a + \sigma v$ and thus (4.7a)(4.7b) reduces to the following equation:

$$\dot{a} = v \tag{4.8a}$$

$$f = \kappa a + \sigma v. \tag{4.8b}$$

One can observe that (4.8) is equivalent to the GMS model (4.3b)(4.3b) in the presliding regime with $N = 1$.

In the sliding regime, the steady-state friction force (i.e., the force f when v is constant and $\dot{a} = 0$) can be obtained by substituting $\dot{a} = 0$ into (4.1a)(4.1b) (4.3b)(4.3b), and (4.7a)(4.7b). In the case of LuGre model (4.1a)(4.1b) and GMS models (4.3b)(4.3b), one can easily see that $f = \mathrm{sgn}(v)g(v)$ is satisfied in the steady state because both (4.1b) and (4.3b) imply that $\dot{a} = 0$ results in $\kappa a = \mathrm{sgn}(v)g(v)$ [1]. In the case of the model (4.7a)(4.7b),

$$|\kappa a + \sigma v| > g(v) \tag{4.9a}$$

$$f = \mathrm{sgn}(\kappa a + \sigma v)g(v) = \kappa a \tag{4.9b}$$

are satisfied in the steady state in the sliding regime. Eliminating $g(v)$ yields $|\kappa a + \sigma v| > |\kappa a|$, which leads to $\mathrm{sgn}(a) = \mathrm{sgn}(v) = \mathrm{sgn}(\kappa a + \sigma v)$. Therefore, one can see that the model (4.7a)(4.7b) also results in $f = \mathrm{sgn}(v)g(v)$ in the steady state.

The state variable a and its derivative $\dot{a}$ are both necessary to realize such a pair of interchangeable expressions; the DAI (4.6a)(4.6b) and the ODE (4.7a)(4.7b). From a physical point of view, a can be understood as the deflection of a linearly viscoelastic asperity.

4.2.2 Extension to include presliding hysteresis with nonlocal memory

The modified model (4.7a)(4.7b) represents a single viscoelasto-plastic element with rate-dependent friction force, which is unable to produce hysteresis with nonlocal memory. As has been suggested in the literature [34, 35, 43–45], one imaginable way to overcome this

[1] Here we are using $N = 1$ and $\lambda_1 = 1$ in (4.3b)(4.3b) for the simplicity of comparison.

limitation is to extend (4.6a)(4.6b) (or equivalently, (4.7a)(4.7b)) to a multistate model composed of many viscoelasto-plastic elements. Based on this idea, (4.6a)(4.6b) can be extended as follows:

$$0 \in \kappa_i a_i + \sigma_i \dot{a}_i - \lambda_i g(v)\mathrm{Sgn}(v - \dot{a}_i),\ i \in \{1, \cdots, N\} \tag{4.10a}$$

$$f = \sum_{i=1}^{N} (\kappa_i a_i + \sigma \dot{a}_i). \tag{4.10b}$$

A physical interpretation of the multistate DAI (4.10a)(4.10b) can be illustrated as Fig. 4.3, which can be thought of as a straightforward extension of Fig. 4.2.

As was the case between (4.6a)(4.6b) and (4.7a)(4.7b), (4.10a) and (4.10b) are equivalent to the following ODE:

$$\dot{a}_i = \frac{\mathrm{sat}(\lambda_i g(v), \kappa_i a_i + \sigma_i v) - \kappa_i a_i}{\sigma_i},\ i \in \{1, \cdots, N\} \tag{4.11a}$$

$$f = \sum_{i=1}^{N} \mathrm{sat}(\lambda_i g(v), \kappa_i a_i + \sigma_i v). \tag{4.11b}$$

This model produces presliding hysteresis with nonlocal memory.

4.2.3 Extension to include frictional lag

The multistate model (4.11a)(4.11b) does not capture frictional lag [25]. As has been suggested in [12], the lag effect can be included by using an additional state variable as follows:

$$\dot{\gamma} = (g(v) - \gamma)/\tau_d \tag{4.12a}$$

$$0 \in \kappa_i a_i + \sigma_i \dot{a}_i - \lambda_i \gamma \mathrm{Sgn}(v - \dot{a}_i),\ i \in \{1, \cdots, N\} \tag{4.12b}$$

$$f = \sum_{i=1}^{N} (\kappa_i a_i + \sigma \dot{a}_i), \tag{4.12c}$$

or equivalently,

$$\dot{\gamma} = (g(v) - \gamma)/\tau_d \tag{4.13a}$$

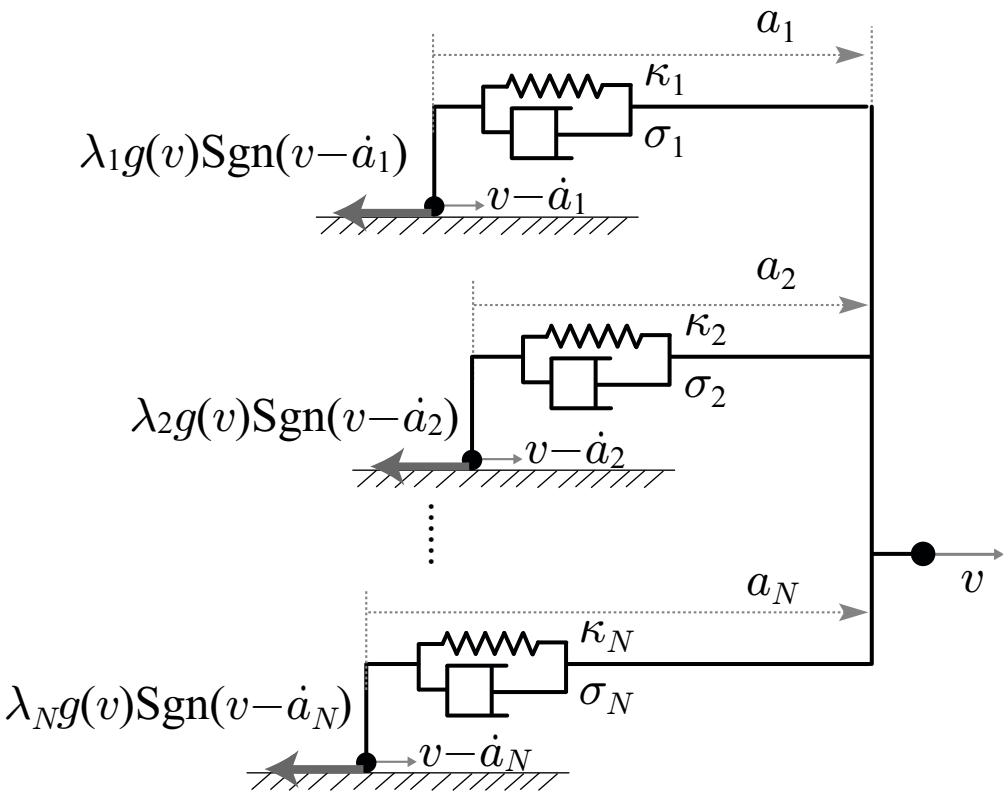

Figure 4.3: A physical interpretation of the model (4.10a) and (4.10b). Figure and caption are reprinted, with permission from Springer: Tribology letter, "A Multistate Friction Model Described by Continuous Differential Equations", vol. 51, no. 3, pp. 513–523, 2013, Xiaogang Xiong, Ryo Kikuuwe, and Motoji Yamamoto, Fig. 4 (see Appendix A1).

$$\dot{a}_i = \frac{\mathrm{sat}(\lambda_i \gamma, \kappa_i a_i + \sigma_i v) - \kappa_i a_i}{\sigma_i},\ i \in \{1, \cdots, N\} \tag{4.13b}$$

$$f = \sum_{i=1}^{N} \mathrm{sat}(\lambda_i \gamma, \kappa_i a_i + \sigma_i v). \tag{4.13c}$$

Here, $\gamma \in \mathbb{R}$ is a new state variable representing a lagged value of $g(v)$. Its initial value should be set within the range $F_c \leq \gamma(0) \leq F_s$. The new parameter $\tau_d > 0$ in (4.12a) represents the time constant of convergence of γ to $g(v)$. When τ_d approaches zero, the model (4.12a)(4.12b)(4.12c) becomes close to (4.10a)(4.10b).

The proposed model (4.12a)(4.12b) (4.12c) is physically straightforward, only describ-

ing the balance between the linear viscoelastic force $\kappa a + \sigma \dot{a}$ and the friction force $\gamma \mathrm{Sgn}(v - \dot{a})$, which depends on the first-order lagged value γ of $g(v)$. It however has not been found in the literature. One difficulty may have been that it is numerically intractable due to the inclusion of the discontinuous $\mathrm{Sgn}(\cdot)$ function. The difficulty is now removed by the use of Theorem 1, which implies that the DAI (4.12a)(4.12b)(4.12c) is equivalent to the ODE (4.13a)(4.13b)(4.13c) having no numerical difficulty.

4.3 Theoretical analysis

This section shows that the proposed model (4.13a)(4.13b)(4.13c) has the following properties, which should be possessed by a well-behaved friction model [35]:

1. The non-viscous part of the friction force is bounded.
2. The friction force is continuous with respect to time.
3. The friction model is dissipative.

To prove the first property of the proposed model (4.13a)(4.13b)(4.13c), a nonnegative function is defined as $V_1 \triangleq \gamma^2/2$. The time derivative of this function is as follows:

$$\dot{V}_1 = \gamma \dot{\gamma} = \gamma(g(v) - \gamma)/\tau_d, \tag{4.14}$$

which is negative when $|\gamma| \geq F_s$ due to $F_c \leq g(v) \leq F_s$. Therefore, one can obtain that $|\gamma| \leq F_s$ is always satisfied if the initial value of γ satisfies $|\gamma| \leq F_s$ [21, 31]. From (4.13c), one can see that $|f| \leq \sum_{i=1}^{N} \lambda_i |\gamma| \leq F_s \sum_{i=1}^{N} \lambda_i = F_s$. This means that $|f|$ is bounded.

The second property of the proposed model (4.13a)(4.13b) (4.13c) is obvious since the function sat is continuous with respect to its arguments and the variables γ, a, and v are continuous with respect to time.

The third property can be proven by showing that there exists a constant $\varphi > 0$ such that $\int_0^t v f \mathrm{d}t \geq -\varphi$ is satisfied for all $t > 0$ [21, 31]. Let us define a function V_2 as $V_2 \triangleq$

$\sum_{i=1}^{N} \kappa_i a_i^2/2$. Then, one obtains

$$vf - \dot{V}_2 = \sum_{i=1}^{N} \frac{(\sigma_i v - \kappa_i a_i)\mathrm{sat}(\lambda_i \gamma, \kappa_i a_i + \sigma_i v) + \kappa_i^2 a_i^2}{\sigma_i}. \tag{4.15}$$

When $z = 0$, the right hand side of (4.15) is positive. When $z \neq 0$, (4.15) reduces to the following equation:

$$vf - \dot{V}_2 = \sum_{i=1}^{N} \frac{\sigma_i^2 v^2 + \kappa_i^2 a_i^2 (\max(1, |\kappa_i a_i + \sigma_i v|/(\lambda_i \gamma)) - 1)}{\sigma_i \max(1, |\kappa_i a_i + \sigma_i v|/(\lambda_i \gamma))} \geq 0. \tag{4.16}$$

Therefore, one can see that $vf - \dot{V}_2 \geq 0$ is always satisfied, and thus

$$\int_0^t vf \mathrm{d}t \geq V_2(t) - V_2(0) > -V_2(0) \tag{4.17}$$

is also satisfied for all $t > 0$. This shows that the model (4.13a)(4.13b)(4.13c) has the third property.

4.4 Simulation and comparison

This section illustrates the properties of the new model through simulations. Section 4.4.1, 4.4.2, and 4.4.3 provide the simulation results of the new model (4.13a)(4.13b)(4.13c). Section 4.4.4 gives comparison between the GMS model and the new model. In all simulations, the parameters of the models were chosen through trial-and-error so that they produce major features of friction phenomena. It must be noted that an efficient parameter tuning method remains an open problem. The forward Euler method was used for all simulations.

4.4.1 Nondrifting and stick-slip oscillation

It is well known that an external force that is smaller than the magnitude of static friction force does not produce unbounded positional drift, which is termed as nondrifting property [21, 22]. A simulation was performed to test this nondrifting property of the new model (4.13a)(4.13b)(4.13c). In this simulation, an external force shown in Fig. 4.4(a) was applied

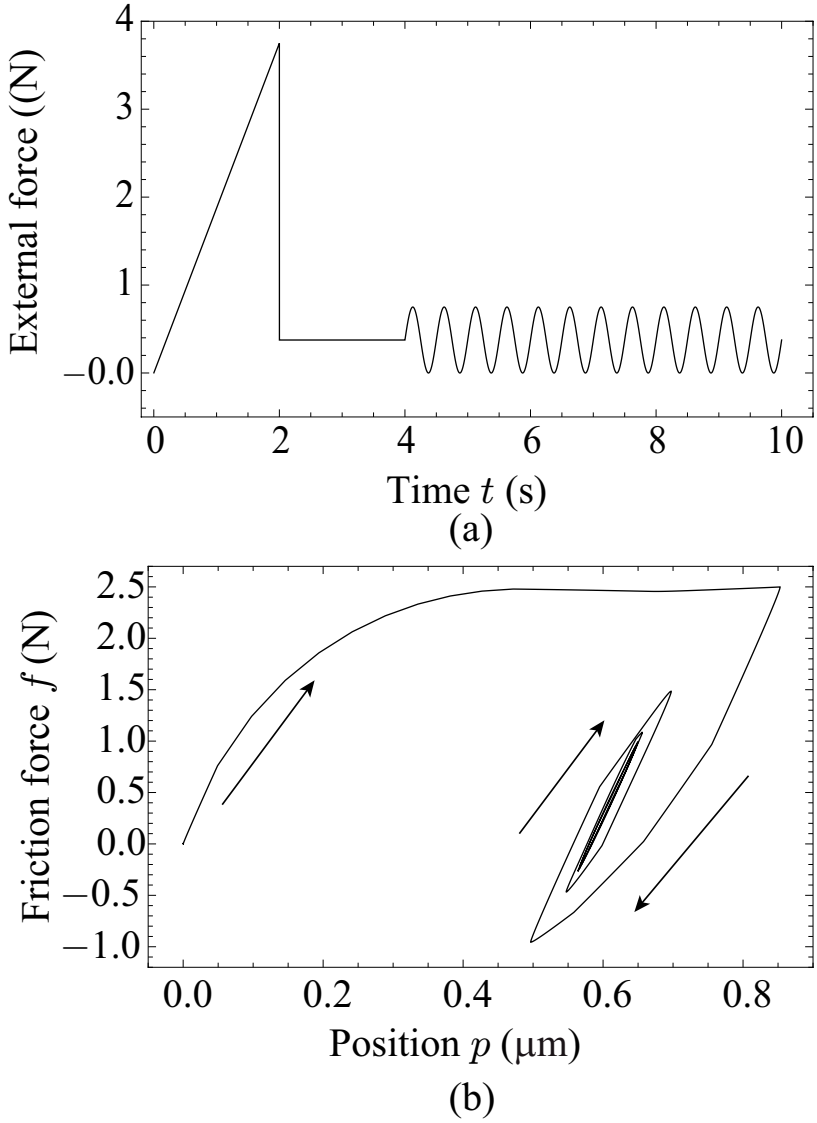

Figure 4.4: Nondrifting property; (a) an external force as a function of time t; (b) the friction force f as a function of position p. The parameters are chosen as; $\alpha = 2$, $v_s = 5$ μm/s, $F_c = 1$ N, $F_s = 2.5$ N, $\kappa_i = (5/i)$ N/μm, $\sigma_i = 0.02$ Ns/μm, $\lambda_i = 0.1$, $i \in \{1, 2, \cdots, 10\}$, $\tau_d = 0.02$ s. The time-step size was 0.001 s. Figure and caption are reprinted, with permission from Springer: Tribology letter, "A Multistate Friction Model Described by Continuous Differential Equations", vol. 51, no. 3, pp. 513–523, 2013, Xiaogang Xiong, Ryo Kikuuwe, and Motoji Yamamoto, Fig. 4 (see Appendix A1).

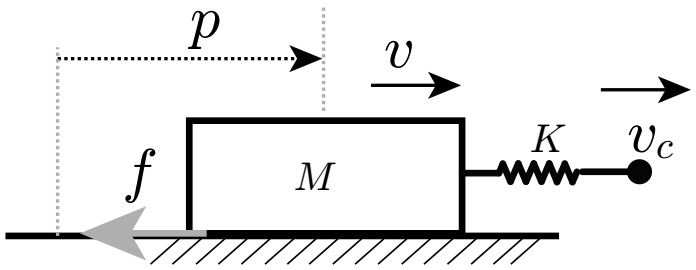

Figure 4.5: The scenario of stick-slip oscillation

to a mass $M = 1$ kg, which is subjected to friction force f produced by the new model (4.13a)(4.13b)(4.13c). Fig. 4.4(b) shows the result, in which the position oscillates without shift, exhibiting the nondrifting property of the new model.

Another set of simulation was performed to check the stick-slip behavior of the new model. In this simulation, as shown in Fig. 4.5, the mass $M = 1$ kg, subjected to the friction force f, was connected to a spring with the stiffness $K = 0.1$ N/μm, and the other end of the spring was moved at a constant velocity $v_c = 2$ μm/s. Fig. 4.6 shows the results, in which one can observe that the mass M experienced a stick-slip motion. Fig. 4.6(a) shows step-like changes in the position and impulsive changes in the velocity. The dashed circles in Fig. 4.6(b) indicate spike-like force followed by high frequency oscillation after stick-slip periods. Those phenomena are consistent with the empirical results [22]. They are known to be reproducible with the GMS model (4.3b)(4.3b) and the generic models in [38, 39], while, as pointed out in [35], the LuGre model [21, 31], the single state elastoplastic model [32], and the Leuven model [24, 34] produce qualitatively different stick-slip motion.

4.4.2 Rate independency and amplitude dependency of hysteresis loop

Experimental data in the literature, e.g., [22, 39, 93], show that, in the presliding regime, the hysteresis loop of a force-position curve is hardly affected by the change rate of position. This characteristic is referred to as rate independency of hysteresis loop. In contrast, different strokes of position input result in different loop sizes of force-position curves [22, 39]. Here we refer to such a characteristic as an amplitude dependency of hystere-

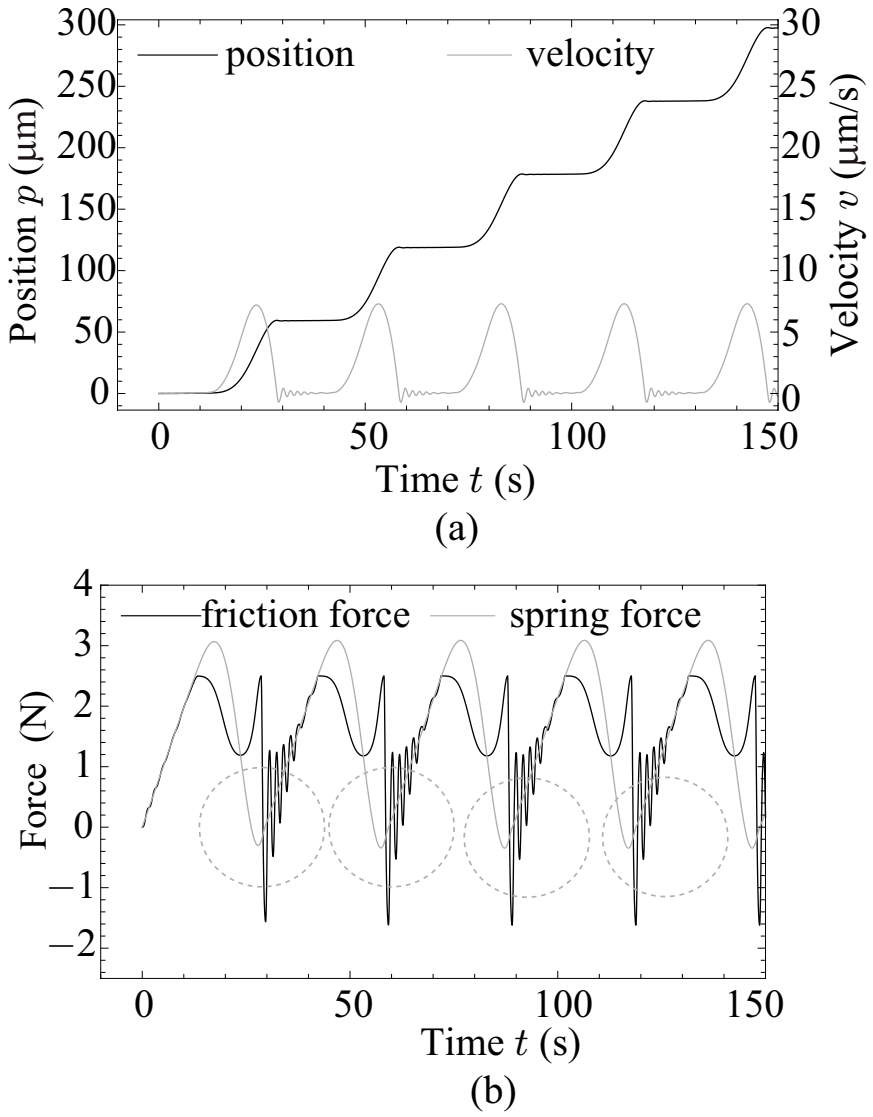

Figure 4.6: Stick-slip oscillation; (a) the position and velocity of the mass M as a function of time t; (b) the spring force and friction force as a function of time t. The parameters were chosen identical to those in Fig. 4.4. The time-step size was 0.005 s. Figure and caption are reprinted, with permission from Springer: Tribology letter, "A Multistate Friction Model Described by Continuous Differential Equations", vol. 51, no. 3, pp. 513–523, 2013, Xiaogang Xiong, Ryo Kikuuwe, and Motoji Yamamoto, Fig. 5 (see Appendix A1).

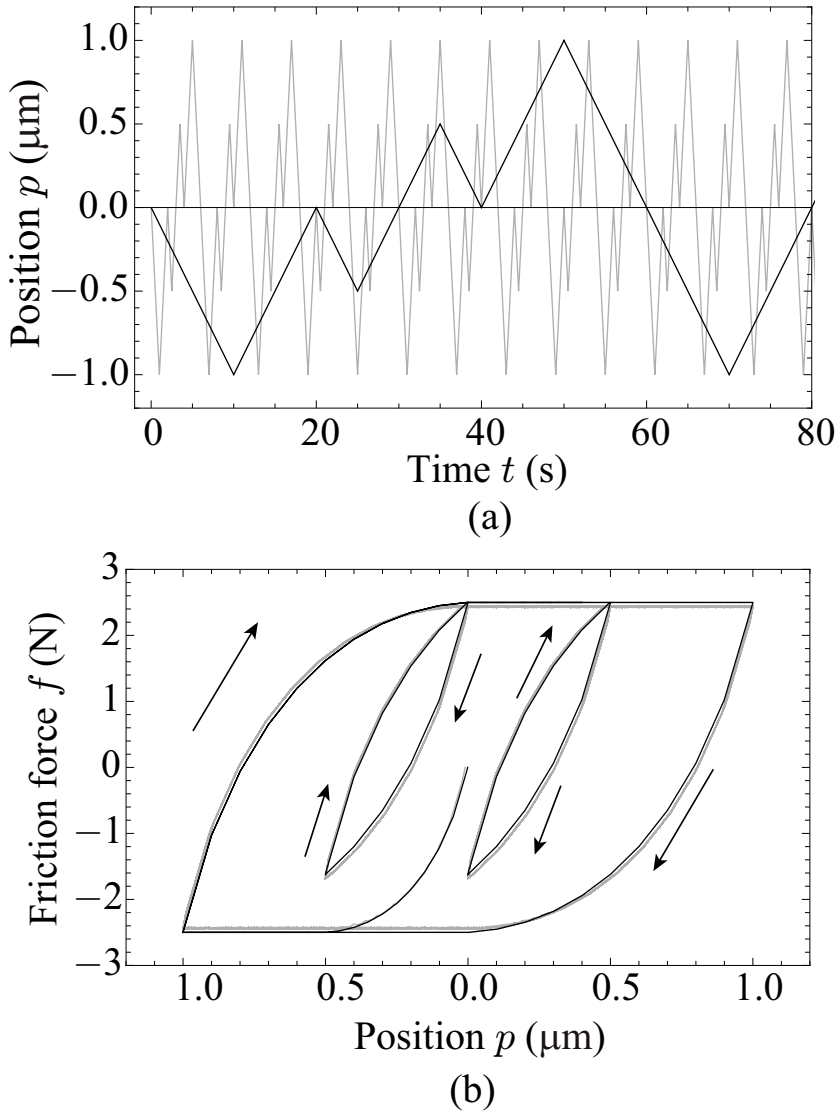

Figure 4.7: Rate independency of hysteresis loop; (a) two positional inputs p as functions of time t (The gray curve is of 10 times the frequency of the black curve.); (b) the friction force f obtained for the two different input position signals p. The parameters were chosen identical to those in Fig. 4.4. The time-step size was 0.01 s. Figure and caption are reprinted, with permission from Springer: Tribology letter, "A Multistate Friction Model Described by Continuous Differential Equations", vol. 51, no. 3, pp. 513–523, 2013, Xiaogang Xiong, Ryo Kikuuwe, and Motoji Yamamoto, Fig. 6 (see Appendix A1).

sis loop. Two simulations were performed to test these two properties of the new model (4.13a)(4.13b)(4.13c).

In the simulation of rate independency of hysteresis loop, the positional inputs shown in Fig. 4.7 (a) were provided to the new model and the resultant friction forces f were recorded. The position inputs in Fig. 4.7(a) were chosen so that the presliding hysteresis with nonlocal memory becomes visible. The gray curve in Fig. 4.7(a) is 10 times the frequency of the black one. The result is shown in Fig. 4.7(b), which clearly shows that the model (4.13a)(4.13b)(4.13c) is rate independent in the shape of the hysteresis loop. It also shows that the force-position curves have closed internal loops whose top tips overlap the trajectory of outer loop, implying that the new model captures the feature of presliding hysteresis with nonlocal memory.

In the simulation of amplitude dependency of hysteresis loop, the positional inputs in Fig. 4.8(a) were provided to the new model (4.13a)(4.13b)(4.13c), and the resultant forces were plotted as a function of the positional inputs, as shown in Fig. 4.8(b). It is shown that the sizes of the loops in the force-position hysteresis vary depending on different magnitudes of input. This characteristic is consistent with the experimental results in [22, 39] and the simulation results of the generic model presented in [39].

4.4.3 Frictional lag

It has been known that frictional lag results in hysteresis in the force-velocity curve, in which the friction force during acceleration is larger than that during deceleration [23, 40]. A simulation was performed to check this property of the new model (4.13a)(4.13b)(4.13c). In this simulation, two biased sinusoidal velocity inputs in Fig. 4.9(a) were provided to the new model (4.13a)(4.13b)(4.13c). Fig. 4.9(b) shows the corresponding results, in which the magnitude of friction force is larger during acceleration than during deceleration. Fig. 4.9(b) also shows that the hysteresis loops of the force-velocity curves are influenced both by the input frequencies and τ_d. The frequency effect on the hysteresis loops has been observed in Hess and Soom's experiments [94] and pointed out in Al-Bender et al.'s [35] and De Moerlooze et al.'s modeling studies [39].

Another simulation was performed to investigate the effect of frictional lag on the new

model's behavior during transitions between the presliding and sliding regimes. In this simulation, two sinusoidal velocity inputs in Fig. 4.10(a) were provided to the new model (4.13a)(4.13b)(4.13c). Fig. 4.10(b) shows the results. One can observe that the width of the force-velocity loop increases as the input frequency increases. This feature is consistent with experimental results in the literature [35, 40]. Fig. 4.10(b) also shows that, by appropriate choice of τ_d, the new model can be adjusted so that the friction force during acceleration is bigger than that in deceleration. This feature of the curves is reported in the experimental results in the literature [22, 23, 40].

4.4.4 Comparison between GMS model and new model

The GMS model (4.3b)(4.3b) and the new model (4.13a)(4.13b)(4.13c)were compared through a simulation of their transition behaviors. In this simulation, a sinusoidal velocity input shown in Fig. 4.11(a) was provided to the two models. The parameters of the new model were identical to those in Fig. 4.4. except three different values of σ_i ($i = 1, \cdots, 10$) were used in this simulation. The parameters of GMS model were also identical to those of the new model except that the parameter C was chosen as $C = 62$ N/s. This C value was chosen so that the resultant force-velocity curve becomes as close as possible to that of the new model with $\sigma_i = 0.001$ Ns/μm, which are shown in Fig. 4.11(b).

The results are shown in Fig. 4.11(b) to (h). Fig. 4.11(b), (c), and (d) show that the force produced by the GMS model is in some places nonsmooth, and this feature is magnified as σ_i increases. Fig. 4.11(e) and (f) show that the discontinuities in the force coincide with transitions between the presliding and sliding regimes of the elements. It is reasonable to consider that this is caused by the equation (4.3b), which shows that $\dot{a}_i$ is not guaranteed to be continuous with respect to v and a_i. The magnified discontinuities with larger σ_i are also reasonable results because (4.3b) implies that the discontinuities in $\dot{a}_i$ is propagated to f through the coefficient σ_i. This sort of results have not been reported in previous result, presumably because this effect is not apparent with sufficiently small σ_i values. Actually, most of previous works [36, 37, 87–89] employing the GMS models ignore the term $\sigma_i a_i$ and thus the discontinuities have not been a concern. As for the proposed model, in contrast, $\sigma_i > 0$ is necessary because (4.13a)(4.13b)(4.13c) includes the division by σ_i. Therefore,

one can say that the σ_i values should be sufficiently low in the GMS model but should be sufficiently high in the proposed model.

As an effect of the continuous ODE (4.13a)(4.13b)(4.13c), the friction force produced by the new model is always continuous with respect to the velocity and the time, as can be seen in Fig. 4.11(b)(c)(d) and Fig. 4.11(g)(h), although some non-smoothness (discontinuous changes in the rate-of-change of the force) can be observed in Fig. 4.11(g)(h). Another feature of the new model can be seen in Fig. 4.11(g) and (h), in which the transition from the sliding regime to the presliding regime occur at one element after another. This is in contrast to the simultaneous transitions exhibited by the GMS model, shown in Fig. 4.11(e) and (f).

4.5 Summary

The chapter has introduced a new multistate friction model that is an extended version of the author' differential-algebraic single-state friction model. This multistate friction model consists of multiple parallel elements. Each element is described by a single-state friction model, which exhibits smooth transitions between the presliding and sliding regimes. Moreover, the new model involves a parameter τ_d to adjust the effect of frictional lag, which is the time lag from the change in the velocity to the change in the friction force. This model is described as a set of continuous ODEs, and thus the friction force produced by this model is always continuous with respect to time and the input velocity. It does capture many major features of friction reported in the literature, such as the Stribeck effect, nondrifting property, stick-slip oscillation, presliding hysteresis with nonlocal memory, rate independency and magnitude dependency of hysteresis loop, and frictional lag. This model has been validated through simulations and comparisons with experimental results in the literature.

Potential applications of this model include not only simulation but also control for friction compensation, because this model, i.e., the ODE (4.13a)(4.13b)(4.13c), is computationally inexpensive enough for realtime computation and does not require any iterative computation. Future work should clarify a method to identify the parameters of the proposed model. It may be possible to apply some on-line parameter identification methods

in the literature, e.g., [36, 37, 87], since this model is described by a set of continuous differential equations (4.13a)(4.13b)(4.13c). Effects of each parameters on major features of friction should also be clarified for efficient off-line tuning based on experimental data.

As another important topic of study, the proposed model should be experimentally compared to previous friction models, such as the GMS model. One suitable approach may be, as can be found in [95, 96], to optimize the parameters of each model to fit experimental data from real friction phenomena, and to compare residual fitting errors obtained from the models. Relating such results to the complexity of the models, such as the number of parameters, memory usage, and the computational cost, may lead to a set of guidelines for choosing a friction model. One salient feature of the proposed model is that the micro-damping coefficient requires to be non-zero and can be rather high without affecting the continuity, while it is usually considered zero in previous work. Practical advantages or disadvantages of this feature may also be clarified by comparative study based on parameter fitting.

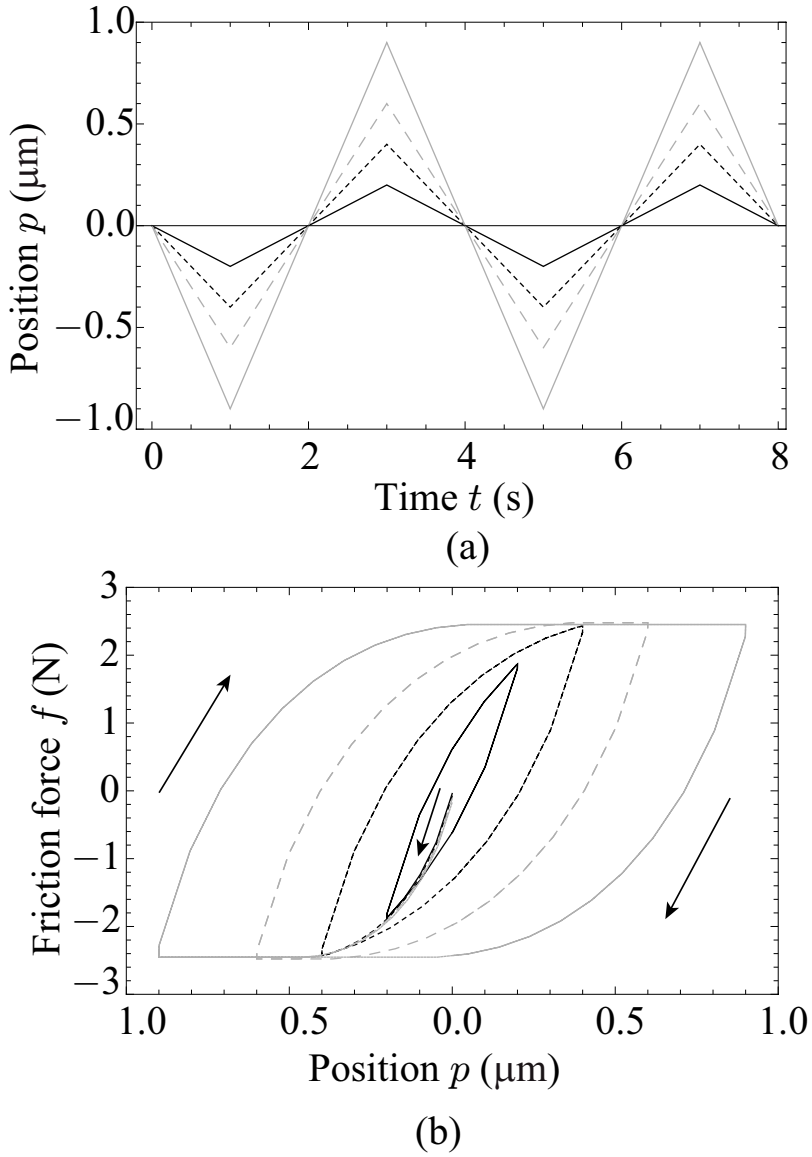

Figure 4.8: Amplitude dependency of hysteresis loop; (a) four positional inputs p with different amplitudes as functions of time t; (b) the friction forces f obtained for the four different input position signals p. The parameters were chosen identical to those in Fig. 4.4. The time-step size was 0.001 s. Figure and caption are reprinted, with permission from Springer: Tribology letter, "A Multistate Friction Model Described by Continuous Differential Equations", vol. 51, no. 3, pp. 513–523, 2013, Xiaogang Xiong, Ryo Kikuuwe, and Motoji Yamamoto, Fig. 7 (see Appendix A1).

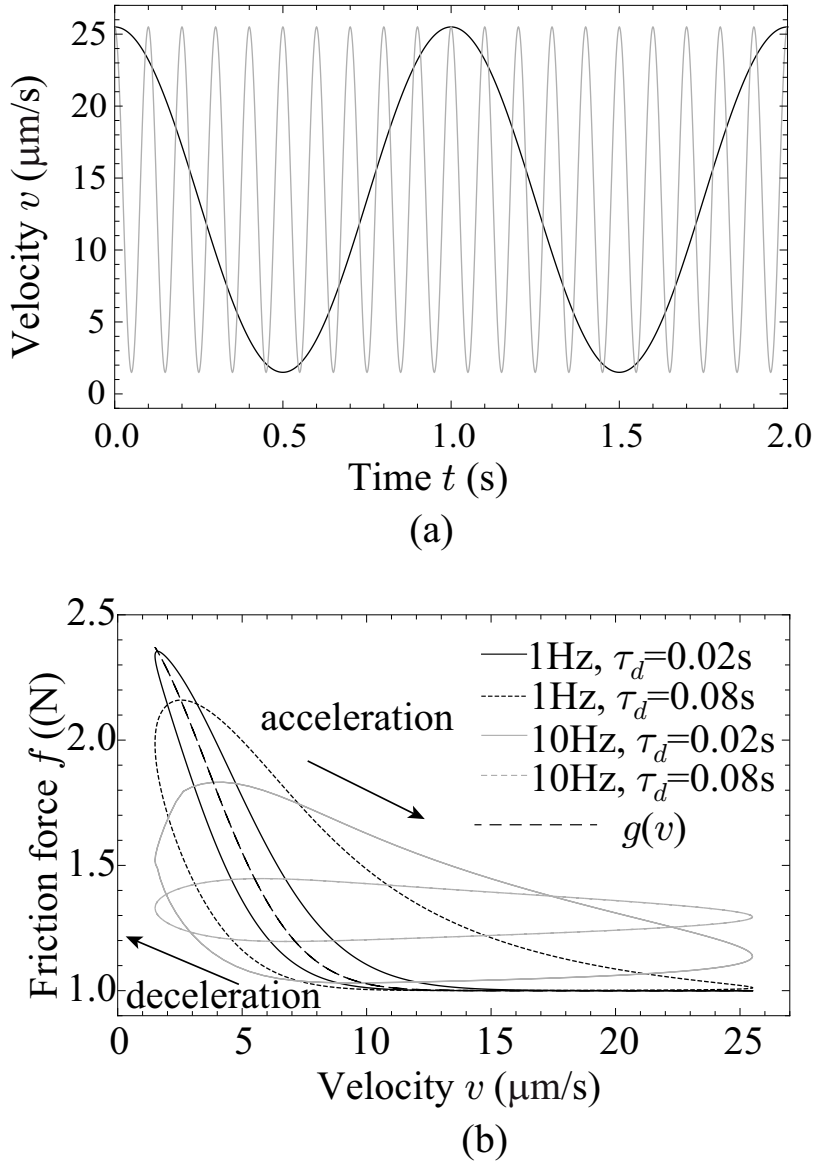

Figure 4.9: Frictional lag; (a) two velocity inputs v as functions of time t; (b) the friction force f obtained for the two different input velocity signals v and two values of τ_d. The other parameters were chosen identical to those in Fig. 4.4. The time-step size was 0.001 s. Figure and caption are reprinted, with permission from Springer: Tribology letter, "A Multistate Friction Model Described by Continuous Differential Equations", vol. 51, no. 3, pp. 513–523, 2013, Xiaogang Xiong, Ryo Kikuuwe, and Motoji Yamamoto, Fig. 8 (see Appendix A1).

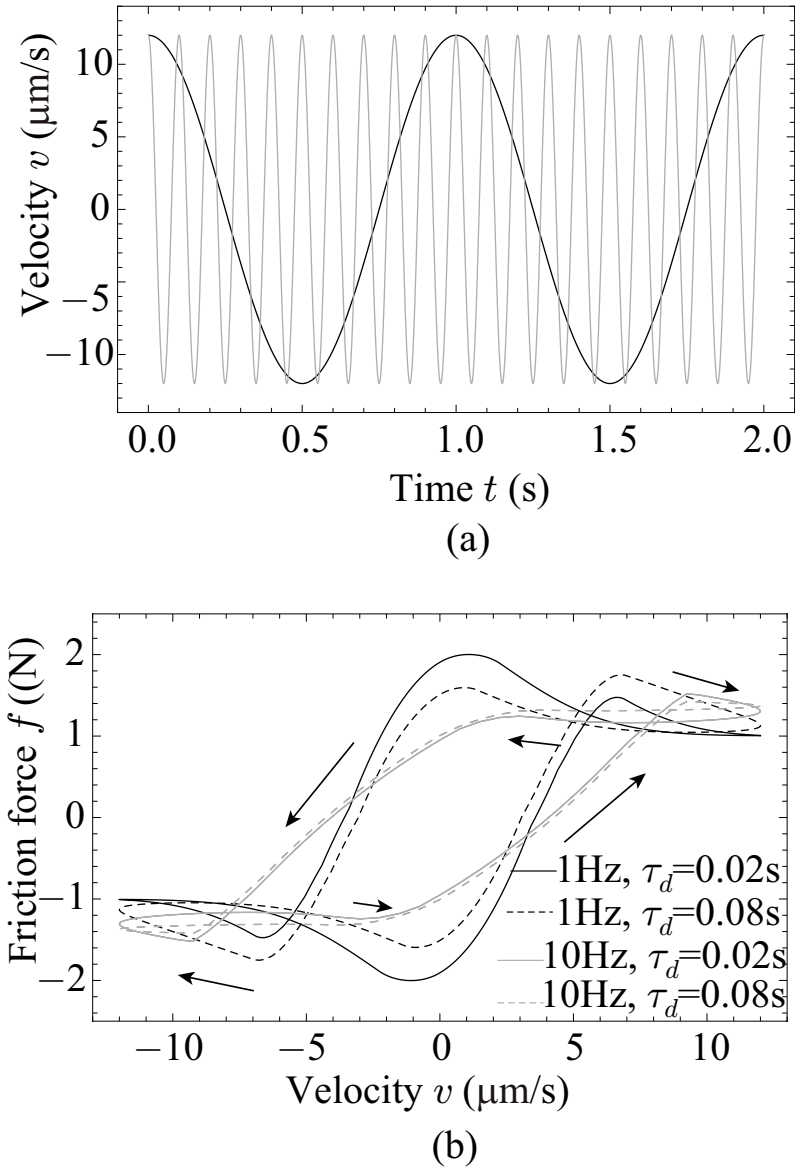

Figure 4.10: Frictional lag effect on transition behavior; (a) two velocity input v as functions of time t; (b) the friction force f obtained for the two different input velocity signals v and two values of τ_d. The other parameters were chosen identical to those in Fig. 4.4. The time-step was 0.001 s. Figure and caption are reprinted, with permission from Springer: Tribology letter, "A Multistate Friction Model Described by Continuous Differential Equations", vol. 51, no. 3, pp. 513–523, 2013, Xiaogang Xiong, Ryo Kikuuwe, and Motoji Yamamoto, Fig. 9 (see Appendix A1).

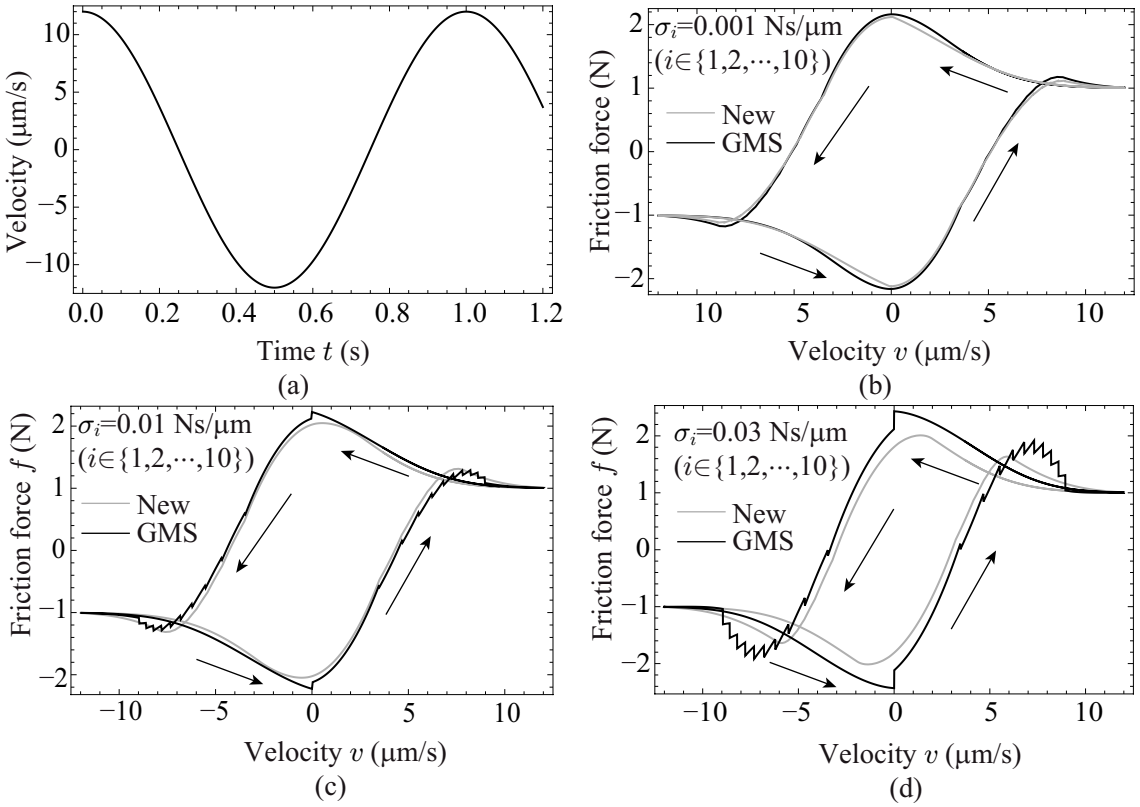

Figure 4.11: Transition behaviors of the GMS model (4.3b)(4.3b) and new model (4.13a) (4.13b) (4.13c); (a) a velocity input v as a functions of time t; (b)(c)(d) the friction force f obtained from the input velocity v; (e)(f)(g)(h) the friction force f and the number of elements in the presliding regimes; The gray vertical lines in (e)(f)(g)(h) indicate the time at which the number of elements in the presliding regime changes. The parameters were chosen identical to those in Fig. 4.4. The time-step size was 0.0001 s. (It should be noted that non-zero σ_i has not been used in reported applications of the GMS model in the literature.) Figure and caption are reprinted, with permission from Springer: Tribology letter, "A Multistate Friction Model Described by Continuous Differential Equations", vol. 51, no. 3, pp. 513–523, 2013, Xiaogang Xiong, Ryo Kikuuwe, and Motoji Yamamoto, Fig. 10 (see Appendix A1).

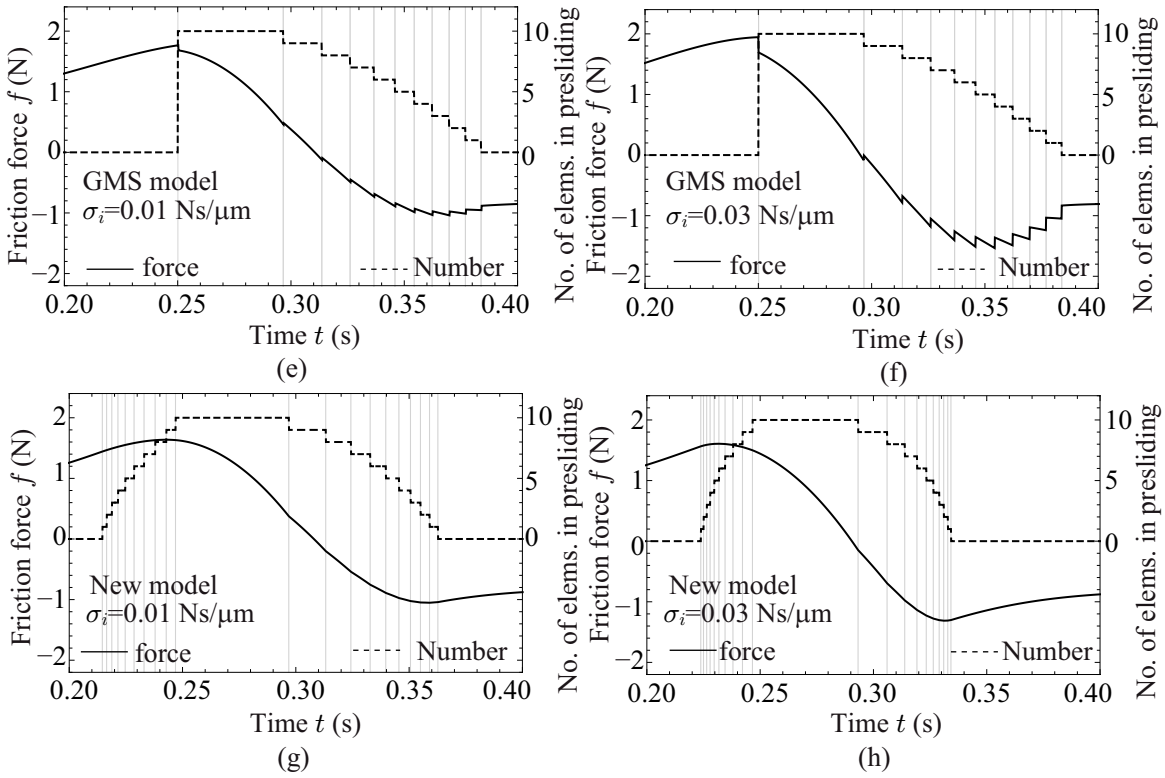

Figure 4.11: (Continued.) Figure and caption are reprinted, with permission from Springer: Tribology letter, "A Multistate Friction Model Described by Continuous Differential Equations", vol. 51, no. 3, pp. 513–523, 2013, Xiaogang Xiong, Ryo Kikuuwe, and Motoji Yamamoto, Fig. 10 (see Appendix A1).

Chapter 5

A contact model with nonlinear compliance

This chapter proposes a compliant contact model with nonzero indentation based on the previous simple contact model in Chapter 3. The contact force and indentation of this model possesses the following three features: (i) continuity of the force at the time of collision, (ii) Hertz-like nonlinear force-indentation curve, and (iii) non-zero indentation at the time of loss of contact force. On the contrary, the conventional Hunt-Crossley (HC) model does not capture the feature (iii) as the model makes the contact force and the indentation reach zero simultaneously. The comparisons between the HC model and the new model are illustrated through their force-indentation curves and an example of a free-falling ball. The behaviors of the new model and the effect of parameters in the model are investigated through numerical simulations.

The rest of this chapter is organized as follow. Section 5.1 introduces some mathematical preliminaries to be used in the subsequent sections. Next, some related work is outlined in Section 5.1. Section 5.2 introduces the new compliant contact model and Section 5.3 presents some numerical results concerning the effects of parameters in the new model. Finally, Section 5.4 provides concluding remarks.

★ Portions of the materials in this chapter are reprinted from *Transactions of ASME: Journal of Applied Mechanics*, vol. 81, no. 2, Xiaogang Xiong and Ryo Kikuuwe and Motoji Yamamoto, "A Contact Force Model With Nonlinear Compliance and Residual Indentation", pp. 021003-1:8, 2014, as published in [97, 98], with permission from ASME (see Appendix A2).

5.1 Related work

In some previous work, the force-indentation curves are obtained through experiments using real objects such as biological tissues [2, 3] and sports balls [4, 15]. One typical curve is roughly depicted as Fig. 5.1(a), by referring to the experimental data of biological tissue contact in [2]. It shares three distinct characteristics that has been elucidated in the beginning of this chapter with other experimental results of real objects contact [4, 15, 60].

Kelvin-Voigt (KV) model is known to be one of the simplest models of contact. In this model, the contact force $f \in \mathbb{R}$ can be described in the following form:

$$f = \begin{cases} 0 & \text{if } p < 0 \\ -K(p + b_1\dot{p}) & \text{if } p \geq 0 \end{cases} \tag{5.1}$$

where $p \in \mathbb{R}$ is the displacement, of which the positive value stands for the depth of indentation, $K > 0$ is the stiffness coefficient, and $b_1 \geq 0$ is the ratio of the viscous coefficient to the stiffness coefficient. This model is preferred in many applications due to its simplicity, but it produces unnatural discontinuous and sticky force as illustrated in Fig. 5.1(b) and pointed out in [16, 53]. In addition, the linear force-indentation relation does not agree with Hertz's model. The COR corresponding to this model is independent from impact velocity [51, 53].

Hunt-Crossley (HC) model overcomes the drawbacks of KV model (5.1) and is consistent with Hertz's model. HC model can be described as follows:

$$f = \begin{cases} 0 & \text{if } p < 0 \\ -Kp^{\lambda}(1 + b_2\dot{p}) & \text{if } p \geq 0, \end{cases} \tag{5.2}$$

where $b_2 \geq 0$ is a damping parameter and $\lambda > 1$ is a constant related to materials and geometries of contact objects. This model results in a force-indentation curve as illustrated in Fig. 5.1(c) and has been utilized to reproduce the behaviors of measurably-deformable objects [2, 3, 58–60]. However, as can be seen from the difference between Fig. 5.1(a) and Fig. 5.1(c), HC model produces a distinctly different curve from empirical results, producing

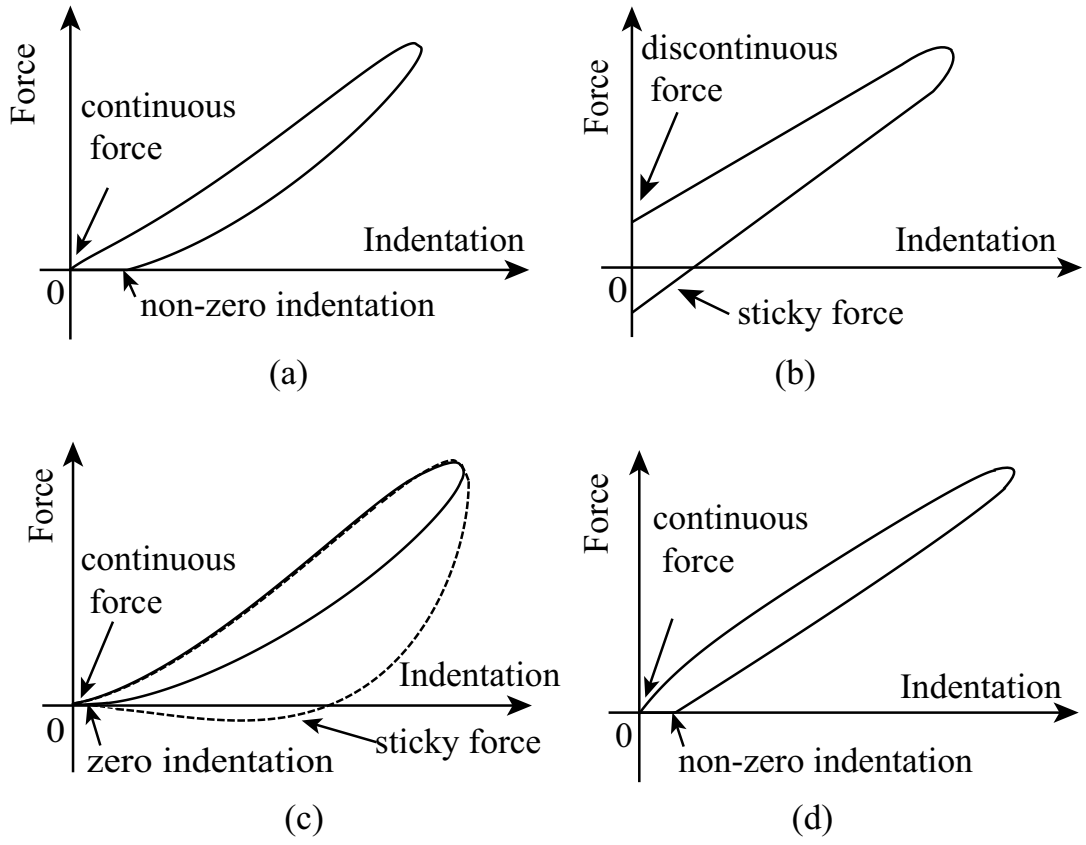

Figure 5.1: Force-indentation curves; (a) typical empirical result adopted from, e.g., [2, Fig. 4], [3, Fig. 2.6] and [4, Fig. 2], (b) KV model (5.1), (c) HC model (5.2) without any external force (solid) and with an external pulling force (dashed), (d) the author's previous contact model (5.3). Figure and caption are reprinted, with permission from ASME: Journal of Applied Mechanics, "A Multistate Friction Model Described by Continuous Differential Equations", vol. 81, no. 2, pp. 021003-1:8, 2014, Xiaogang Xiong, Ryo Kikuuwe, and Motoji Yamamoto, Fig. 2 (see Appendix A2).

zero indentation at the time of zero contact force. It is consistent with empirical data only when the COR is large [61]. Another weakness of HC model is that, as pointed out in [55], an unnatural sticky force may arise when the objects are separated by an external force, as indicated by the dashed curve in Fig. 5.1(c).

In Chapter 3, the author proposed a linear contact model defined by the following differential algebraic inclusion (DAI):

$$0 \in a + \left(\frac{1}{\gamma} + \beta_1\right)\dot{a} - \mathrm{dio}(\gamma(a-p) + \dot{a}) \tag{5.3a}$$

$$f = -K\left(a + \left(\frac{1}{\gamma} + \beta_1\right)\dot{a}\right). \tag{5.3b}$$

Here, $a \in \mathbb{R}$ is a state variable newly introduced, $\beta_1 \geq 0$ is a constant that affects damping, and $\gamma > 0$ is an appropriate constant. Although the DAI (5.3) does not appear usable with common numerical integration schemes, it can be equivalently rewritten into the following ODE by using Theorem 2:

$$\dot{a} = \max\left(-\frac{\gamma a}{1+\gamma\beta_1}, \gamma(p-a)\right) \tag{5.4a}$$

$$f = -K\max\left(0, p + \beta_1\gamma(p-a)\right). \tag{5.4b}$$

This means that the contact model (5.3) can be used for numerical simulation employing common ODE solvers. The behaviors of the state variable a is defined by the ODE (5.4a) and the force f is determined by the output equation (5.4b). The Chapter 3 showed some numerical examples regarding the effects of β_1 and γ, but tuning guidelines for the parameters are not obtained yet.

Equation (5.4) implies that, in the model (5.3), the force f is always nonnegative and continuous with respect to p and a. This means that the model (5.3) never produces discontinuous or sticky forces, which are main drawbacks of KV model. In addition, a simple simulation result suggests that the model produces non-zero indentation at the time of the contact force being lost, as in Fig. 5.1(d), while HC model results in zero indentation. One limitation of the model (5.3) is that its force-indentation curve is not close to those of Hertz's

and HC models.

5.2 New contact model

5.2.1 Formulation of new model

To remove the limitation of linear contact-force produced by the previous contact model (5.3), this chapter proposes a new model defined by the following DAI:

$$0 \in a + \left(\frac{1}{\gamma} + \beta_1 + \beta_2 a\right)\dot{a} - \mathrm{dio}(\gamma(a - p|p|^{\lambda-1}) + \dot{a}) \tag{5.5a}$$

$$f = -K\left(a + \left(\frac{1}{\gamma} + \beta_1 + \beta_2 a\right)\dot{a}\right). \tag{5.5b}$$

Here, $\lambda \geq 1$ is a constant that determines the nonlinearity of the force-indentation relation and $\beta_1 \geq 0$ and $\beta_2 \geq 0$ are damping parameters. The parameter $\gamma > 0$ is an appropriate constant that makes it possible to rewrite the DAI (5.5) into an ODE. The units for the quantities a, K, β_1, β_2 and γ are m^λ, $\mathrm{N/m}^\lambda$, s, $\mathrm{s/m}^\lambda$ and s^{-1}, respectively. It is easy to see that the previous model (5.3) is a special case of the new model (5.5) with $\lambda = 1$ and $\beta_2 = 0$.

In the same manner as in the previous model (5.3), the DAI (5.3) can also be rewritten as an ODE that is tractable with numerical integration schemes. By the application of Theorem 2, (5.5) can be rewritten as follows:

$$\dot{a} = \max\left(-\frac{\gamma a}{1 + \gamma(\beta_1 + \beta_2 a)},\, \gamma(p|p|^{\lambda-1} - a)\right) \tag{5.6a}$$

$$f = -K \max\left(0,\, p|p|^{\lambda-1} + \gamma(\beta_1 + \beta_2 a)(p|p|^{\lambda-1} - a)\right) \tag{5.6b}$$

From (5.6), one can observe that, by setting $\beta_1 = 0$ and $\beta_2 = 0$, (5.6b) reduces to a Hertz's model without dissipation. This implies that the model (5.5) can also be viewed as an extension of Hertz's model.

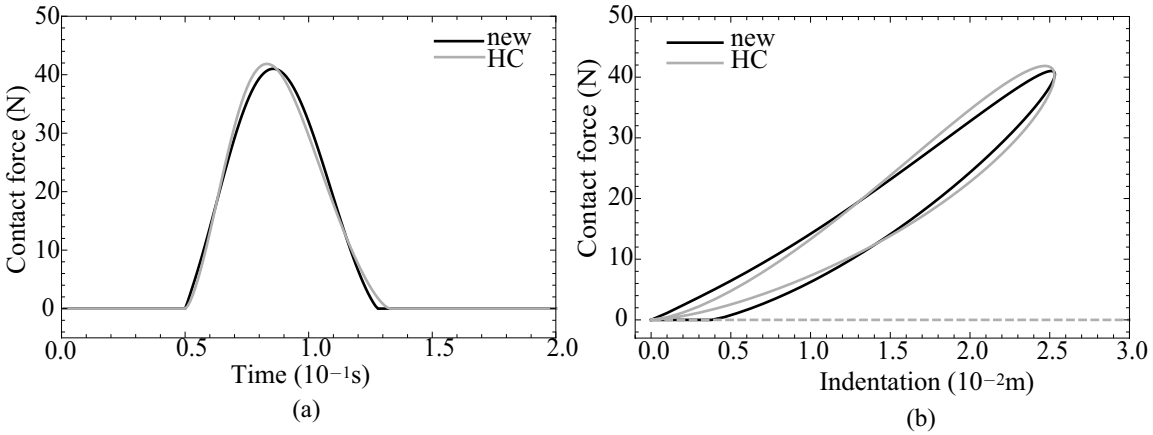

Figure 5.2: The force-indentation curves of the new model (5.6) and HC model (5.2); The parameters are chosen as; $f_e = 0$ N, $\lambda = 1.5$, $K = 10^4$ N/m$^{1.5}$, $\gamma = 2 \times 10^3$ s^{-1}, $\beta_1 = 3 \times 10^{-3}$ s, $\beta_2 = 0.1$ s/m$^{1.5}$ and $b_2 = 0.35$ s/m. The initial conditions are set as; $p(0) = -0.1$ m, $\dot{p}(0) = 2$ m/s and $a(0) = 0$ m$^{1.5}$. Figure and caption are reprinted, with permission from ASME: Journal of Applied Mechanics, "A Multistate Friction Model Described by Continuous Differential Equations", vol. 81, no. 2, pp. 021003-1:8, 2014, Xiaogang Xiong, Ryo Kikuuwe, and Motoji Yamamoto, Fig. 3 (see Appendix A2).

5.2.2 Comparison to HC model

In this section, the new model is compared to HC model through two simulations. Both simulations are performed for a system composed of a point mass $M > 0$ whose position is denoted as $p \in \mathbb{R}$ and a surface fixed at the origin. With a contact force $f \in \mathbb{R}$ and an external force $f_e \in \mathbb{R}$, the equation of motion of the system is described as follows:

$$M\ddot{p} = f + f_e. \tag{5.7}$$

Simulations are performed based on (5.7) with f being substituted by the output of the contact models. For the time integration, the fourth-order Runge Kutta method is used with the timestep size 1×10^{-3}s. The mass M is always set as $M = 1$ kg. In the first simulation, the mass runs into the fixed surface with initial velocity $\dot{p}(0) > 0$ and $f_e = 0$ while in the second one, the mass falls down to the fixed surface with $\dot{p}(0) = 0$ and is subjected by the gravity $f_e = Mg$ where g is the gravity acceleration. The parameters of both models are set so that they produce approximately the same COR with each other for the contact in the first

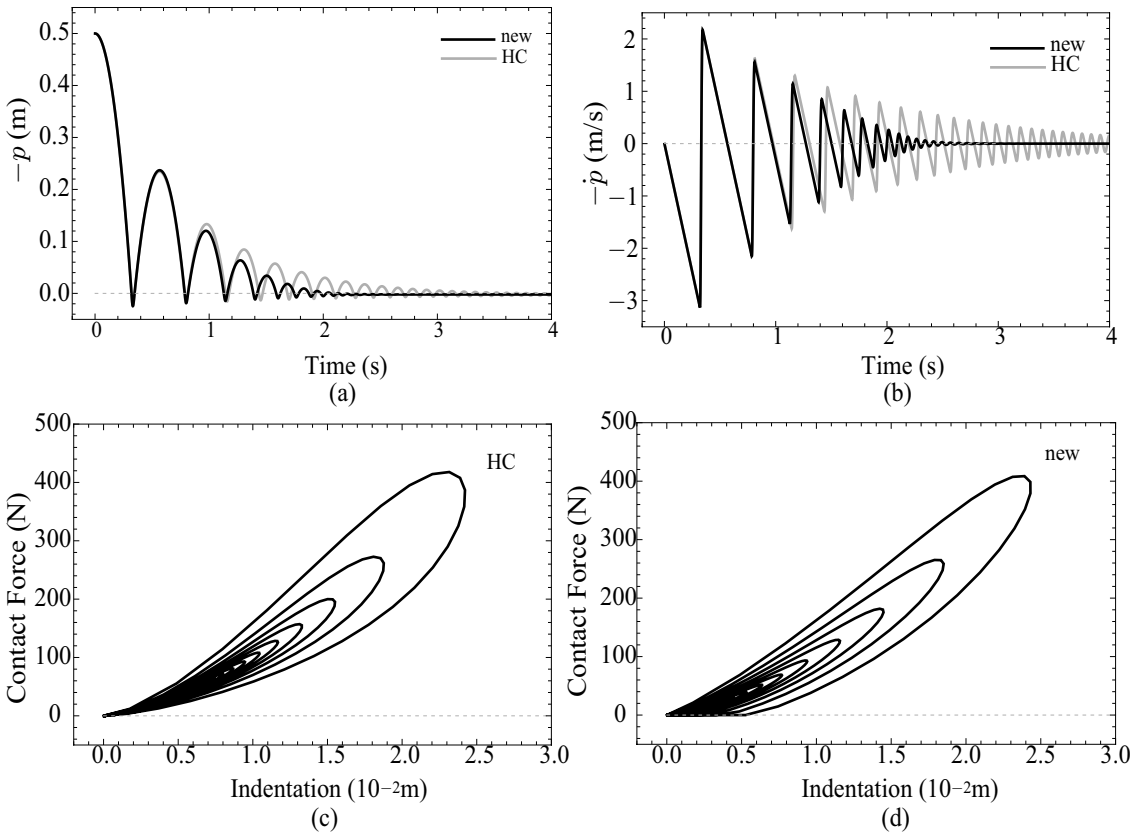

Figure 5.3: Simulation of bouncing motion by using the new model (5.6) and HC model (5.2). The parameters are set as; $f_e = Mg$, $\lambda = 1.5$, $K = 10^4$ N/m$^{1.5}$, $\gamma = 2 \times 10^3$ s^{-1}, $\beta_1 = 1.45 \times 10^{-3}$ s, $\beta_2 = 0.2$ s/m$^{1.5}$ and $b_2 = 0.2$ s/m. The initial conditions are set as; $p(0) = -0.5$ m, $\dot{p}(0) = 0$ m/s and $a(0) = 0$ m$^{1.5}$. Figure and caption are reprinted, with permission from ASME: Journal of Applied Mechanics, "A Multistate Friction Model Described by Continuous Differential Equations", vol. 81, no. 2, pp. 021003-1:8, 2014, Xiaogang Xiong, Ryo Kikuuwe, and Motoji Yamamoto, Fig. 4 (see Appendix A2).

simulation and for the first bouncing in the second simulation. The KV model (5.1) and the author's previous model (5.4) are not included in the comparison because of their unrealistic patterns of force-indentation curves.

Fig. 5.2 shows the first simulation result obtained with the new model and HC model. Fig. 5.2(a) shows that the peak value of the force-time curve of HC model shifts left, comparing that of the new model. Fig. 5.2(b) shows that the new model results in a non-zero indentation (approximately 0.4×10^{-2} m) when the contact force arrives in zero, while, in HC model, zero contact force is achieved only at the time of zero indentation. The nonzero indentation of the new model's curve implies that the contact object lose contact before it recover to its original shape. The new model's curve is also characterized by its downward convex shape similar to Hertz's model. Such features of the new model are in good agreement with empirical data in the literature, illustrated in Fig. 5.1(a).

Fig. 5.3(a) and (b) show the position and velocity results of the second simulation. It can be seen that, although the two models produce almost the same height of the second peak with each other, their subsequent behaviors are distinctly different. Specifically, the new model stops bouncing in a shorter time than the HC model. This difference can be attributed to the term $K\beta_1\dot{a}$ in the new model (5.5), which dissipate energy even when the penetration p is shallow.

Fig. 5.3(c) and (d) show the contact force-indentation curves. Fig. 5.3(c) shows that HC model results in the zero indentation when the contact force arrives back to zero, while Fig. 5.3(d) shows that the new model produces a non-zero indentation when the contact force becomes zero. The later simulation result is consistent with the experiment results in [4, 15].

5.3 Effects of parameters $\beta 1$, $\beta 2$ and γ

5.3.1 Force-indentation curves

In this section, the behaviors of the new model and the effects of the parameters of the new model are illustrated by some simulation results. Those results are obtained by integrating the system (5.7).

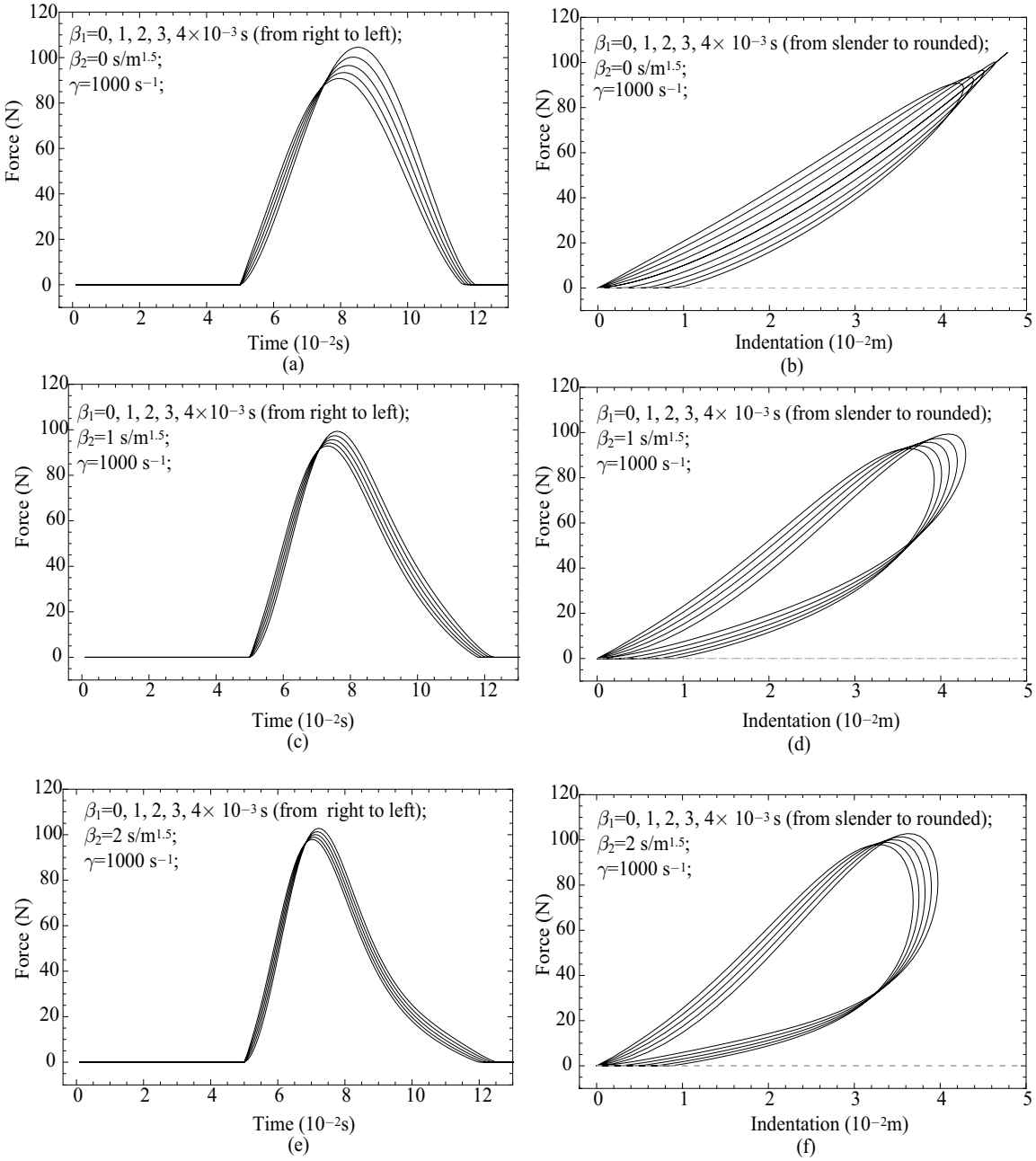

Figure 5.4: Influence of β_1 on the behaviors of the new model (5.5); The parameters are set as; $f_e = 0$ N, $\lambda = 1.5$ and $K = 10^4$ N/m$^{1.5}$. The initial conditions are set as; $p(0) = -0.1$ m, $\dot{p}(0) = 2$ m/s and $a(0) = 0$ m$^{1.5}$. Figure and caption are reprinted, with permission from ASME: Journal of Applied Mechanics, "A Multistate Friction Model Described by Continuous Differential Equations", vol. 81, no. 2, pp. 021003-1:8, 2014, Xiaogang Xiong, Ryo Kikuuwe, and Motoji Yamamoto, Fig. 5 (see Appendix A2).

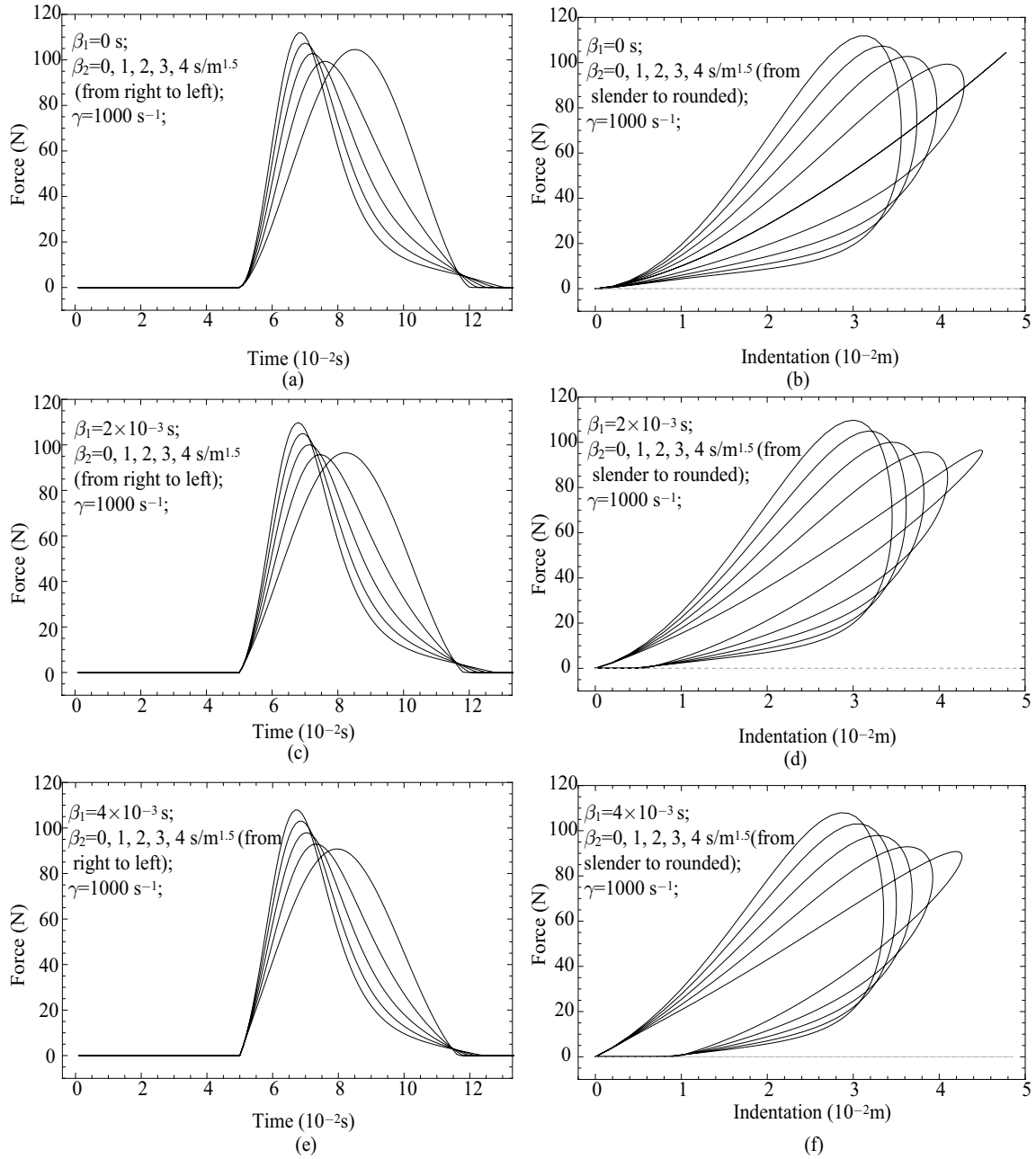

Figure 5.5: Influence of β_2 on the behaviors of the new model (5.5); The parameters are set as; $f_e = 0$ N, $\lambda = 1.5$ and $K = 10^4$ N/m$^{1.5}$. The initial conditions are set as; $p(0) = -0.1$ m, $\dot{p}(0) = 2$ m/s and $a(0) = 0$ m$^{1.5}$. Figure and caption are reprinted, with permission from ASME: Journal of Applied Mechanics, "A Multistate Friction Model Described by Continuous Differential Equations", vol. 81, no. 2, pp. 021003-1:8, 2014, Xiaogang Xiong, Ryo Kikuuwe, and Motoji Yamamoto, Fig. 6 (see Appendix A2).

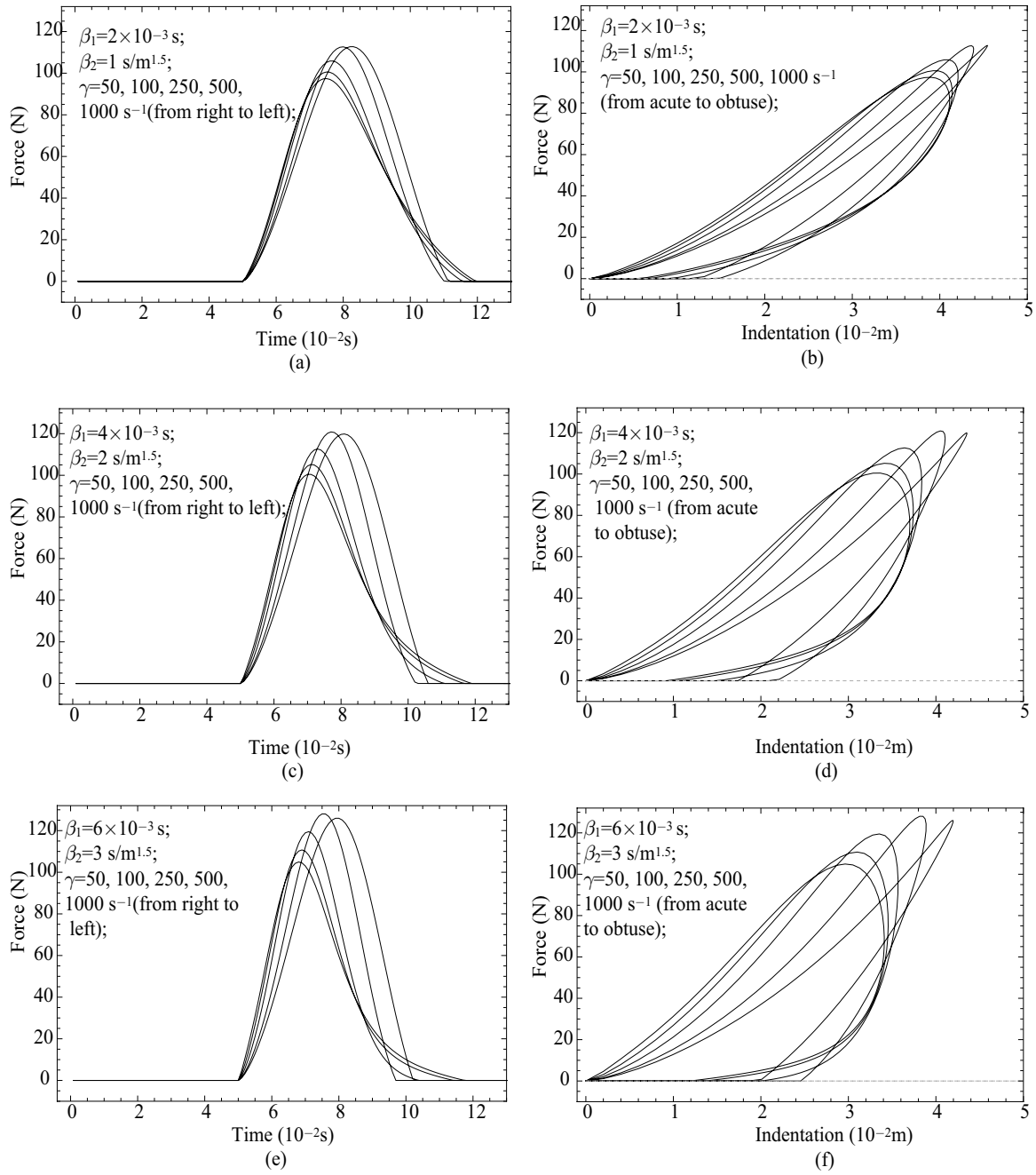

Figure 5.6: Influence of γ on the behaviors of the new model (5.5); The parameters are set as; $f_e = 0$ N, $\lambda = 1.5$ and $K = 10^4$ N/m$^{1.5}$. The initial conditions are set as; $p(0) = -0.1$ m and $a(0) = 0$ m$^{1.5}$. Figure and caption are reprinted, with permission from ASME: Journal of Applied Mechanics, "A Multistate Friction Model Described by Continuous Differential Equations", vol. 81, no. 2, pp. 021003-1:8, 2014, Xiaogang Xiong, Ryo Kikuuwe, and Motoji Yamamoto, Fig. 7 (see Appendix A2).

First, the effects of the three parameters β_1, β_2 and γ are numerically investigated. Fig. 5.4 shows the effect of β_1 with β_2 fixed at different values. For each fixed β_2, the variation of β_1 shows that the residual indentation increases as β_1 increases, as seen in Fig. 5.4(b), (d) or (f). In the special case of $\beta_1 = 0$ in Fig. 5.4(d) and (f), the force-indentation curve is close to that of HC model. Another important effect is that, as is seen in Fig. 5.4 (a), (c) or (e), an increase of β_1 results in an increase of the rate-of-change of the contact force (the slope of the curves in Fig. 5.4(a), (c) or (e)) at the beginning of contact. With a non-zero value of β_1, the force rate-of-change discontinuously changes with respect to time at the time of collision.

Next, Fig. 5.5 shows the effect of β_2 with β_1 fixed at different values. For each fixed β_1, the variation of β_2 shows that the force-indentation curve becomes more rounded as β_2 increases, as illustrated in Fig. 5.5(b), (d) or (f). In the special case of $\beta_1 = 0$, the force-indentation curve is close to that of HC model, as illustrated in Fig. 5.5(b). In addition, a larger β_2 results in the leftward shift of the peak time of the peak contact force and shorter duration of the compression phase. It should be noted that β_2 does not influence the residual indentation at the time of loss of contact force or the rate-of-change of the force at the time of collision.

Fig. 5.6 shows the effect of γ with β_1 and β_2 being fixed. The overall shape of the contact force-indentation is influenced by the value of γ. Fig. 5.6(a), (c) and (e) show that, as γ increases, the force-time curves become more unsymmetrical and the duration of the compression phase becomes shorter. Fig. 5.6(b), (d) and (f) show that, as γ becomes larger, the shape of the contact force-indentation changes from cute, triangle-like curves as those produced by the models in [49, 61–64] to obtuse, rounded curves as those produced by HC model.

From Fig. 5.4, Fig. 5.5 and Fig. 5.6, one may conclude that β_1 determines the residual indentation, β_2 determines the roundedness of the contact force-indentation curves, and that γ determines the overall shape of the contact force-indentation curves.

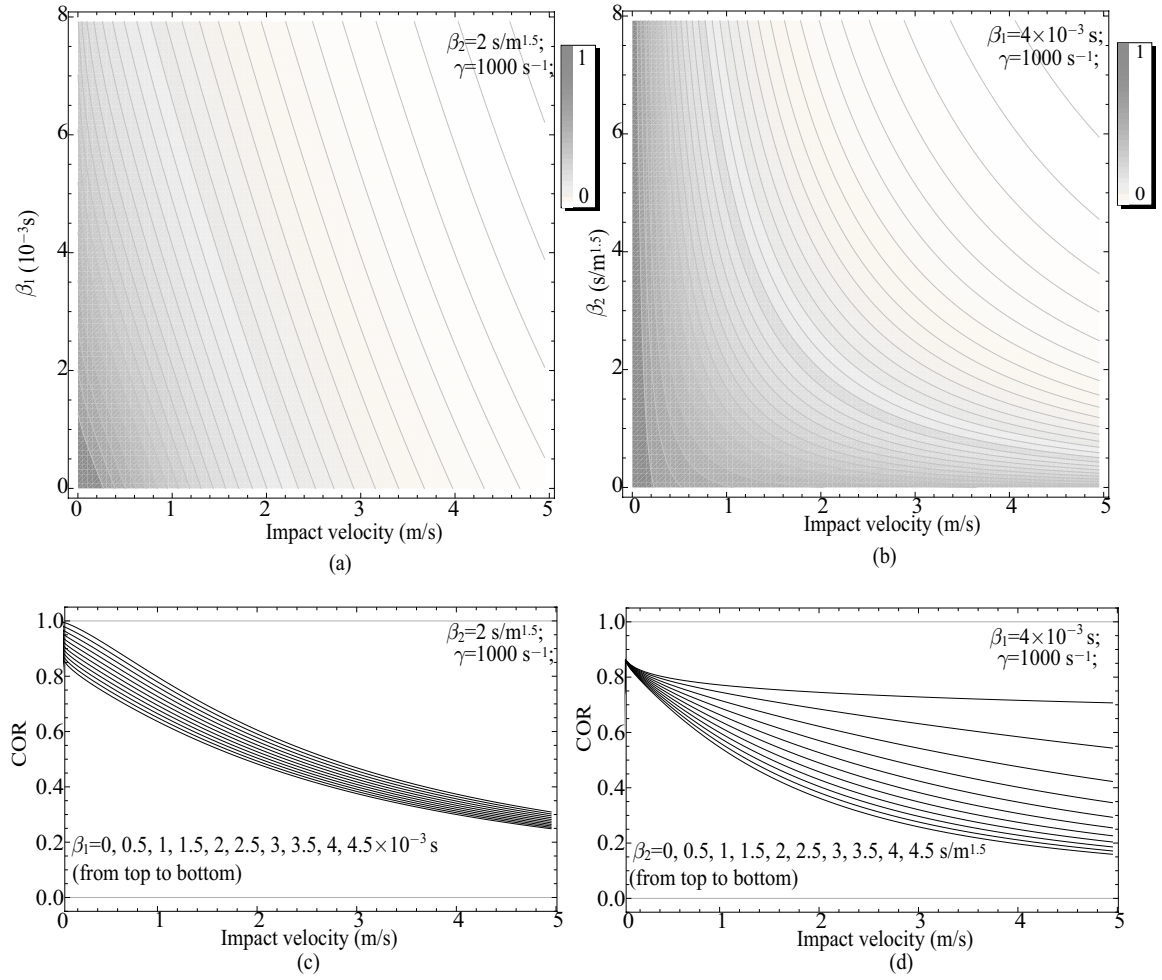

Figure 5.7: (a)(b) The COR as a function of β_1, β_2 and the impact velocity obtained from of the new model (5.5). (c)(d) The COR as a function of impact velocity. The parameters are set as; $f_e = 0$ N, $\lambda = 1.5$ and $K = 10^4$ N/m$^{1.5}$. The initial conditions are set as; $p(0) = -0.1$ m and $a(0) = 0$ m$^{1.5}$. Figure and caption are reprinted, with permission from ASME: Journal of Applied Mechanics, "A Multistate Friction Model Described by Continuous Differential Equations", vol. 81, no. 2, pp. 021003-1:8, 2014, Xiaogang Xiong, Ryo Kikuuwe, and Motoji Yamamoto, Fig. 8 (see Appendix A2).

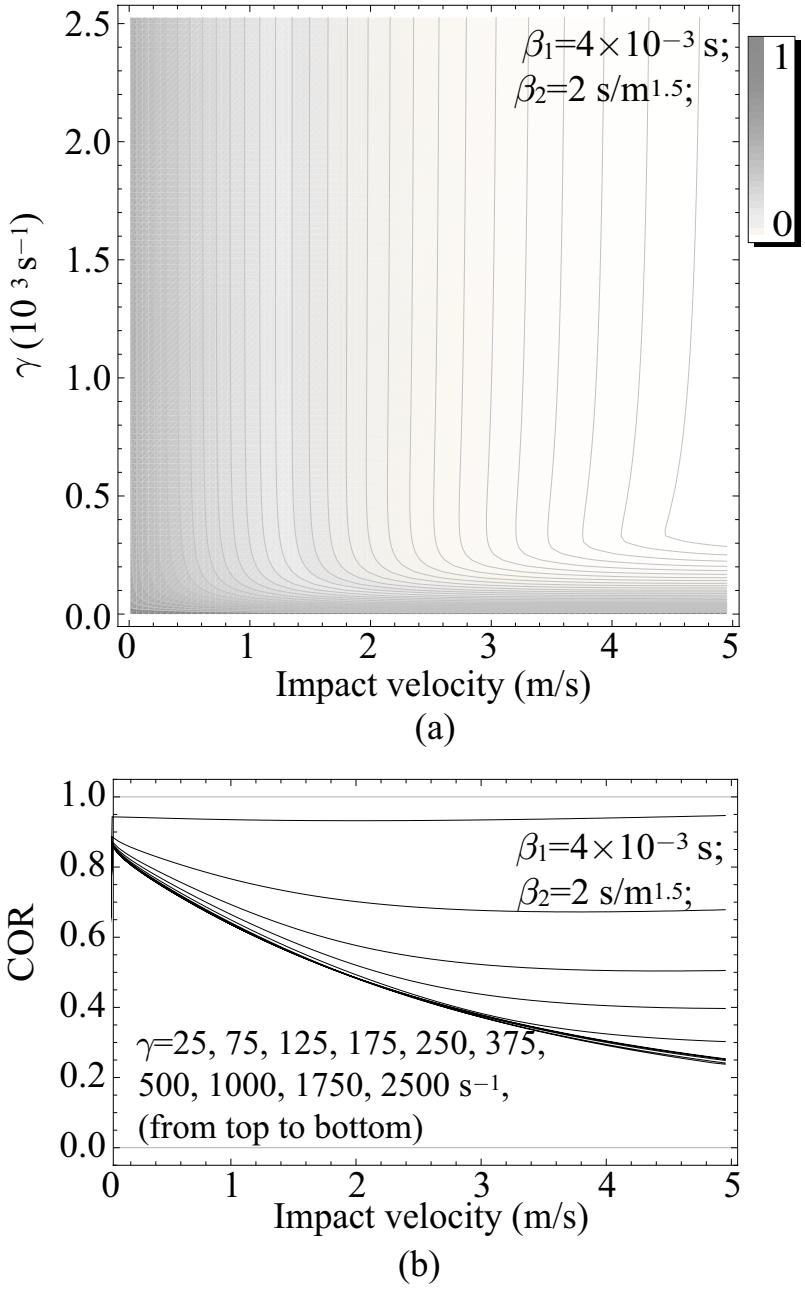

Figure 5.8: (a) The COR as a function of γ and the impact velocity obtained from of the new model (5.5). (b) The COR as a function of impact velocity. The parameters are set as; $f_e = 0$ N, $\lambda = 1.5$ and $K = 10^4$ N/m$^{1.5}$. The initial conditions are set as; $p(0) = -0.1$ m and $a(0) = 0$ m$^{1.5}$. Figure and caption are reprinted, with permission from ASME: Journal of Applied Mechanics, "A Multistate Friction Model Described by Continuous Differential Equations", vol. 81, no. 2, pp. 021003-1:8, 2014, Xiaogang Xiong, Ryo Kikuuwe, and Motoji Yamamoto, Fig. 9 (see Appendix A2).

5.3.2 Coefficient of restitution (COR)

From empirical studies in the literature [53, 60], it has been known that the COR decreases as the impact velocity increases. A set of simulation was performed to investigate the COR obtained by the new model.

Fig. 5.7(a) and (b) show the result, in which the COR is shown as a function of the impact velocity and the parameters β_1 and β_2. Fig. 5.7(c) and (d) show partial data sets from the data in Fig. 5.7(a) and (b), respectively. In all graphs, it can be seen that COR decreases as the impact velocity increases with any settings of β_1 and β_2. This feature is consistent with the known fact in the literature [53]. In addition, Fig. 5.7(c) and Fig. 5.7(d) both show that COR decreases as β_1 or β_2 increases, which is as expected considering that they are damping factors.

An important point in Fig. 5.7(c) and (d) is that, as the impact velocity approaches to zero, the COR does not converges to 1 except the special case $\beta_1 = 0$ shown in Fig. 5.7(c). This observation is consistent with the fact that, with $\beta_1 = 0$, the new model becomes close to HC model as illustrated in Fig. 5.5(b), and that HC model is intended to realize COR$= 1$ with the extreme case of zero impact velocity [16]. Another important point is that, in another special case of $\beta_2 = 0$, the corresponding COR is almost independent from the impact velocity, as shown by the top curve with a slight slope in Fig. 5.7(d). This supports the necessity of the term $K\beta_2 a\dot{a}$ with $\beta_2 > 0$ in the new model (5.5) to reproduce the COR depending on the impact velocity, which has been empirically known [51, 52, 60].

Fig. 5.8(a) shows the COR as a function of impact velocity and the parameter γ. The data of Fig. 5.8(b) is a part of those in Fig. 5.8(a). Fig. 5.8(b) shows that the monotonic decrease of COR with respect to the impact velocity is preserved at any values of γ, except the small value of γ, shown by the top curve in Fig. 5.8(b) and conformed by the bottom part of Fig. 5.8(a). This exception shows that when γ is small, the COR increases with a slight slope with respect to the impact velocity and this gives an agreement with the experiment result for the contact of a baseball dropped from different heights [15], which shows that the COR increases as the height becomes large. Fig. 5.8(b) also shows that, with fixed impact velocity, the COR decreases as γ increases, although it becomes very insensitive to γ when γ is large enough, illustrated by the almost parallel curves of top part of Fig. 5.8(a) and

the covered curves in Fig. 5.8(b). This fact is in contrast to the fact shown in Fig. 5.6(d), in which there are slight variation in the contact force-indentation curves even when γ is large. This means that a variation in γ has an effect of changing the shape of the contact force-indentation curve without causing much variation in the amount of energy loss.

In conclusions, one can see different effects of β_1, β_2 and γ on the COR-velocity curve from Fig. 5.7(c), (d) and Fig. 5.8(b). The parameter β_1 determines the COR at the zero impact velocity. The parameter β_2 determines the slope and the overall shape of the curve. The parameter γ influences both the zero-velocity COR and the slope, but its influence becomes smaller as its value increases.

5.4 Summary

This chapter has proposed an extension of the author' previous compliant contact model for the consistency with empirical results in the literature. The proposed model produces the three characteristics shown in the very beginning of this chapter. The proposed model contains two parameters $\{\beta_1, \beta_2\}$ for damping, two parameters $\{K, \lambda\}$ for static stiffness and one parameter $\{\gamma\}$ for shapes of the contact-force curves. Numerical results have shown that β_1 determines the magnitude of residual indentation and the rate-of-change of the force immediately after the collision, that β_2 influences the roundedness of the hysteresis curve in the force-indentation plane, and that γ influences the shapes of the contact force-indentation curves. The new model also reproduce a negative correlation between the COR and the impact velocity, which is a known result in the literature.

Future work should address design guidelines for the parameters to produce intended shapes of hysteresis curves and COR. Theoretical investigation on the properties of DAI (5.5) would be necessary to clarify the effects of various factors, such as the stiffness parameters K and λ, the damping factors β_1 and β_2 and the coefficient γ. In addition, a further extension of the model to include friction and oblique collision should be sought as a future topic of study.

Chapter 6

Concluding remarks

This dissertation focuses on the modeling of friction and contact by using differential algebraic inclusions (DAIs). It starts from the concept of differential inclusions (DIs), which are set-valued generalizations of ordinary differential equations (ODEs). Mechanical systems involving friction and contact are described as DIs when the contact bodies are idealized as rigid ones and impenetrable to each other. Integrations of DIs are troublesome due to the DIs' set-valued characteristics. In conventional regularization approaches, DIs are directly approximated as ODEs for the easiness of numerical integration. Those straightforward approximations lack the discontinuous nature of original DIs and can cause problems of unnatural behaviors. In this dissertation, DIs are first regularized as DAIs that inherit the discontinuous nature of original DIs. Then the DAIs provide a single-state friction model and a linear contact model to approximate DIs as ODEs. To enhance the applicability of friction and contact models in various engineering applications, the single-state friction and linear contact models are extended to more sophisticated versions such that they can capture more features of friction and contact phenomena. The single-state friction model is extend to a multistate version. It can capture the major friction properties that previous friction models do, such as the Stribeck effect, nondrifting property, stick-slip oscillation, presliding hysteresis with nonlocal memory, and frictional lag. Moreover, it is free from the problems that previous models suffer from, such as unbounded positional drift or discontinuous force. The linear contact model is extended to a nonlinear version. It can simultaneously satisfy the

major features of experimental data of soft-objects contact, such as continuity of the force at the time of collision, Hertz-like nonlinear force-indentation curve, and non-zero indentation at the time of loss of contact force. In contrast, previous contact models can only capture one or two of the three features.

The dissertation has first provided an overview of the conventional approaches to describe mechanical systems involving friction and contact phenomena. Those conventional approaches can be broadly categorized into two classes: hard-constraint approaches and regularization approaches. The hard-constraint approaches typically describe mechanical systems as DIs. The DIs are cumbersome to be integrated due to their set-valued characteristics. Regularization approaches can be used to approximate those DIs by ODEs and then lead to simple integration procedures. One of major problems of the regularization approaches is that they usually lack the discontinuous nature of the original DIs, which cause various unnatural behaviors in descriptions of mechanical systems.

To solve the above problems of hard-constraint and regularization approaches, Chapter 3 has proposed a new approach to regularize DIs. Different from conventional regularization approaches, here, DIs have been first relaxed into DAIs that can inherit the discontinuous nature of DIs. Then, the DAIs were transformed into ODEs, providing a single-state friction model and a linear contact model. This method provides a simple procedure to effectively simulate mechanical systems involving friction and contact with preserving the discontinuous nature. Three examples have been taken to illustrate the simplicity and efficiency of the proposed method. Those examples have shown that, excepting some small penetrations, the proposed method appropriately describe the overall behaviors of mechanical systems that are originally described by DIs.

To extend the application scope of previous friction and contact models to engineering applications, Chapter 4 and Chapter 5 have extended the single-state friction model and linear contact model in Chapter 3 into more sophisticated versions such that they can capture more features of experimental results of friction and contact phenomenon and inherit their advantages, i.e., preserving the discontinuous nature.

Chapter 4 has extended the single-state friction model in Chapter 3 into a multistate version. This extended model is composed of parallel connection of a number of elastoplas-

tic elements. Each elastoplastic element, representing an asperity on the contact surfaces involving friction, has been described by the single-state friction model. This new model reproduces major features of friction phenomena reported in the literature [14, 21, 35, 38], such as the Stribeck effect, nondrifting property, stick-slip oscillation, presliding hysteresis with nonlocal memory, and frictional lag. Moreover, the new model does suffer from the problems of previous regularized models. The new model has been validated through comparisons between its simulation results and empirical results reported in the literature [14, 22]. It also has been experimentally validated in [99].

Chapter 5 has extended the linear contact model in Chapter 3 to a nonlinear version. The new contact model has been equipped with a Hertz-like power-law nonlinearity and a displacement dependent viscosity term based on its original version. The contact force and indentation of this model is consistent with the experimental data in the following three features: (i) continuity of the force at the time of collision, (ii) Hertz-like nonlinear force-indentation curve, and (iii) non-zero indentation at the time of loss of contact force. On the contrary, the conventional KV model only satisfies (ii) while HC model only satisfies (i) and (ii). The new model has been validated through comparisons among the simulation results of the new model, the HC model, and empirical results reported in the literature [2–4]. The parameter effects and the COR properties of the new model have been investigated through numerical simulations.

This dissertation has some limitations on its incomplete contents. Although the multistate friction model has been validated by experiments in [99], its parameters were only identified by try and error, which is a rough way and can not achieve optimal performance of friction compensation. Real-time methods for identifying the multiple parameters of the multistate friction model should be developed for the easinesses of engineering applications. Another limitation is that the performances of the proposed nonlinear contact model have only been validated through numerical methods. Experimental validations should be done in future study. Meanwhile, the guideline of parameter adjustments for this contact model should be illustrated through simulations and experiments.

References

[1] M. F. J. Awrejcewicz and P. Olejnik, "On continuous approximation of discontinuous systems," *Nonlinear Analysis: Theory, Methods & Applications*, vol. 62, no. 7, pp. 1317–1331, 2005.

[2] T. Yamamoto, B. Vagvolgyi, K. Balaji, L. L. Whitcomb, and A. M. Okamura, "Tissue property estimation and graphical display for teleoperated robot-assisted surgery," in *Proceedings of IEEE International Conference on Robotics and Automation*, pp. 4239–4245, 2009.

[3] T. Yamamoto, *Applying tissue models in teleoperated robot-assisted surgery*. PhD Thesis, Johns Hopkins University, Baltimore, Maryland, 2011.

[4] R. Cross, "The bounce of a ball," *American Journal of Physics*, vol. 67, no. 3, pp. 222–227, 1999.

[5] R. I. Leine, C. Glocker, and D. H. V. Campen, "Nonlinear dynamics and modeling of various wooden toys with impact and friction," *Journal of Vibration and Control*, vol. 9, no. 1–2, pp. 25–78, 2001.

[6] C. Glocker, "Set-Valued Force Laws, Dynamics of Non-Smooth Systems," Lecture Notes in Applied Mechanics, Vol. 1. Springer-Verlag, Berlin, 2001.

[7] S. Schoeder, H. Ulbrich, and T. Schindler, "Discussion of the Gear-Gupta-Leimkuhler method for impacting mechanical systems," *Multibody System Dynamics*, 2013. In press.

[8] P. Fores, R. Leine, and C. Glocker, "Modeling and analysis of planar rigid multi-body systems with translational clearance joints based on the non-smooth dynamics approach," *Multibody System Dynamics*, vol. 23, no. 2, pp. 165–190, 2010.

[9] C. Glocker and F. Pfeiffer, "Multiple impacts with friction in rigid multi-body systems," *Nonlinear Dynamics*, vol. 7, no. 4, pp. 471–497, 1995.

[10] N. Nguyen and B. Brogliato, "Multiple impacts in dissipative granular chains," Lecture Notes in Applied and Computational Mechanics, Vol. 72. Springer-Verlag, Berlin, 2013.

[11] M. Förg, F. Pfeiffer, and H. Ulbrich, "Simulation of unilateral constrained systems with many bodies," *Multibody System Dynamics*, vol. 14, no. 2, pp. 137–154, 2005.

[12] Y. Gonthier, J. Mcphee, C. Lange, and J. C. Piedbœuf, "A regularized contact model with asymmetric damping and dwell-time dependent friction," *Multibody System Dynamics*, vol. 11, no. 3, pp. 209–233, 2004.

[13] D. Quinn, "A new regularization of coulomb friction," *Transactions of the ASME: Journal of Vibration and Acoustics*, vol. 126, no. 3, pp. 391–397, 2004.

[14] H. Olsson, K. Åström, C. Canudas de Wit, M. Gäfvert, and P. Lischinsky, "Friction models and friction compensation," *European Journal of Control*, vol. 4, no. 3, pp. 176–195, 1998.

[15] R. Cross, "Physics of Baseball & Softball," Springer, 2011.

[16] K. Hunt and F. Crossley, "Coefficient of restitution interpreted as damping in vibroimpact," *ASME Journal of Applied Mechanics*, pp. 440–445, 1975.

[17] R. G. Adams and M. Nosonovsky, "Contact modeling-forces," *Tribology International*, vol. 33, pp. 431–442, 2000.

[18] V. Acary and B. Brogliato, "Numerical Methods for Nonsmooth Dynamical Systems," Lecture Notes in Applied and Computational Mechanics, Vol. 35. Springer-Verlag, Berlin, 2008.

[19] V. Acary and B. Brogliato, "Time-stepping numerical simulation of switched circuits within the nonsmooth dynamical systems approach," *IEEE Transactions on Computer-Aided Design of Integrated Circuits and Systems*, vol. 29, no. 7, pp. 1402–1055, 2010.

[20] P. Dahl, "A solid friction model," tech. rep., Aerospace Corporation, 1968.

[21] C. Canudas de Wit, H. Olsson, K. J. Åström, and P. Lischinsky, "A new model for control of sytem with friction," *IEEE Transactions on Automatic Control*, vol. 40, no. 3, pp. 419–425, 1995.

[22] V. Lampaert, F. Al-Bender, and J. Swevers, "Experimental characterization of dry friction at low velocities on a developed tribometer setup for macroscopic measurements," *Tribology Letters*, vol. 16, no. 1-2, pp. 95–105, 2004.

[23] F. Al-Bender, V. Lampaert, and J. Swevers, "Modeling of dry sliding friction dynamics: From heuristic models to physically motivated models and back," *Chaos: An Interdisciplinary Journal of Nonlinear Science*, vol. 14, no. 2, pp. 446–450, 2004.

[24] J. Swevers, F. Al-Bender, C. G. Ganseman, and T. Prajogo, "An integrated friction model structure with improved presliding behavior for accurate friction compensation," *IEEE Transactions on Automatic Control*, vol. 45, no. 4, pp. 675–686, 2000.

[25] B. Armstrong-Hélouvry, P. Dupond, and C. Canudas De Wit, "A survey of models, analysis tools and compensation methods for the control of machines with friction," *Automatica*, vol. 30, no. 7, pp. 1083–1138, 1994.

[26] V. Lampaert, *Modelling and control of dry sliding friction in mechanical systems*. PhD thesis, Katholieke Universiteit Leuven, Belgium, 2003.

[27] L. Freidovich, A. Robertsson, A. Shiriaev, and R. Johansson, "Lugre-model-based friction compensation," *IEEE Transactions on Control System Technology*, vol. 18, no. 1, pp. 194–200, 2010.

[28] T. Tjahjowidodo, F. Al-Bender, H. Van Brussel, and W. Symens, "Friction characterization and compensation in electro-mechanical systems," *Journal of Sound and Vibration*, vol. 308, no. 3-5, pp. 632–646, 2007.

[29] R. Kikuuwe, Y. Kobayashi, and H. Fujimoto, "Coulomb-friction-based needle insertion/withdrawal model and its discrete-time implementation," in *Proceedings of EuroHaptics 2006*, pp. 207–212, 2006.

[30] J. G. Hale, B. Hohl, S.-H. Hyon, T. Matsubara, E. M. Moraud, and G. Cheng, "Highly precise dynamic simulation environment for humanoid robots," *Advanced Robotics*, vol. 22, no. 10, pp. 1075–1105, 2008.

[31] K. J. Åström and C. Canudas-de-Wit, "Revisiting the LuGre friction model," *IEEE Control Systems Magazine*, vol. 28, no. 6, pp. 101–114, 2008.

[32] P. Dupont, V. Hayward, B. Armstrong, and F. Altpeter, "Single state elastoplastic friction models," *IEEE Transactions on Automatic Control*, vol. 47, no. 5, pp. 787–792, 2002.

[33] X. Xiong, R. Kikuuwe, and M. Yamamoto, "A differential-algebraic method to approximate nonsmooth mechanical systems by ordinary differential equations," *Journal of Applied Mathematics, Vol. 2013, Article ID 320276*, 2013.

[34] V. Lampaert, J. Swevers, and F. Al-Bender, "Modification of the Leuven integrated friction model structure," *IEEE Transactions on Automatic Control*, vol. 47, no. 4, pp. 683–687, 2002.

[35] F. Al-Bender, V. Lampaert, and J. Swevers, "The generalized maxwell-slip model: a novel model for friction simulation and compensation," *IEEE Transactions on Automatic Control*, vol. 50, no. 11, pp. 1883–1887, 2005.

[36] M. Boegli, T. De Laet, J. De Schutter, and J. Swevers, "A Smoothed GMS friction model suited for gradient-based friction state estimation," in *Proceedings of 2012 American Control Conference*, pp. 2627–2632, 2012.

[37] M. Boegli, T. De Laet, J. De Schutter, and J. Swevers, "A Smoothed GMS friction model for Moving Horizon friction state and parameter estimation," in *Proceedings of 12th IEEE International Workshop on Advanced Motion Control*, pp. 1–6, 2012.

[38] F. Al-Bender, V. Lampaert, and J. Swevers, "A novel generic model at asperity level for dry friction force dynamics," *Tribology Letters*, vol. 16, no. 1-2, pp. 81–93, 2004.

[39] K. De Moerlooze, F. Al-Bender, and H. Van Brussel, "A generalized asperity-based friction model," *Tribology Letters*, vol. 40, no. 1, pp. 113–130, 2010.

[40] F. Al-Bender and J. Swevers, "Characterization of friction force dynamics," *IEEE Control Systems Magazine*, vol. 28, no. 6, pp. 64–81, 2008.

[41] R. Burridge and L. Knopoff, "Model and theoretical seismicity," *Bulletin of the Seismological Society of America*, vol. 57, no. 3, pp. 341–371, 1967.

[42] A. E. Filippov and V. L. Popov, "Modified Burridge-Knopoff model with state dependent friction," *Tribology International*, vol. 43, no. 8, pp. 1392–1399, 2010.

[43] C. F. Jenkin, "A mechanical model illustrating the behaviour of metals under," *Engineering*, vol. 114, p. 603, 1922.

[44] W. D. Iwan, "A distributed-element model for hysteresis and its steady-state dynamic response," *Transactions of ASME: Journal of Applied Mechanics*, vol. 33, no. 4, pp. 893–900, 1966.

[45] M. Goldfarb and N. Celanovic, "A lumped parameter electromechanical model for describing the nonlinear behavior of piezoelectric actuators," *Transactions of ASME: Journal of Dynamic Systems, Measurement, and Control*, vol. 119, pp. 478–485, 1997.

[46] B. J. Lazan, "Damping of Materials and Members in Structural Mechanics," Pergamon Press, London, U.K., 1968.

[47] X. Mu and Q. Wu, "On impact dynamics and contact events for for biped robots via impact effects," *IEEE Transaction on Systems, Man and Cyberentics-Part B: Cyberentics*, vol. 36, no. 6, pp. 1364–1372, 2006.

[48] P. Flores, J. Ambrósio, J. C. P. Claro, and H. M. Lankarani, "Influence of the contact-impact force model on the dynamic response of multi-body systems," *Proceedings*

of the Institution of Mechanical Engineers, Part K: Journal of Multi-body Dynamics, vol. 220, no. 1, pp. 21–34, 2006.

[49] K. A. Ismail and W. J. Stronge, "Viscoplastic analysis for direct impact of sports balls," *International Journal of Non-Linear Mechanics*, vol. 47, no. 2, pp. 16–21, 2012.

[50] K. Hanley, F. Collins, K. Cronin, E. Byrne, K. Moran, and D. Brabazon, "Simulation of the impact response of a sliotar core with linear and non-linear contact models," *International Journal of Impact Engineering*, vol. 50, pp. 113–122, 2012.

[51] T. Schwager and T. Pöschel, "Coefficient of restitution and linear-dashpot model revisited," *Granular Matter*, vol. 6, no. 9, pp. 465–469, 2007.

[52] R. Ramírez, T. Pöschel, N. V. Brilliantov, and T. Schwager, "Coefficient of restitution of colliding viscoleastic spheres," *Physical Review E*, vol. 60, no. 4, pp. 4465–4472, 1999.

[53] G. Gilardi and I. Sharf, "Literature survey of contact dynamics modelling," *Mechanism and Machine Theory*, vol. 37, no. 10, pp. 1213–1239, 2002.

[54] M. Machado, P. Moreira, P. Flores, and H. Lankarani, "Compliant contact force models in multibody dynamics: evolution of the Hertz contact theory," *Mechanism and Machine Theory*, vol. 53, pp. 99–121, 2012.

[55] D. W. Marhefka and D. E. Orin, "A compliant contact model with nonlinear damping for simulation of robotic systems," *IEEE Transaction on System, Man and Cybernetics-Part A: Systems and Humans*, pp. 566–572, 1999.

[56] P. Flores, M. Machado, M. T. Silva, and J. M. Martins, "On the continuous contact force models for soft materials in multiobdy dynamics," *Multibody System Dynamics*, vol. 25, no. 3, pp. 357–375, 2011.

[57] A. Roy and J. A. Carretero, "A damping term based on material properties for the volume-based contact dynamics model," *International Journal of Non-Linear Mechanics*, vol. 47, no. 3, pp. 103–112, 2012.

[58] A. Haddadi and K. Hashtrudi-Zaad, "A new method for online parameter estimation of hunt-crossley environment dynamic models," in *Proceedings of IEEE/RSJ International Conference on Intelligent Robots and Systems*, pp. 981–986, 2008.

[59] S. Sørensen, M. Hansen, M. Ebbesen, and O. Mouritsen, "Implicit identification of contact parameters in a continuous chain model," *Modeling, Identification and Control*, vol. 32, no. 1, pp. 1–15, 2011.

[60] Y. Zhang and I. Sharf, "Validation of nonlinear viscoelastic contact force models for low speed impact," *ASME Journal of Applied Mechanics*, vol. 76, no. 5, pp. 051002–1–051002–12, 2009.

[61] M. Gharib and Y. Hurmuzlu, "A new force model for low coefficient of restitution impact," *ASME Journal of Applied Mechanics*, vol. 79, no. 6, pp. 064506.1–064506.5, 2012.

[62] H. M. Lankarani and P. E. Nikaravesh, "Continuous contact force models for impact analysis on multibody systems," *Nonlinear Dynamics*, vol. 5, pp. 193–207, 1994.

[63] K. A. Ismail and W. J. Stronge, "Impact of viscoplastic bodies: dissipation and restitution," *ASME Journal of Applied Mechanics*, vol. 75, no. 6, pp. 061011.1–061011.5, 2008.

[64] A. S. Yigit, A. P. Christoforou, and M. A. Majeed, "A nonlinear visco-elastoplastic impact model and the coefficient of restitution," *Nonlinear Dynamics*, vol. 66, no. 4, pp. 509–521, 2011.

[65] R. Kikuuwe, S. Yasukouchi, H. Fujimoto, and M. Yamamoto, "Proxy-based sliding mode control: a safer extension of PID position control," *IEEE Transactions on Robotics*, vol. 26, no. 4, pp. 670–683, 2010.

[66] R. Kikuuwe, M. Yamamoto, and H. Fujimoto, "Velocity-bounding stiff position controller," in *Proceeding of IEEE/RSJ International Conference on Intelligent Robots and Systems*, pp. 3050–3055, 2006.

[67] B. Brogliato, A. Daniilidis, C. Lemarechal, and V. Acary, "On the equivalence between complementarity systems, projected systems and differential inclusions," *Systems & Control Letters*, vol. 55, no. 1, pp. 45–51, 2006.

[68] D. Karnopp, "Computer simulation of stick-slip friction in mechanical dynamic systems," *Transactions of the ASME: Journal of Dynamic Systems, Measurement, and Control*, vol. 107, no. 1, pp. 100–103, 1985.

[69] R. Kikuuwe, N. Takesue, A. Sano, H. Mochiyama, and H. Fujimoto, "Admittance and impedance representations of friction based on implicit Euler integration," *IEEE Transactions on Robotics*, vol. 22, no. 6, pp. 1176–1188, 2006.

[70] P. Dupont, V. Hayward, B. Armstrong, and F. Altpeter, "Single state elastoplastic friction models," *IEEE Transactions on Automatic Control*, vol. 47, no. 5, pp. 787–792, 2002.

[71] J. Bastien and C. Lamarque, "Persoz's gephyroidal model described by a maximal monotone differential inclusion," *Archives of Applied Mechanics*, vol. 78, no. 5, pp. 393–407, 2008.

[72] R. Kikuuwe and M. Yamamoto, "A modular software architecture for simulating mechanical systems involving coulomb friction integrable by the runge-kutta method," in *Proceedings of the 2008 IEEE/RSJ International Conference on Intelligent Robots and Systems*, pp. 2277–2282, 2008.

[73] C. Glocker and C. Studer, "Formulation and preparation for numerical evaluation of linear compementarity systems in dynamics," *Multibody System Dynamics*, vol. 13, no. 4, pp. 447–463, 2005.

[74] M. Anitescu and F. Porta, "Formulating dynamic multi-rigid-body contact problems with friction as solvable linear complementarity problems," *Nonlinear Dynamics*, vol. 14, no. 3, pp. 231–247, 1997.

[75] D. Stewart:, "Rigid-body dynamics with friction and impact," *SIAM Review*, vol. 42, no. 1, pp. 3–39, 2000.

[76] M. Anitescu and D. Hart:, "A constraint-stabilized time-stepping approach for rigid multibody dynamics with joints, contact and friction," *International Journal for Numerical Methods in Engineering*, vol. 60, no. 14, pp. 2335–2371, 2004.

[77] F. Porta and M. Anitescu, "A time-stepping method for stiff multibody dynamics with contact and friction," *International Journal for Numerical Methods in Engineering*, vol. 55, no. 7, pp. 753–784, 2002.

[78] M. Vukobratović and V. Potkonjak, "Dynamics of contact tasks in robotics. part I: General model of robot interacting with environment," *Mechanism and Machine Theory*, vol. 34, no. 6, pp. 923–942, 1999.

[79] K. Hunt and F. Crossley, "Coefficient of restitution interpreted as damping in vibroimpact," *ASME Journal of Applied Mechanics*, vol. 42, pp. 440–445, 1975.

[80] R. Kikuuwe and H. Fujimoto, "Incorporating geometric algorithms in impedance- and admittance-type haptic rendering," in *Proceedings of the Second Joint Eurohaptics Conference and Symposium on Haptic Interfaces for Virtual Environment and Teleoperator Systems*, pp. 249–254, 2007.

[81] P. Fores and J. Ambrósio, "On the contact detection for contact-impact analysis in multibody systems," *Multibody System Dynamics*, vol. 24, no. 1, pp. 103–122, 2010.

[82] L. Luo and M. Nahon, "Development and validation of geometry-based compliant contact models," *Transactions of the ASME: Journal of Computational and Nonlinear Dynamics*, vol. 6, p. 011004, 2011.

[83] M. Anitescu, F. Porta, and D. Stewart, "Time-stepping for three-dimensional rigid body dynamics," *Computer Methods in Applied Mechanics and Engineering*, vol. 177, no. 3, pp. 187–193, 1999.

[84] J. Baumgarte, "Stabilization of constraints and integrals of motion in dynamical systems," *Computer Methods in Applied Mechanics and Engineering*, vol. 1, no. 1, pp. 1–16, 1972.

[85] X. Xiong, R. Kikuuwe, and M. Yamamoto, "A differential-algebraic multistate friction model," in *In Simulation, Modeling, and Programming for Autonomous Robots, Lecture Notes in Computer Science* (I. Noda, D. B. Noriaki Ando, and J. J. Kuffner, eds.), pp. 77–88, Springer, 2012.

[86] X. Xiong, R. Kikuuwe, and M. Yamamoto, "A multistate friction model described by continuous differential equations," *Tribology Letters*, vol. 51, no. 3, pp. 513–523, 2013.

[87] S. Grami and P. Bigras, "Identification of the GMS friction model based on a robust adaptive observer," *International Journal of Modelling, Identification and Control*, vol. 5, no. 4, pp. 297–304, 2008.

[88] C. C. Casanova, E. R. De Pieri, U. F. Moreno, and E. B. Castelan, "Friction compensation in flexible joints robot with GMS model: Identification, control and experimental results," in *Proceedings of the International Federation of Automatic Control*, pp. 11793–11798, 2008.

[89] I. Nilkhamhang and A. Sano, "Adaptive friction compensation using the GMS model with polynomial Stribeck function," in *Proceedings of the 2006 IEEE International Conference on Control Applications*, pp. 1085–1090, 2006.

[90] V. Lampaert, F. Al-Bender, and J. Swevers, "A generalized Maxwell-slip friction model appropriate for control purposes," in *Proceedings of IEEE International Conference on Physics and Control*, pp. 1170–1177, 2003.

[91] J. Bastien and C.-H. Lamarque, "Persoz's gephyroidal model described by a maximal monotone differential inclusion," *Archive of Applied Mechanics*, vol. 58, no. 5, pp. 393–407, 2008.

[92] J. Bastien, M. Schatzman, and C.-H. Lamarque, "Study of an elastoplastic model with an infinite number of internal," *European Journal of Mechanics A/Solids*, vol. 21, no. 2, pp. 199–222, 2002.

[93] K. De Moerlooze and F. Al-Bender, "On the relationship between normal load and friction force in pre-sliding frictional contacts. part 2: Experimental investigation," *Wear*, vol. 269, no. 3-4, pp. 183–189, 2010.

[94] D. P. Hess and A. Soom, "Friction at a lubricated line contact operating at oscillating sliding velocities," *Transactions of ASME: Journal of Tribology*, vol. 112, no. 1, pp. 147–152, 1990.

[95] K. Worden, C. X. Wong, U. Parlitz, A. Hornstein, D. Engster, T. Tjahjowidodo, F. Al-Bender, D. Rizos, and S. Fassois, "Identification of pre-sliding and sliding friction dynamics: Grey box and black-box models," *Mechanical Systems and Signal Processing*, vol. 21, no. 1, pp. 514–534, 2007.

[96] M. Ruderman and T. Bertram, "Two-state dynamic friction model with elastoplasticity," *Mechanical Systems and Signal Processing*, vol. 39, no. 1-2, pp. 316–332, 2013.

[97] X. Xiong, R. Kikuuwe, and M. Yamamoto, "A differential-algebraic contact model with nonlinear compliance," in *Proceedings of the ASME 2012 5th Dynamic Systems and Control Conference*, 2012. DSCC2012-MOVIC2012-8642.

[98] X. Xiong, R. Kikuuwe, and M. Yamamoto, "A contact force model with nonlinear compliance and residual indentation," *Transactions of ASME: Journal of Applied Mechanics*, vol. 81, no. 2, pp. 021003.1–021003.8, 2013.

[99] A. Ahmad, K. Andersson, U. Sellgren, and M. Boegli, "A Smoothed GMS friction model suited for gradient-based friction state estimation," in *Proceedings of the ASME 2013 Dynamic Systems and Control Conference*, 2013. DSCC2013-3982.

Appendix A: Copyright Permissions

Appendix A1: Copyright permission for Chapter 4

SPRINGER LICENSE
TERMS AND CONDITIONS

Jan 01, 2014

This is a License Agreement between Xiaogang Xiong ("You") and Springer ("Springer") provided by Copyright Clearance Center ("CCC"). The license consists of your order details, the terms and conditions provided by Springer, and the payment terms and conditions.

All payments must be made in full to CCC. For payment instructions, please see information listed at the bottom of this form.

License Number	3273440422331
License date	Nov 21, 2013
Licensed content publisher	Springer
Licensed content publication	Tribology Letters
Licensed content title	A Multistate Friction Model Described by Continuous Differential Equations
Licensed content author	Xiaogang Xiong
Licensed content date	Jan 1, 2013
Volume number	51
Issue number	3
Type of Use	Thesis/Dissertation
Portion	Full text
Number of copies	1
Author of this Springer article	Yes and you are a contributor of the new work
Order reference number	120
Title of your thesis / dissertation	APPLICATIONS OF DIFFERENTIAL ALGEBRAIC INCLUSIONS ON FRICTION AND CONTACT MODELING
Expected completion date	Mar 2014
Estimated size(pages)	110
Total	0 JPY
Terms and Conditions	

Objection to Contrary Terms
Springer Science + Business Media hereby objects to any terms contained in any purchase order, acknowledgment, check endorsement or other writing prepared by you, which terms are inconsistent with these terms and conditions or CCC's Billing and Payment terms and conditions. These terms and conditions, together with CCC's Billing and Payment terms and conditions (which are incorporated herein), comprise the entire agreement between you and Springer Science + Business Media (and CCC) concerning this licensing transaction. In the event of any conflict between your obligations established by these terms and conditions and those established by CCC's Billing and Payment terms and conditions, these terms and conditions shall control.

Jurisdiction
All disputes that may arise in connection with this present License, or the breach thereof, shall be settled exclusively by arbitration, to be held in The Netherlands, in accordance with Dutch law, and to be conducted under the Rules of the 'Netherlands Arbitrage Instituut' (Netherlands Institute of Arbitration). ***OR:***

All disputes that may arise in connection with this present License, or the breach thereof, shall be settled exclusively by arbitration, to be held in the Federal Republic of Germany, in accordance with German law.

Other terms and conditions:

v1.3

If you would like to pay for this license now, please remit this license along with your payment made payable to "COPYRIGHT CLEARANCE CENTER" otherwise you will be invoiced within 48 hours of the license date. Payment should be in the form of a check or money order referencing your account number and this invoice number RLNK501164391. Once you receive your invoice for this order, you may pay your invoice by credit card. Please follow instructions provided at that time.

Make Payment To:
Copyright Clearance Center
Dept 001
P.O. Box 843006
Boston, MA 02284-3006

For suggestions or comments regarding this order, contact RightsLink Customer Support: customercare@copyright.com or +1-877-622-5543 (toll free in the US) or +1-978-646-2777.

Gratis licenses (referencing $0 in the Total field) are free. Please retain this printable license for your reference. No payment is required.

Appendix A2: Copyright permission for Chapter 5

Beth Darchi <DarchiB@asme.org> Wed, Nov 27, 2013 at 12:50 AM
To: xiaogang xiong <xiong@ctrl.mech.kyushu-u.ac.jp>

Dear Mr. Xiong:
This letter has been revised to reflect all requests. It is our pleasure to grant you permission to use **Figure 1-9** from "A Contact Force Model with Nonlinear Compliance and Residual Indentation," by Xiaogang Xiong, Ryo Kikuuwe, and Motoji Yamamoto, Journal of Applied Mechanics, Vol.81, No.2, Article 021003, 2013, as cited in your letter for inclusion in a Ph.D. dissertation to be published by Kyushu University.

Permission is granted for the specific use as stated herein and does not permit further use of the materials without proper authorization. Proper attribution must be made to the author(s) of the materials. **PLEASE NOTE**: if any or all of the figures and/or Tables are of another source, permission should be granted from that outside source or include the reference of the original source. ASME does not grant permission for outside source material that may be referenced in the ASME works.

As is customary, we request that you ensure full acknowledgment of this material, the author(s), source and ASME as original publisher. Acknowledgment must be retained on all pages printed and distributed.

Many thanks for your interest in ASME publications.

Sincerely,

Beth Darchi
Publishing Administrator
ASME
2 Park Avenue, 6th Floor
New York, NY 10016-5990
Tel 1.212.591.7700
darchib@asme.org

From: xiaogang xiong [mailto:xiong@ctrl.mech.kyushu-u.ac.jp]
Sent: Saturday, November 23, 2013 7:03 AM
To: Beth Darchi
Subject: Re: Usage in Thesis/Dissertation

Dear Administrator Beth,

Thank you very much for your permission.

I thought I made a mistake in the last permission-form because I was a little confused by the that form.

I want to use the full text, including Figure 1~9, of the following paper:

Xiaogang Xiong, Ryo Kikuuwe, and Motoji Yamamoto:"A Contact Force Model with Nonlinear Compliance and Residual Indentation," Transactions of ASME: Journal of Applied Mechanics, Vol.81, No.2, Article 021003, 2013.

in my Ph.D. dissertation.

I update a new version of the permission-form. I very appreciate your help if you give me the permission.

Thank you very much.

Xiaogang Xiong

Three Park Avenue tel 1.212.591.7000
New York, NY fax 1.212.591.7674
10016-5990 U.S.A. www.asme.org

ASME CONFERENCE/JOURNAL /BOOKS PUBLICATIONS PERMISSION REQUEST FORM:
Please be sure to fill out all in order to complete the form, then email the form to permissions@asme.org.
*Please type in all required text.

ASME Publication Title Conference/Journal/Book)*: Transactions of ASME: Journal of Applied Mechanics

Complete List of Authors*: Xiaogang Xiong, Ryo Kikuuwe, and Motoji Yamamoto

Paper Title (Conference/Journal) *: A Contact Force Model With Nonlinear Compliance and Residual Indentation

Paper Number Conference)*: 021003
Volume Number (Journal) *: 81
Indicate Page(s) in the ASME publication: 021003-1~021003-8
Year of Publication*: 2013
List Figure Numbers: 1~9
List Table Numbers: 0
Number of Copies: 1

Usage (Please check box): ☑ Print ☑ Academic ☑ Online ☐ Intranet

Title of outside publication*: Kyushu University Doctoral Dissertation Database

Publisher*: Kyushu University

Explanation of Usage: As a part of my Ph.D. dissertation submitted to Kyushu University.

First Name*: Xiaogang
Last Name*: Xiong
Address Line 1*: Department of Mechanical Engineering, Faculty of Engineering, Kyushu University, 744 Motooka, Nishi-ku, Fukuoka 819-0395, Japan
Address Line 2:

City*: Fukuoka
State*: Fukuoka
Zip*: 819-0395
Phone: +81-092-802-3179
Fax: +81-092-802-3177
Email*: xiong@ctrl.mech.kyushu-u.ac.jp